Distribution Agreement

In presenting this thesis or dissertation as a partial fulfillment of the requirements for an advanced degree from Emory University, I hereby grant to Emory University and its agents the non-exclusive license to archive, make accessible, and display my thesis or dissertation in whole or in part in all forms of media, now or hereafter known, including display on the world wide web. I understand that I may select some access restrictions as part of the online submission of this thesis or dissertation. I retain all ownership rights to the copyright of the thesis or dissertation. I also retain the right to use in future works (such as articles or books) all or part of this thesis or dissertation.

Signature:

_____ _____

Kate Heffernan Date

Astrocytes of the primate: form and function in health and disease

By

Kate S. Heffernan
Doctor of Philosophy

Graduate Division of Biological and Biomedical Science

Neuroscience

_____
Adriana Galvan
Advisor

_____
Yoland Smith
Co-Advisor

_____
Ellen Hess
Committee Member

_____
Baljit Khakh
Committee Member

_____
Steven Sloan
Committee Member

Accepted:

_____
Kimberly J. Arriola, Ph.D.
Dean of the James T. Laney School of Graduate Studies

_____
Date

Astrocytes of the primate: form and function in health and disease

By

Kate S. Heffernan
B.S., University of Rochester, 2014

Advisor: Adriana Galvan, Ph.D.
Co-Advisor: Yoland Smith, Ph.D.

An abstract of
A dissertation submitted to the Faculty of the
James T. Laney School of Graduate Studies of Emory University
in partial fulfillment of the requirements for the degree of
Doctor of Philosophy
Graduate Division of Biological and Biomedical Science
Neuroscience
2023

Abstract

Astrocytes of the primate: form and function in health and disease

By Kate S. Heffernan

Astrocyte morphology and function is affected in most neurodegenerative disorders. Investigation into the neurobiological mechanisms underlying astrocyte morphological and functional changes remains in its infancy and has great potential to identify new targets for biomarkers and therapeutics. Of note, species differences in astrocyte morphology and function have been described though not comprehensively assessed, which may complicate our understanding of astrocytes in health and disease. Here, we narrowed this gap in knowledge by using a combination of histological techniques, electrophysiology, and pharmacology to assess astrocyte morphology and interrogate function to broadly improve our understanding of primate astrocytes, with particular relevance to parkinsonism. We examined how astrocyte morphology and interaction with surrounding structures differed between healthy mice and rhesus macaques. Primate astrocytes displayed larger territories with lower density of branches, but primate and mouse astrocytes covered a comparable number of synaptic terminals. Our data suggest that astrocyte complexity scales with size to optimally cover the neuropil across species. We also found species-specific morphological differences between mouse and primate astrocytes in the external globus pallidus (GPe), an astrocyte-enriched structure which displays astrocyte dysfunction in mouse models of parkinsonism. Next, we assessed astrocyte morphology in a primate model of parkinsonism. Our data suggest that astrocytes display morphological changes in parkinsonian primates, such as decreased territory areas, but do not display signs of astrocytic reactivity common to other neurodegenerative disorders. We also assessed expression and localization of connexin-43 (cx-43), a gap junction protein which is highly expressed in the GPe and increased in animal models of parkinsonism. Though cx-43 expression was not increased in parkinsonian primates, we did see increased localization to astrocyte endfeet. Finally, we examined how pharmacological manipulation of cx-43 affects pathological neuronal activity in the GPe of parkinsonian primates. Blocking astrocyte cx-43 further exacerbated some of the electrophysiological features of parkinsonism, which together with increased cx-43 expression in astrocyte endfeet, could indicate altered glio-vascular interactions following dopamine depletion. Together, these studies provide new information about astrocytes across species and highlight the importance of investigating astrocyte morphology and function in primate species to better understand their contribution to human disease.

Astrocytes of the primate: form and function in health and disease

By

Kate S. Heffernan
B.S., University of Rochester, 2014

Advisor: Adriana Galvan, Ph.D.
Co-Advisor: Yoland Smith, Ph.D.

A dissertation submitted to the Faculty of the
James T. Laney School of Graduate Studies of Emory University
in partial fulfillment of the requirements for the degree of
Doctor of Philosophy
Graduate Division of Biological and Biomedical Science
Neuroscience
2023

ACKNOWLEDGEMENTS

I am incredibly grateful to my advisor, Adriana Galvan, for her support and guidance throughout my time in graduate school. Adriana, thank you for always entertaining my ideas (no matter how "out there") and for countering my pessimism with optimism and encouragement. This allowed me to push forward even when experiments failed, or applications were rejected. I would also like to thank my co-advisor, Yoland Smith, for invaluable advice and guidance.

I am appreciative for my committee members: Ellen Hess, Baljit Khakh, and Steven Sloan. Thank you for your time and valuable feedback. I consider myself lucky to have had the opportunity to learn from each of you.

To all of the Galvan, Wichmann, and Smith lab members, past and present, thank you for your support. I am particularly grateful to those who have played a significant role in my experience as a graduate student. Thomas Wichmann- thank you for your thoughtful feedback during lab meetings and MatLab expertise. My code always needed a bit (maybe a lot) of work, and you were always willing to help. Damien Pittard, DeErra Locklin, and Charlotte Armstrong – thank you for your expertise and care working with the animals in the lab. Cindy Hu and Yuxian Ma – thank you for teaching me the fine art of injectrode and optrode making. The postdocs: Anne-Caroline Martel, Dan Albaugh, Mike Caiola, and Peter Gombkoto – thank you for showing me that there is a light at the end of the tunnel. Kazi Rahman and Satya Thota – thank you for contributing your work and sharing your enthusiasm for science. Susan Jenkins and Jean-Francois Pare – you have taught me so much, but I am most grateful for your compassion and kindness. Diane Choi, Vanessa Barragan, and Natalia Magnusson – thank you for commiserating with me at times and bringing new energy and enthusiasm to the lab. I am excited to see where your paths take you. Thank you to Oreo, Izzy, Volks, Wagon, Lego, Hansel, and Gretel.

Finally, I would like to thank my family. This has been a long journey, and I would not have made it through without my parents, Susan and Robert Heffernan, my sister, Danielle Heffernan, and my husband, Asher Thoeming. Mom and Dad, your love and support have always been my greatest strengths, and my time in graduate school has been no exception. I know these past five years have been particularly difficult for all of us, for many reasons, but the countless phone calls and visits have helped me through. Danielle, you have always been my number-one cheerleader, seeing my potential, even when I could not see it myself. You were usually the source of unexpected package deliveries, and your care packages always arrived when I needed them the most. Asher, you have been my best friend from undergrad to grad and in between. Thank you for the years of unwavering support and love, and for being a great dog-dad to Kona.

TABLE OF CONTENTS

LIST OF FIGURES AND TABLES

CHAPTER 1: Introduction

The chapter contains excerpts from:

Heffernan, K.S., Galvan, A. (2023). Building and characterization of an affordable diOlistic device for single-cell labeling in rodent and non-human primate brain slices. *Current Protocols in Neuroscience*. https://doi.org/10.1002/cpz1.760.

Heffernan, K.S., Rahman, K., Smith, Y., Galvan, A. (2022). Characterization of the GfaABC1D promoter to selectively target astrocytes in the rhesus macaque brain. *Journal of Neuroscience Methods*. https://doi.org/10.1016/j.jneumeth.2022.109530.

1.1. CONTEXT

This dissertation "Astrocytes of the primate: form and function in health and disease" is presented in five chapters. The first chapter begins with a brief discussion of the known morphological and functional features of astrocytes across species, followed by discussion of the pathophysiology of parkinsonism and the potential contribution of astrocytes to the disease state, and concluded with a conceptual outline of the dissertation. Chapter 2 compares differences in astrocyte morphology between non-human primates and rodents and explores possible implications for divergent astrocyte function. Much of our understanding of astrocyte form and function originates from work in rodents. By investigating functional and morphological characteristics of primate astrocytes, we provide a comprehensive framework that has significant implications for astrocyte function in human health and disease. Chapters 3 and 4 then explore astrocyte morphological and functional changes in a non-human primate model of parkinsonism. The final chapter of the dissertation summarizes the findings, discusses limitations, and provides direction for future studies.

1.2. ASTROCYTES: A HISTORICAL PERSPECTIVE

Historically, astrocytes have been classified based on morphology and anatomical location. Rudolf Virchow coined the term "neuroglia" in 1856, describing connective tissue containing nerve cells (Virchow, 1856; Weigert, 1895). Astrocytes were then classified into two groups based on morphology and gross anatomical location: fibrous and protoplasmic (Andriezen, 1893). White matter fibrous astrocytes, named for their numerous fibrils, had long and thin processes forming a star-like shape (Figure 1.1). Gray matter protoplasmic astrocytes were also characterized by many fibrils, though they contained less than fibrous astrocytes (Andriezen, 1893). With the advent of histological techniques, Cajal described the morphological properties of astrocytes with gold-sublimated chloride, reduced silver nitrate, and Golgi

impregnation (Cajal, 1913). The star-shaped cells extended processes into the neuropil and formed endfeet with vasculature. These morphological features led early researchers to suggest that astrocytes delivered nutrients from the bloodstream to neurons (Golgi, 1873). Early morphological studies and drawings provided insight that would spark the interest in astrocyte form and function.

1.3. ASTROCYTE FORM FOLLOWS FUNCTION

1.3.1 Overall astrocyte morphology and regulation of synapses

Canonical protoplasmic astrocytes display a complex and spongiform morphology. Like neurons, the main processes in astrocytes are rich in intermediate filaments. Filamentous proteins, such as glial fibrillary acidic protein (GFAP), have restricted expression in the primary and secondary branches emanating from the soma (Bushong et al., 2002). While staining for GFAP is commonly used to visualize astrocytes and reliably labels the primary branches, only about 15% of astrocyte volume is revealed with such staining (Bushong et al., 2002). Smaller processes, often termed ‘branchlets’ and ‘leaftlets’ or perisynaptic astrocytic processes ‘PAPs’ when adjacent to a neuronal synapse, make up most of the astrocytic volume (Figure 1.2). Astrocyte leaflets are small structures which contain glycogen granules and ribosomes but lack the filaments seen in primary and secondary branches (Bernardinelli et al., 2014). With diameters ranging in the tens to hundreds of nanometers, leaflets are often too small to be seen with conventional light microscopy approaches.

The ‘tripartite’ synapse defines the spatial relationship between a pre-synaptic element, post-synaptic element, and astrocyte process (a PAP) (Araque et al., 1999; Aten et al., 2022). Visible with electron microscopy, astrocytes form intimate units with neuronal synapses and their associated structures. In the hippocampus, in which astrocyte morphology has been extensively studied, the vast majority of synapses are contacted by an astrocyte (Aten et al.,

2022; Ventura and Harris, 1999). Though likely dependent upon brain region, it is probable that similar level of astrocytic contact with synapses exists throughout the brain, indicating a considerable role for astrocytes in synaptic modulation and/or structural support. Such support may impact synaptic strength, as synapses in contact with astrocyte leaflets are larger than synapses without astrocyte contact (Witcher et al., 2007). In fact, numerous studies across brain regions have described changes in ultrastructural relationships between astrocytes and synapses following changes in synaptic activity evoked by physiological changes such as voluntary exercise or disease (Bernardinelli et al., 2014; Lushnikova et al., 2009; Sun et al., 2013; Tatsumi et al., 2016; Theodosis et al., 2008; Villalba and Smith, 2011). Structural changes in astrocyte leaflets are plastic and dynamic. As leaflets are devoid of GFAP, they utilize actin dynamics much like dendritic spines (Haber et al., 2006; O'Neill et al., 2023). Changes in astrocyte leaflet morphology have been shown to coordinate with changes in dendritic spines, and thus the dynamic nature of astrocyte leaflets allows for quick reorganization of neuron-glial communication at synapses (Haber et al., 2006). For instance, following induction of long-term potentiation, leaflets stabilize around the synapse in minutes (Bernardinelli et al., 2014).

1.3.2 Astrocyte endfeet and regulation of blood vessels

Astrocytes have endfeet, distal extensions of processes which make direct contact with vasculature (Figure 1.3). While it has not been investigated directly, endfeet appear to emerge from major branches, given their robust GFAP expression. Astrocytic endfeet are flattened processes that wrap around blood vessels. They surround the basal membrane, sealing in pericytes and endothelial cells, to maintain the blood brain barrier (BBB). Across brain regions, nearly all astrocytes are in direct contact with at least one blood vessel (Hösli et al., 2022b). In healthy brains, endfeet are estimated to cover 99% of the cerebrovascular surface (Mathiisen et al., 2010). But in many conditions such as Multiple Sclerosis, aging, and stroke, coverage of

vasculature is reduced, increasing permeability and disruption of the BBB (Montagne et al., 2015; Niu et al., 2019; Wang and Parpura, 2016). Like synapses, astrocytic coverage of vasculature is a dynamic process, ensheathing vessels on the order of minutes to hours (Mills et al., 2022). The endfeet are rich in mitochondria which aid in the release of vasoactive molecules (Abbott et al., 2010; Mathiisen et al., 2010). The release of such vasoactive molecules leads to changes in vessel diameter (Takano et al., 2006).

1.3.3 Composition and function of astrocyte networks

Astrocytes form extensive networks through the coupling of connexins. Both connexin-30 (cx-30) and connexin-43 (cx-43) are expressed primarily in astrocytes and show a preferential regional distribution (Nagy et al., 1999). In adult mammals, cx-30 is abundantly expressed in cortex, thalamic nuclei, and the brainstem relative to other structures. Most brain structures express cx-43 at stable levels, with particularly high expression in the hippocampus and cerebellum (Mazaud et al., 2021; Nagy et al., 1999). Cx-43 is primarily involved in astrocyte coupling, though the extent of its functions remain to be elucidated (Hösli et al., 2022a).

Connexins can function as a hemichannel allowing for the direct exchange of small molecules, or as a gap junction when paired with an opposing membrane. Each gap junction channel, or hemichannel, is composed of six subunits. Gap junctions can be homomeric or heteromeric, composed of hemichannels from two different connexin subtypes (cx-30 and cx-43 gap junctions have been reported)(Bennett et al., 2003). Once paired, the pore between two hemichannels allow diffusion of small molecules less than approximately 1 kDa (Bennett et al., 2003). The pore size limits the passage of molecules to those such as ions, second messengers, neurotransmitters, and metabolites (Figure 1.3). Like PAPs and endfeet, astrocyte coupling is likely a dynamic process, as connexins have a short half-life in the range of 1-5 hours (Leybaert et al., 2017).

The functions of astrocyte coupling remain unclear. It has been proposed that the network allows redistribution of energy substrates from the blood such as glucose (and subsequent breakdown to glutamine for distribution) and lactate (Cheung et al., 2022; Harris, 2007). However, the vast majority of astrocytes make direct contact with vasculature (Hösli et al., 2022b). Thus, in the context of metabolite redistribution, direct vascular contact and astrocyte-astrocyte coupling appears redundant, suggesting that astrocyte coupling likely plays a multifaceted functional role. Astrocyte networks also redistribute ions such as potassium and calcium (Bazzigaluppi et al., 2017; EbrahimAmini et al., 2021). Changes in the buffering of both ions can influence the excitability of surrounding neurons. For example, blockade of cx-43 gap junctions using the mimetic peptide Gap27 increased levels of extracellular potassium, enhancing or reducing neuronal activity and local field potential amplitude dependent upon the ion's concentration (Bazzigaluppi et al., 2017; Bellot-Saez et al., 2018). Oscillations of calcium across astrocyte networks were also shown to precede neuronal synchronization in sleep, with cx-43 blockade preventing the synchronization of neurons (Szabó et al., 2017). Thus, astrocytes coupled by cx-43 form networks which can impact the activity of surrounding neurons. In addition to physiological effects on neuron activity, astrocyte cx-43 also effects astrocyte morphology. Knockout of cx-43 in mice results in astrocytic reactivity and hypertrophy (Chever et al., 2014; Hösli et al., 2022a). Hypertrophy may be related to the expression of the water channel aquaporin-4 (AQP4), which has shown to colocalize with cx-43 in astrocyte endfeet (Nicchia et al., 2005).

1.4. SPECIES-SPECIFIC ASTROCYTE FORM MAY REVEAL SPECIALIZED FUNCTION

Previous studies reported differences in morphology between rodent and primate astrocytes (Colombo et al. 1995; Oberheim et al. 2006, 2009; Falcone et al., 2019). It was

discovered that primate astrocytes occupy larger territory areas and have a greater number of primary branches (Oberheim et al., 2009). Unique features of primate astrocytes have also been described. In neocortex, mammals contain interlaminar astrocytes (ILAs), polarized astrocytes with cell bodies residing in layer 1 of cortex with processes that span various layers. However, the length of ILA processes increases in higher-order species, terminating in layer 2-3 in mice and layers 4-5 in primates. Perhaps the length of ILA processes increased in parallel with the expansion of the neocortex (Falcone et al., 2019). While the functional purposes of ILAs are unknown, great emphasis has been placed on the expansion of processes in primates (Colombo et al., 1995; Falcone et al., 2019). In addition to ILAs, cortical astrocytes in hominid species present varicosities, but such varicosities were not found in the brains of old world monkeys such as rhesus macaques (Falcone et al., 2021a; Oberheim et al., 2009). It is unclear if 'varicose projection' astrocytes (VPAs) represent a separate class or state of astrocyte.

In addition to morphology, species differences in astrocytic gene expression and function have been described. Transcriptomic analyses revealed that only 30% of astrocyte genes enriched in humans were also enriched in mice (Zhang et al., 2016). Interestingly, 52% of astrocyte genes enriched in mice were also enriched in humans. However, genes that were highly enriched in mouse astrocytes such as *GFAP*, *AQP4*, *SLC1A2*, and others were also enriched in human astrocytes (Zhang et al., 2016). And while differences in gene expression between species are evident, studies of the functional role of such genes in primate species have been hampered by technical limitations. For functional assessments, the field has relied on *in vitro* studies. Human astrocytes have reportedly faster calcium transients in response to neurotransmitters (Oberheim et al., 2009), though once again, the functional significance of this difference is unknown. Human astrocytes also demonstrate greater susceptibility to oxidative stress, which

may have significant implications for neurodegenerative disease (Li et al., 2021). Lastly, mice transplanted with human glial progenitor cells, which largely differentiated into astrocytes, performed better on cognitive tasks than their control counterparts (Han et al., 2013). The human-derived astrocytes in these mice also retained primate features such as long processes seen in ILAs, suggesting that such features may be intrinsically programmed (Han et al., 2013). Thus, while there is evidence to support unique functions and features of primate astrocytes, many questions remain about the possible divergence of both morphology and function of primate astrocytes from rodent astrocytes. Further investigation has largely been hindered by the lack of tools to comprehensively assess astrocytes in high-order species.

1.5. TOOLS TO REVEAL MORPHOLOGY AND INTERROGATE ASTROCYTE FUNCTION IN PRIMATES

1.5.1 Immunohistochemical markers and morphological methods

Despite an increasing interest in astrocytes, reliable methods to reconstruct astrocyte morphology in primates remain limited. Most studies rely on the use of immunohistochemical markers, single cell filling, or viral transduction. Commonly used markers for astrocytes such as glial fibrillary acidic protein (GFAP) reveal only a fraction of the astrocytic processes, and also show regional differences in expression (Bushong et al., 2002). Other markers that are commonly used to identify astrocytes include Aldh1L1, S100β, Sox9, and transporters such as GLAST, GLT-1, and GAT-3 (Galvan et al., 2010; Jurga et al., 2021; Sun et al., 2017). Aldh1L1 is a cytoplasmic enzyme which labels the astrocyte cell body and some of its processes, and thus it is effective for astrocyte identification but inadequate for morphological assessment (Mudannayake et al., 2016). S100β is a calcium-buffering protein also expressed in the cytoplasm of astrocytes and some mature myelinating oligodendrocytes (Du et al., 2021). Similarly to Aldh1L1, S100β is effective for astrocyte identification more so than morphological analyses, and its labeling of oligodendrocytes makes it less suited for identification of cell types

in white matter. A newer identified marker, Sox9, is a transcription factor which results in a nuclear stain in astrocytes and neural stem cells in neurogenic zones (Sun et al., 2017). Localization to the cell's nucleus makes Sox9 ideal for cell type identification, but once again insufficient to reveal morphology. Transporters such as GLAST, GLT-1, and GAT-3 label fine astrocyte processes, but their expression and distribution may vary within a cell and by brain region, and thus they are best suited for identification of astrocyte processes for electron microscopy, in which the relationship between astrocyte transporters and synapses are of interest.

Immunohistochemical markers lack uniform expression throughout the astrocyte, thus other methods have been developed and used to reveal astrocyte morphology. Golgi stains have been used to label individual astrocytes, however, this technique requires long incubation times and relies on brightfield microscopy which has limited resolution (Golgi, 1873; Gull et al., 2015). Though, Golgi-impregnated tissue has successfully been used in electron microscopy studies (Vints et al., 2019). DiOlistics (the use of dyes that are incorporated into cells using high pressure (Gan et al., 2000)) have also been used to label astrocytes, but like Golgi staining, the number and distribution of labeled astrocytes is random. Thus, the technique may yield few labeled cells per section (Gan et al., 2000; Heffernan and Galvan, 2023; Seabold et al., 2010). Intracellular injection of fluorescent dyes (e.g., Lucifer Yellow) resolves fine morphological detail in individual astrocytes but it is time consuming and requires technical expertise, and specialized equipment (Moye et al., 2019). It should also be noted that both diOlistics and intracellular injection typically require unfixed or lightly fixed tissue, rendering the tissue unusable for other types of analysis such as photo conversion and electron microscopy.

1.5.2 Adeno-associated viruses (AAV) and astrocyte-selective promoters

In light of the challenges associated with immunohistochemical markers and other histological techniques, genetic approaches have been used to label astrocytes. Aldh1L1

transgenic mice have commonly been used to drive transgene expression in astrocytes (Srinivasan et al., 2016). While Aldh1L1 has demonstrated specificity in transgenic mice, when packaged in an AAV, it results in significant transduction of neurons in many brain regions (Mudannayake et al., 2016; Koh et al., 2017). Given that transgenic lines are not currently available for practical reasons in primate research, viral vectors are necessary to drive cell-type specific expression of transgenes (Izpisua Belmonte et al., 2015).

Many studies have used the gfa2 sequence of the glial fibrillary acidic protein (GFAP) as a promoter to target astrocytes (Lee et al., 2008, 2006). The gfa2 sequence is relatively large at 2.2 kb, encompassing nearly half of the packaging capacity of adeno-associated virus (AAV) vectors which are the most used vectors in primate neuroscience research. Early truncated versions of the gfa2 promoter, such as gfa28, did not result in selective targeting of astrocytes (Lee et al., 2006). More recently, the GfaABC1D promoter, a truncated version of gfa2 (681 bp), was shown to display a higher astrocyte transduction efficiency, along with decreased non-specific targeting of neurons (Lee et al., 2008). GfaABC1D has been successfully used to target astrocytes in various studies (Lee et al., 2008; Nagai et al., 2019; Octeau et al., 2018; Pignataro et al., 2017; Poskanzer and Yuste, 2016; Xie et al., 2010; Yu et al., 2018). However, most of the available studies have used the GfaABC1D promoter in mice, and recent work has demonstrated non-specific transduction and lower efficiency of the GfaABC1D promoter in rats, underscoring the need for species specific testing of viral vector tools (Taschenberger et al., 2017). Furthermore, viral efficiency and specificity often differ between primates and rodents, even when using the same virus and anatomical target (Albaugh et al., 2020; Jüttner et al., 2019). A study in marmosets used different fragments of the gfa2 sequence to drive expression in astrocytes, demonstrated a tradeoff between sequence length and specificity, such that a

minimum sequence length of 0.3kb was necessary to minimize non-specific transduction of neurons. This specific shortened gfa2 promoter provides a similar specificity and efficiency to GfaABC1D, but so far, the specificity had only been assessed in the cortex and cerebellum in marmosets (Shinohara et al., 2016). In addition to transgenic lines and AAVs, vectors based on lentivirus have been used to transduce astrocytes in rodents. While lentiviruses have greater packaging capabilities than AAVs, their larger size restrict diffusion across large brain regions (Huda et al., 2014).

To this end, we tested the specificity and efficacy of the GfaABC1D promoter in rhesus macaques (Heffernan et al., 2022). Following injections of AAV5-GfaABC1D-tdTomato into basal ganglia structures in two rhesus macaques, we found robust expression of the marker protein in the regions injected with the virus. Transduced cells co-expressed Aldh1L1 and GFAP, and our electron microscope results further confirmed their astrocytic identity. The ultrastructural observations also demonstrated that within individual astrocytes, tdTomato was expressed throughout fine processes, surrounding neuronal terminals and blood vessels.

1.5.3 Exploring astrocyte function in vivo

Using transgenic rodent lines and AAVs as described above, studies have begun to analyze astrocyte functions in behaving animals. Studies have primarily used optogenetics (Mederos et al., 2019), designer receptors exclusively activated by designer drugs (DREADDS) (Adamsky et al., 2018; Durkee et al., 2019; Nagai et al., 2019), and pharmacology to study astrocyte function (Abudara et al., 2014; Chever et al., 2014; Stehberg et al., 2012). In the case of optogenetics, the exact functional consequence of expressing ion channels in astrocytes is unclear, as astrocytes are not electrically active cells. However, astrocytes do express g-protein coupled receptors. Thus melanopsin, a light-activated receptor which mimics gq-coupled receptors, could be a physiologically-relevant optogenetic method to manipulate astrocyte

activity (Mederos et al., 2019). However, an important hurdle in the use of optogenetic tools in primates is that the spread of light in the large primate brain (in comparison to rodent brains) is limited, making the modulation of sufficient numbers of astrocytes unlikely to produce quantifiable effects *in vivo* (Galvan et al., 2017). In contrast, chemogenetic manipulations using DREADDs allow modulation over many astrocytes. However, DREADD expression must be restricted to the brain region of interest, which can be difficult to achieve with intracerebral injections of viral vectors. Thus, pharmacological approaches to modulate astrocyte activity appear most feasible in primate species, though these also present some limitations.

There are limited numbers of pharmacological compounds that have specificity for astrocytes. Of the most notable, gap junction blockers have been used for decades to assess astrocyte coupling in culture, brain slices, and in living animals. Connexin channels which form hemichannels and gap junctions are expressed in tissues throughout the body and cell types within the brain. And given their similar structure, compounds that specifically target one connexin versus another are limited. Historically, compounds such as carbenoxolone, quinine, octanol, and others have been used to block gap junctions despite a host of known off-target effects (Manjarrez-Marmolejo and Franco-Pérez, 2016; Rouach et al., 2003). However, given cx-43's specific expression in astrocytes, and to a lesser degree endothelial cells, mimetic peptides such as Gap26 and Gap27 were developed to target cx-43 over other connexins. These peptides have been used *in vitro* and *in vivo* to block astrocyte gap junctions (Bazzigaluppi et al., 2017; EbrahimAmini et al., 2021; Stehberg et al., 2012).

1.6. PATHOPHYSIOLOGY OF PARKINSON'S DISEASE AND THE MPTP NON-HUMAN PRIMATE MODEL

1.6.1 Pathophysiology

Parkinson's disease (PD) is largely characterized by the degeneration of substantia nigra compacta (SNc) cells, the concomitant depletion of nigral-striatal dopamine and emergence of

motor deficits, the most common of which include asymmetrical resting tremor, postural instability, bradykinesia, and rigidity. Motor deficits nearly always improve with levodopa (Blumenfeld, 2010). There are also non-motor features of the disease, including cognitive deficits in executive functioning, depression, sleep disturbances such as REM sleep behavior disorder, and dementia in later stages. Postmortem examination of brain tissue from PD patients show a-synuclein aggregates and Lewy bodies in addition to loss of pigmented dopaminergic cells in the SNc (Braak et al., 2003).

In PD patients and animal models of parkinsonism, motor deficits are partly attributed to aberrant neuronal firing rates and patterns in the motor portion of basal ganglia-thalamo-cortical circuits. Projections from motor and premotor cortices innervate the putamen (the motor portion of the striatum). The putamen then projects to the external globus pallidus (GPe), subthalamic nucleus (STN), internal globus pallidus (GPi), and substantia pars reticulata (SNr) via the indirect pathway. The direct pathway sends projections from the putamen directly to the GPi and SNr. The output nuclei (GPi and SNr, with the GPi being the main output in the motor circuit) send their axons to motor regions of the thalamus which projects back to cortex. The output of the basal ganglia also reaches downstream nuclei such as the pedunculopontine nucleus, lateral habenula, and superior colliculus. In addition, the striatum receives significant dopaminergic input from the SNc (Middleton and Strick, 2000). The functional model of basal ganglia pathophysiology proposes that the loss of dopaminergic input to the striatum in PD results in imbalanced activity between the indirect and direct pathways. As a significant neuromodulator in the striatum, dopamine loss affects the level of activity in direct versus indirect striatal medium spiny neurons (MSN), the striatal projection neurons. D1 receptor expressing, or direct pathway neurons, are normally excited by dopamine, whereas D2-receptor expressing, or indirect pathway

neurons, are normally inhibited by dopamine. The loss of dopamine decreases D1 direct MSN activity and increases D2 indirect MSN activity, though recent work failed to find distinct difference in firing rates between the two MSN populations in PD patients (Valsky et al., 2020). Increased MSN GABAergic transmission to the GPe reduces GABAergic transmission to the STN which results in increased glutamatergic drive to the output nuclei (GPi and SNr). Decreased inhibition from the direct pathway and increased glutamatergic drive from the STN leads to increased inhibitory outflow from the basal ganglia to thalamus (Wichmann and DeLong, 2003). The model suggests that this imbalance ultimately alters activity in the regions of cortex that receive the basal ganglia-processed information (mostly premotor and supplementary motor cortices), altering movement planning and execution leading to inhibition of voluntary movements (Figure 1.4).

As proposed by the functional model, several studies have identified changes in firing rates throughout the basal ganglia circuits in parkinsonian animals and PD patients (Galvan et al., 2015a). However, other studies have pointed to the importance of alterations in firing patterns, inter-neuronal synchronization, and oscillatory activity (Brown et al., 2001; Galvan et al., 2015a). Neurons throughout the basal ganglia show increased bursting discharge patterns following dopamine depletion in animal models and during intraoperative recordings in PD patients (Hutchison et al., 1994; Steigerwald et al., 2008). Beta oscillations (8-35 Hz) are seen in the basal ganglia and motor cortices in healthy individuals during movement, but are substantially increased in PD patients (Brown et al., 2001). Additionally, symptom severity is correlated with increased oscillatory activity below 15 Hz and decreased activity above 15 Hz in the non-human primate (NHP) 1-methyl-4-phenyl-1,2,3,6-tetrahydropyridine (MPTP) model of parkinsonism (Devergnas et al., 2014a). Changes in beta oscillatory power have received

considerable attention because they are significantly attenuated by current antiparkinsonian treatments such as levodopa and deep brain stimulation (DBS) (Brown et al., 2001; Meissner et al., 2005; Miocinovic et al., 2013).

1.6.2 Discovery and pathophysiology of the MPTP-treated non-human primate model of parkinsonism

The drug 1-methyl-4-phenyl-1,2,3,6-tetrahydropyridine (MPTP) was first synthesized by Albert Ziering, a scientist at Hoffman-LaRoche in 1947 (LEE et al., 1947). Shortly thereafter, MPTP was tested in animals and humans as a potential treatment for several disorders. However, it was not until the 1980s that MPTP's harmful effects were discovered. In 1982, a chemist attempted to synthesize a meperidine (Demerol) analog for illegal drug consumption, but the batch was inadvertently comprised of almost pure MPTP. The batch was distributed on the streets, and seven adults ultimately intravenously injected the drug. Within days of injection, all seven adults developed severe parkinsonian symptoms, including tremor and asymmetrical motor dysfunction. A few of the adults also displayed non-motor symptoms of parkinsonism such as executive functioning deficits and facial seborrhea (Langston, 2017).

The parkinsonian symptoms in the patients readily responded to levodopa (Ballard et al., 1985). This discovery ushered in a wave of new research to understand if MPTP also resulted in dopaminergic cell death in the substantia nigra. Early studies discovered that MPTP was not harmful on its own, but the breakdown of MPTP by monoamine oxidase B (MAOB) resulted in a highly toxic metabolite, MPP+ (Heikkila et al., 1984; Langston et al., 1984a). Astrocytes were responsible for the conversion of MPTP to MPP+, but were largely spared of toxic effects (Ransom et al., 1987). Instead of accumulating in astrocytes, researchers found that MPP+ had a high affinity for dopamine transporters which were expressed primarily on catecholaminergic neurons (Shen et al., 1985). Once inside dopaminergic neurons, MPP+ accumulates and inhibits

mitochondrial complex I, ultimately causing decreased ATP and increased generation of free radicals (Ramsay et al., 1986). Patients with PD also demonstrated mitochondrial complex I dysfunction, suggesting a common underlying mechanism for degeneration of dopaminergic cells (Schapira et al., 1990).

Given the similarities between the original MPTP patients and PD patients, researchers began to investigate MPTP's potential for creating animal models of PD. The first monkey models using MPTP were published in 1984 (Burns et al., 1984; Langston et al., 1984b). The models replicated the levodopa-responsive motor signs of PD with nigral dopamine depletion. Mice and rats were also given injections of MPTP, but it was ultimately found that rats (and mice, though to a lesser degree) have high levels of MAOB present in blood plasma, resulting in the conversion of MPTP to MPP+ prior to passing the blood brain barrier (Riachi et al., 1988). Thus, rats and mice show a lesser degree of central degeneration of dopaminergic cells after MPTP treatment than primates.

1.7. IMPORTANCE OF THE GPE IN PARKINSONISM

The GPe is a heterogeneous structure with several subtypes of neurons. The main classes of neurons are separated by distinct differences across several modalities, including intrinsic electrophysiological properties, synaptic inputs, projection targets, gene expression, and changes in activity following dopamine depletion (Abdi et al., 2015; Abecassis et al., 2020; Cui et al., 2016; Katabi et al., 2023; Pamukcu et al., 2019). Though there many subclasses, recent studies in rodents identified two primary populations of neurons in the GPe: arkypallidal neurons which primarily project from the GPe to the striatum (STR), and prototypical neurons which primarily project from the GPe to the STN (Abdi et al., 2015; Mallet et al., 2012; Mastro et al., 2014). Additionally, arkypallidal and prototypic neurons were shown to form a medio-lateral gradient and receive different inputs, suggesting functionally segregated regions of the GPe (Mallet et al.,

2012; Mastro et al., 2014). However, investigations into the synaptic inputs to each GPe neuron population have argued against direct pathway and indirect pathway segregation. Prototypic and arkypallidal neurons receive inputs from indirect pathway medium spiny neurons as well as collaterals from direct pathway medium spiny neurons of the STR, though indirect D2-expressing neurons remain the primary source of GABAergic input to the GPe (Cui et al., 2021). In addition, both prototypic and arkypallidal neurons receive inputs from the STN, though the STN preferentially targets prototypic neurons (Aristieta et al., 2021; Ketzef and Silberberg, 2021).

Considerable attention has been given to STN-projecting prototypic GPe neurons in the context of parkinsonism. This subclass of GPe neurons project to the STN, and receives the most inputs (relative to other GPe neurons) from the glutamatergic neurons within the STN which project back to the GPe (Aristieta et al., 2021; Mastro et al., 2014). The STN-GPe loop has been proposed as a potential generator of pathological oscillations in parkinsonism (Bevan et al., 2002; McCarthy et al., 2011; Nevado-Holgado et al., 2014). Due to the recurrent inhibitory-excitatory connections of the GPe and STN, the loop is prone to oscillations (Bevan et al., 2002). In fact, optogenetic patterning of GPe neurons to discharge at beta frequency resulted in beta oscillation-like activity throughout the basal ganglia-thalamo-cortical network, further implicating GPe activity in the pathological network activity seen in PD (Crompe et al., 2020).

In parkinsonian monkeys, GPe neurons have lower firing rates and an increased tendency to discharge in bursts compared with healthy animals (Miller and DeLong, 1987; Tachibana et al., 2011; Wichmann and Soares, 2006). The changes in firing rate and bursting seen in MPTP treated monkeys were also found in the GPe of PD patients (Hutchison et al., 1994). This change in GPe outflow influences activity of other basal ganglia structures, particularly the STN (Fan et

al., 2012). Manipulation of GPe activity has decreased pathological activity in downstream structures (such as the STN) and has reduced parkinsonian motor deficits in rodent and non-human primate models, demonstrating that the GPe plays a key role in modulating the basal ganglia-thalamo-cortical circuit and motor dysfunction in parkinsonism (Mastro et al., 2017; Meissner et al., 2005; Soares et al., 2004). Overall, changes to the GPe's heterogeneous synaptic inputs and outputs and emergence of pathological neuronal activity such as bursting and oscillations, have clear implications in the pathophysiology of parkinsonism.

1.8. RELEVANCE OF THE ASTROCYTE NETWORK IN THE GPE IN PARKINSONISM

Astrocytes are enriched in the GPe, outnumbering neurons (Cui et al., 2016). The high number of astrocytes suggests that they play a crucial role in the regulation of GPe function. Such regulation has been shown to falter following dopamine depletion. In dopamine-depleted mice, astrocytes within the GPe show decreased expression of GAT-3, an astrocyte-specific GABA transporter (Chazalon et al., 2018). Decreased astrocytic buffering of GABA further exacerbated the increased GABA release from indirect pathway striatal MSNs, resulting in tonic inhibition of GPe neurons and motor impairments. Another study found that GPe astrocytes maintain homeostatic levels of glutamate while gating striatopallidal GABA transmission, a function which is lost in a dopamine-depleted state (Cui et al., 2016). While limited, the studies investigating GPe astrocyte dysfunction in dopamine-depleted animals highlight their importance and relevance in parkinsonism.

In addition to altered GABAergic and glutamatergic buffering, astrocytes in the GPe may display changes in cell-cell coupling following dopamine depletion. The gap junction-associated protein cx-43 is enriched in the GPe in comparison to other basal ganglia structures (Charron et al., 2014; Nagy et al., 1999). Levels of cx-43 are further increased in the cortex of PD patients

and in the globus pallidus of a rodent model of parkinsonism (Itoh and Voskuhl, 2017; Kawasaki et al., 2009). Collectively, this suggests that astrocyte networks formed by cx-43 may be altered in the GPe in parkinsonism, providing a potential target to ameliorate pathological neuronal activity.

1.9. FRAMEWORK FOR THE DISSERTATION

The goal of the dissertation is to first characterize astrocyte morphology in the healthy non-human primate and then assess astrocyte morphology and function in a non-human primate model of parkinsonism. To reveal primate astrocyte morphological characteristics and compare with rodents, I use a multi-technique approach. In Chapter 2, I use a combination of immunohistochemistry, AAV-mediated labeling of astrocytes, diOlistics, and confocal and electron microscopy to reveal species similarities and differences in astrocyte morphology. I show that astrocyte morphological complexity has scaled with increased brain size. In Chapter 3, I compare astrocyte morphology and the expression of reactivity-associated markers in healthy and parkinsonian non-human primates. I demonstrate that while markers of reactivity are not elevated in the parkinsonian animals across several brain regions, astrocyte territory areas are reduced. In Chapter 4, I use in vivo electrophysiology and pharmacology to assess astrocyte function between healthy and parkinsonian non-human primates. While there is no clear effect of pharmacological manipulation of astrocytes in parkinsonian animals, the studies reveal a potential biomarker for parkinsonism that may be modulated by astrocytes. Finally in Chapter 5, I discuss the broader implications of this work and make suggestions for future studies. In sum, the work presented here thoroughly characterizes astrocytes in the non-human primate and identifies cell-type specific changes in the pathophysiology of parkinsonism.

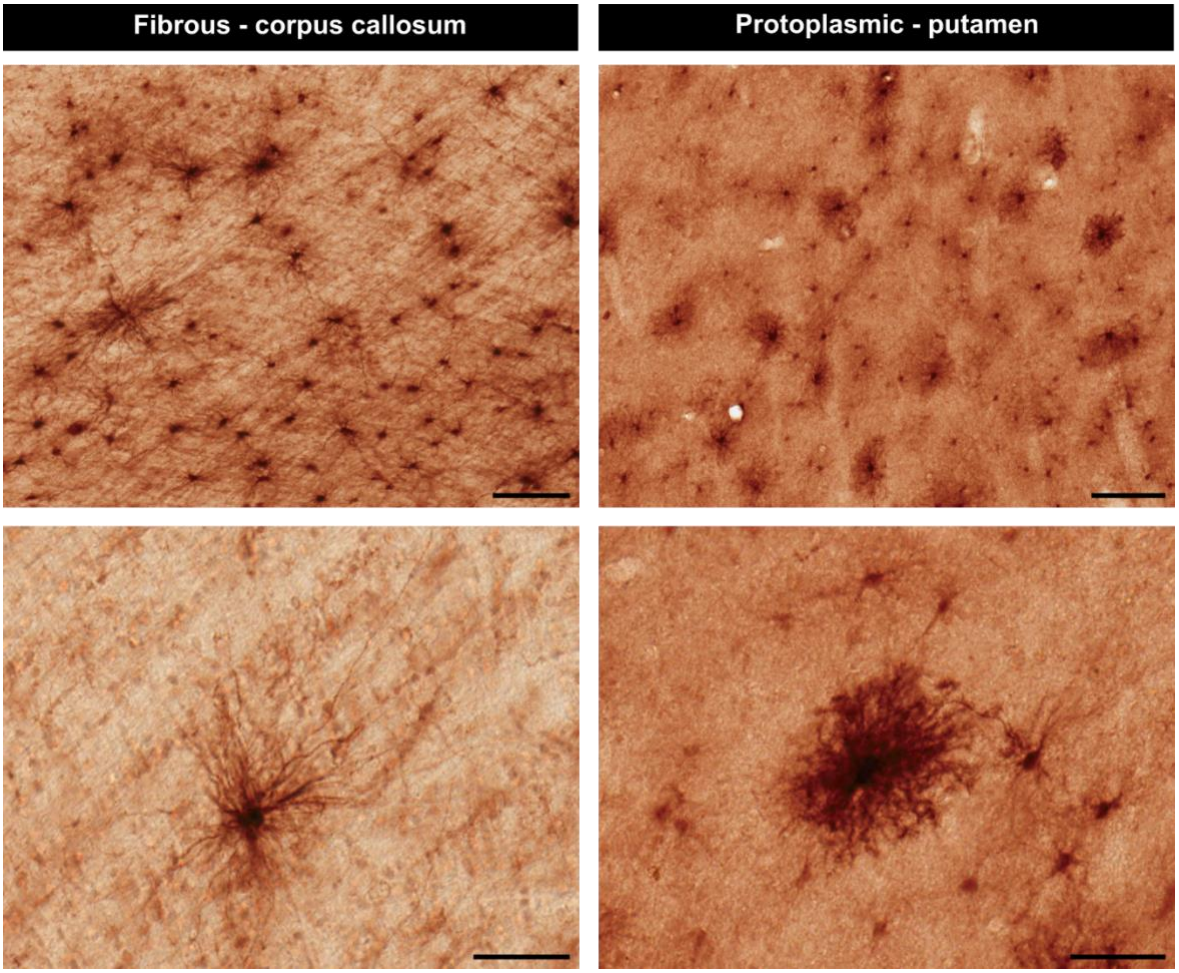

Figure 1.1 Fibrous and protoplasmic astrocytes.
Representative examples of fibrous (left) and protoplasmic (right) astrocytes. Fibrous astrocytes from corpus callosum and protoplasmic astrocytes from putamen in a rhesus macaque were labelled using a viral vector with an astrocyte-selective promoter to express tdTomato, which was revealed using antibodies and immunoperoxidase. Scalebars 100 µm on top images and 50 µm on bottom images (see Chapter 2 for detailed methods).

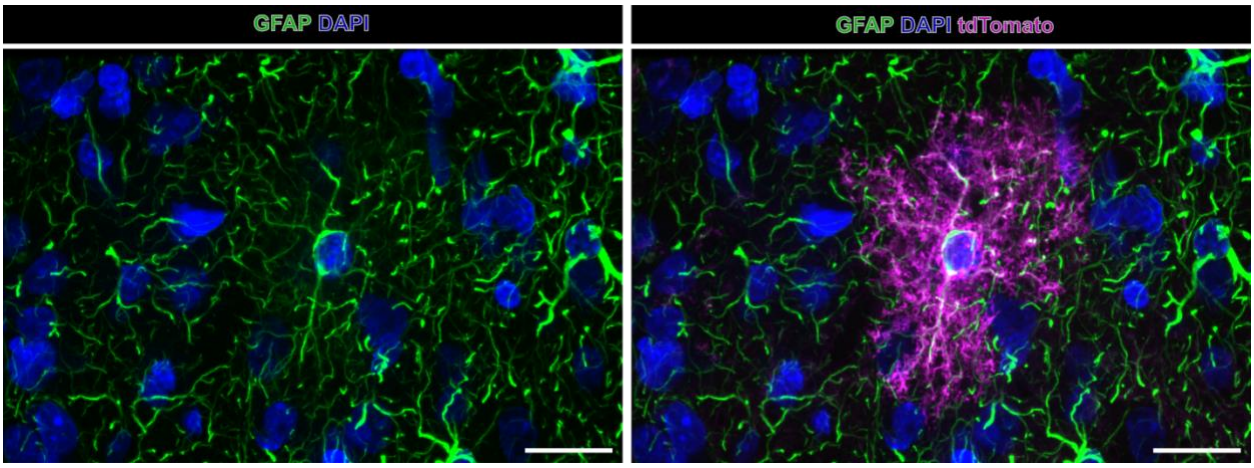

Figure 1.2 Expression of GFAP in an individual astrocyte.
(Left) Representative example of GFAP expression in an individual astrocyte in the rhesus macaque cortex using antibodies against GFP and revealed with immunofluorescence. (Right) Example of the same astrocyte from the left image, revealed using expression of tdTomato after injections with a viral vector with an astrocyte-selective promoter. (Green – GFAP; Magenta – tdTomato; Blue – DAPI). Scalebars 20 µm. (see Chapter 2 for detailed methods).

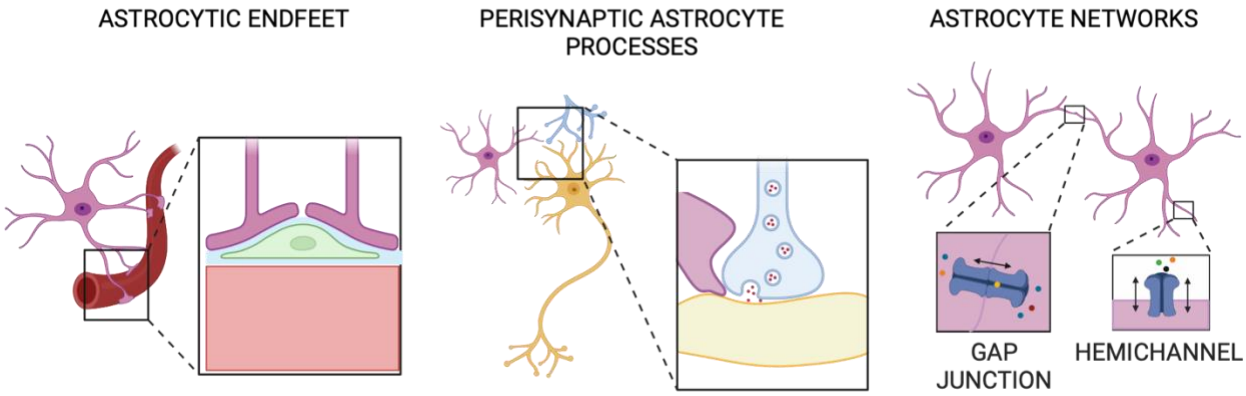

Figure 1.3 Astrocyte characteristics.
(Left) Morphology of astrocytic endfeet. (Middle) Morphology of perisynaptic astrocyte processes. (Right) Localization of astrocyte connexins which form gap junctions and hemichannels.

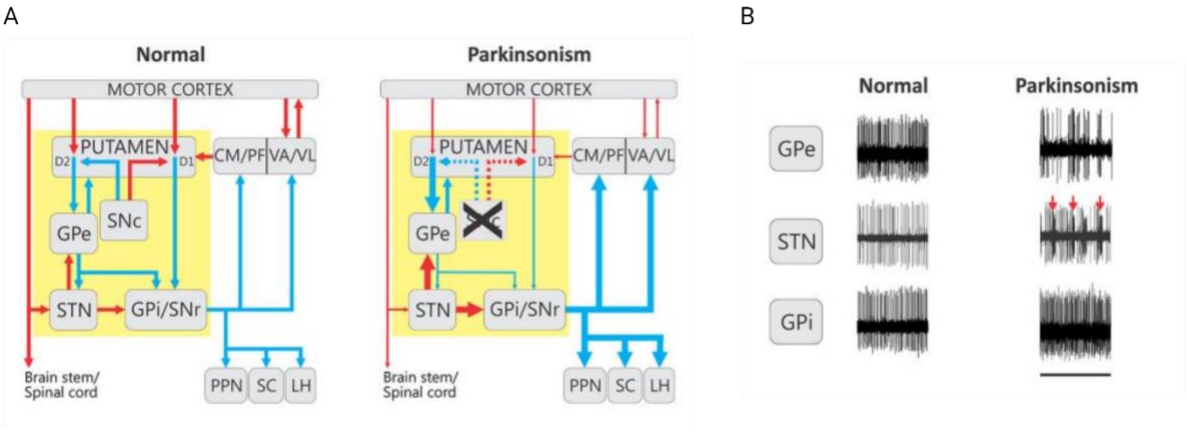

Figure 1.4 Firing rate and pattern changes in parkinsonism.
(A) The yellow box indicates the interconnected basal ganglia nuclei that receive extrinsic input from the cortical and thalamic regions. For simplicity some connections have been omitted from this diagram. The left panel indicates the circuits in the "Normal" state, and the right shows the overall changes in activity that have been associated with parkinsonism. Blue and red arrows indicate inhibitory and excitatory connections, respectively. The thickness of the arrows corresponds to their presumed activity. Abbreviations: CM, centromedian nucleus of thalamus; D1 and D2, dopamine receptor subtypes; GPe, external segment of the globus pallidus; GPi, internal segment of the globus pallidus; LH, lateral habenula; PF, parafascicular nucleus of the thalamus; PPN, pedunculopontine nucleus; SC, superior colliculus; SNc, substantia nigra pars compacta; SNr, substantia nigra pars reticulata; STN, subthalamic nucleus; VA, ventral anterior nucleus of thalamus; VL, ventrolateral nucleus of thalamus. (B) Extracellular recordings of neurons in the GPe, STN, and GPi in rhesus macaques before (normal) and after (parkinsonism) treatment with MPTP. Arrows indicate examples of bursts in an STN neuron. Horizontal line represents 1 s. Both panels reproduced with permission (Galvan et al., 2015a).

CHAPTER 2: Scaled complexity of mammalian astrocytes: insights from mouse and macaque

The chapter is reproduced with minor edits from:

Heffernan, K.S., Martinez, I., Jaeger, D., He, J., Stauffer, W.R., Khakh, B., Smith, Y., Galvan, A. (2023) Scaled complexity of mammalian astrocytes: insights from mouse and macaque. *In preparation.*.

2.1. ABSTRACT

Astrocytes intricately weave within the neuropil, giving rise to characteristic bushy morphologies. Pioneering studies suggested that primate astrocytes are more complex due to increased branch numbers and territory size compared to rodent counterparts. However, there has been no comprehensive comparison of astrocyte morphology across species. We employed several techniques to investigate astrocyte morphology and directly compared them between mice and rhesus macaques in cortical and subcortical regions. We assessed astrocyte density, territory size, branching structure, fine morphological complexity, and interactions with neuronal synapses using a combination of techniques including immunohistochemistry, AAV-mediated transduction of astrocytes, diOlistics, confocal imaging, and electron microscopy. We found significant morphological similarities between primate and rodent astrocytes, suggesting that astrocyte structure has scaled with evolution. Our findings show that primate astrocytes are larger than those in rodents but contest the view that primate astrocytes are morphologically more complex.

2.2. INTRODUCTION

Astrocytes have a complex architecture which allows them to directly interact with synapses, blood vessels, and other cells. Though astrocytes were thoughtfully described in the early studies of Rudolph Virchow and Ramon y Cajal, these cells were largely ignored and thought of as mere support for the better-studied neurons (Cajal, 1913; R. Virchow, 1846; Santiago Ramon y Cajal, 1911; Virchow, 1856). Only over the last few decades has interest in astrocytes grown substantially, resulting in a multitude of new tools to interrogate their function and characterize their morphology. Advancements such as chemogenetics and optogenetics combined with astrocyte-targeting transgenic mouse lines or adeno-associated virus (AAV) promoters allow for direct manipulation of astrocyte function (Adamsky et al., 2018; Mederos et

al., 2019; Nagai et al., 2019; Yu et al., 2020). Techniques such as 3D electron microscopy have allowed for reconstruction of astrocyte processes and their interactions with neuronal synapses and blood vessels at fine resolution (Aten et al., 2022; Salmon et al., 2023). Many of these approaches are commonly used in mice, but rarely in other species, which limits our knowledge of astrocyte morphology in primates.

Original studies discovered significant differences in morphology between rodent and primate astrocytes (Colombo et al. 1995; Oberheim et al. 2006, 2009; Falcone et al., 2019). While these studies present data supporting unique morphological features such as longer interlaminar astrocyte processes and the presence of varicosities on a subset of cortical hominid astrocytes, evidence demonstrating increased morphological complexity of astrocytes in primate species is lacking. It has been established that primate astrocytes display larger territory areas (Oberheim et al., 2009). However, details regarding the cellular density, primary branching structure, fine process size and density, and interactions with neurons and synapses remain largely unexplored. Further, morphological complexity and cellular density can have significant functional implications, as they may determine the number of synapses an astrocyte can regulate. Despite the lack of data directly analyzing astrocyte complexity across species, papers commonly cite primate astrocytes as more complex than rodent (Allen and Eroglu, 2017; Vasile et al., 2017; Verkhratsky et al., 2018).

Here, we used a series of techniques to systematically assess astrocyte morphology in mice and rhesus macaques across cortical and subcortical brain regions. Filtering down from overall astrocyte density to astrocyte territory size, individual astrocyte primary branching structure, and the fine process or perisynaptic astrocyte process (PAP) morphology, the data paint a comprehensive picture of astrocyte morphology across species. We show that while primate

astrocytes are larger than their rodent counterparts, their morphological complexity is comparable. Furthermore, we demonstrate that the degree of astrocyte-neuron interaction is scaled across species, despite previous claims. These findings point to a new understanding of astrocyte morphology and complexity in rodent and primate species that counter long-standing views in the field. Our data suggest astrocyte complexity scales with size to optimally cover the neuropil in order to allow them to perform their essential physiological and pathophysiological roles across species.

2.3. MATERIALS AND METHODS

2.3.1. Animals

All procedures were approved by the Animal Care and Use Committee of Emory University and performed in accordance with the Guide for the Care and Use of Laboratory Animals (NRC, 2010) and the U.S. Public Health Service Policy on the Humane Care and Use of Laboratory Animals (revised 2015).

All rhesus macaques were sourced from the Emory National Primate Research Center (ENPRC). The monkeys were maintained in a controlled environment with a 12-hour light/dark cycle, had free access to water, and were fed twice daily. Eight rhesus macaques were used in this study: 3 received AAV injections (4-year-old male, 4-year-old female, and 5-year-old male), 2 for diI and GFAP experiments (6-year-old-male, 4-year-old female), and 3 for cell density experiments (9-year-old female, 11-year-old male, and 3-year-old male). The two monkeys involved in diI and GFAP studies were assigned as clinical cases for heart murmur/possible hypertrophic cardiomyopathy and chronic low weight without specific cause, respectively. The number of monkeys included in each experiment is summarized in the table below and listed in the figure legend.

Mice (all C57BL/6J) were fed regular chow and water ad libitum and maintained at a 12-hour light/dark cycle. Fifteen mice were included in this study: 5 received AAV injections (females, 8-9 months of age), 7 for diI and GFAP experiments (males, 6-7 months of age), and 3 for cell counts (males, 5 months of age). The number of mice included in each experiment is summarized in the table below and listed in the figure legend.

Table 2.1. Animals

Species	Sex	Age at perfusion	Experiment
Rhesus macaque	Male	4 years	AAV5-GfaABC1D
Rhesus macaque	Female	4 years	AAV5-GfaABC1D
Rhesus macaque	Male	5 years	AAV5-GfaABC1D
Rhesus macaque	Male*	6 years	DiI, GFAP
Rhesus macaque	Female**	4 years	DiI, GFAP
Rhesus macaque	Female	9 years	Cell counts
Rhesus macaque	Male	11 years	Cell counts
Rhesus macaque	Male	3 years	Cell counts
Mouse	Female	9 months	AAV5-GfaABC1D
Mouse	Female	9 months	AAV5-GfaABC1D
Mouse	Female	9 months	AAV5-GfaABC1D
Mouse	Female	8 months	AAV5-GfaABC1D
Mouse	Female	8 months	AAV5-GfaABC1D
Mouse	Male	6 months	DiI, GFAP
Mouse	Male	6 months	DiI, GFAP
Mouse	Male	7 months	DiI, GFAP
Mouse	Male	7 months	DiI, GFAP
Mouse	Male	7 months	DiI, GFAP
Mouse	Male	7 months	DiI, GFAP
Mouse	Male	7 months	DiI, GFAP
Mouse	Male	5 months	Cell counts
Mouse	Male	5 months	Cell counts
Mouse	Male	5 months	Cell counts

GfaABC1D indicates animals that received AAV5 injections. DiI and GFAP indicates animals whose tissue was subjected to diOlistic bombardment and GFAP staining. Cell counts indicates animals whose tissue was stained for astrocyte and neuronal markers. *This animal presented a heart murmur with possible hypertrophic cardiomyopathy. **This animal was chronically underweight and unthrifty without specific cause.

2.3.2. AAV injections in mice and monkeys

Prior to enrollment in the study, blood samples from all monkeys were tested by the EPC Viral Core and confirmed sero-negativity for AAV5 antibodies. In two of the monkeys and all

mice, the pZac2.1 vector backbone and AAV5 serotype was used to express the fluorescent tag TdTomato under the GfaABC1D promoter. pZac2.1 gfaABC1D-tdTomato was a gift from Baljit Khakh (Addgene viral prep # 44332-AAV5 ; http://n2t.net/addgene:44332; RRID:Addgene_44332).(Shigetomi et al., 2013) In the third monkey, the pZac2.1 vector backbone and AAV5 serotype was used to express the membrane-tethered fluorescent tag GFP under the GfaABC1D promoter. pZac2.1 gfaABC1D.PI.Lck-GFP.SV40 was a gift from Baljit Khakh (Addgene viral prep # 105598-AAV5; RRID:Addgene_105598).(Shigetomi et al., 2013) The virus solutions were stored at -80°C and thawed the day of the injection. The details regarding injection procedure for two monkeys have been previously described.(Heffernan et al., 2022) Briefly, monkeys underwent chamber placement surgery or intracerebral injections of the virus. They were sedated with ketamine (10 mg/kg) and intubated for isoflurane anesthesia (maintained at 1-3%). Post-operatively, monkeys were treated with buprenorphine (0.03 mg/kg) and banamine (1 mg/kg) as analgesics, and Rocephin (25 mg/kg) to prevent infection. Monkeys that underwent chamber placement surgery then received intracerebral injections of the virus guided by electrophysiology. Monkeys were perfused 4-9 weeks following injection.

Mice were anesthetized with 3-4% isofluorane and maintained at 1.5-2.5% during surgery. Mice were given buprenorphine ER (1mg/kg) and 0.2% lidocaine (4mg/kg) and head fixed on a stereotaxic frame (Kopf). Craniotomies were performed bilaterally above primary motor cortex. In each hemisphere, 0.5 µl of virus was deposited in motor cortex (in mm from Bregma: AP +1.1, ML ± 1.5, DV 0.75) and striatum (AP +1.1, ML ± 1.5, DV 2.75) using a nanoinjector (Nanoinject II, Drummond Scientific). Mice were perfused 3-4 weeks following surgery.

2.3.3. General methods related to immunohistochemistry

For all sections below except 2.3.4.3 and 2.3.4.4, monkeys and mice were transcardially perfused with Ringer's solution followed by a fixative solution containing 4% PFA and 0.1% glutaraldehyde. Brains were post-fixed in 4% PFA for 24-48 hours at 4°C and then sectioned coronally at 60 µm on a vibratome (Leica). Prior to staining, all sections were first treated with 1% sodium borohydride, to reduce free aldehydes and Schiff bases resulting from glutaraldehyde fixation and rinsed in phosphate buffered saline (PBS; 0.01M, pH 7.4).

For sections 2.3.4.3 and 2.3.4.4 (DiI and GFAP) monkeys and mice were transcardially perfused with Ringer's solution. Whole mouse brains and 4 mm blocks of monkey brains were immersion-fixed in 4% PFA for 1 hour at room temperature and then sectioned coronally at 300 µm on a vibratome (Leica). Details for primary and secondary antibodies are listed in Table 2.2.

2.3.3.1. Cell counts: neurons and astrocytes

For each animal, three 60 µm sections were selected. Sections were separated by 60 µm for mice and 300 µm for monkey. All sections were located approximately within -0.1 to -0.46 mm from bregma in mouse and 16.05 to 13.8 from the interaural line in monkey according to the Paxinos brain atlases (Paxinos et al., 2000; Paxinos and Franklin, 2019). To prevent non-specific binding and permeabilize the tissue, sections were incubated in a solution of 1% donkey serum, 1% bovine serum albumin (BSA), and 0.3% Triton X-100 in PBS. Sections were then incubated overnight in the blocking/permeabilization solution containing antibodies for neurons (NeuN 1:10000) and astrocytes (Aldh1L1 1:3000 and S100β 1:200). Binding sites were revealed using a fluorophore-conjugated secondary antibody (all 1:100). Sections were incubated in the secondary solution overnight and rinsed in PBS. Sections were incubated in PBS containing DAPI (5µg/mL) for 10 minutes. Sections were then mounted with Vectashield (Vector Laboratories) on slides and coverslipped.

Slides were imaged using a confocal microscope (Leica DM5500B) equipped with a CCD camera (Orca R2; Hamamatsu). Regions of interest (primary motor cortex layers 2/3 and 5, primary somatosensory cortex layers 2/3 and 5, globus pallidus (external for monkey), and dorsal putamen (monkey) or dorsolateral striatum (mouse) were identified by pattern of DAPI staining and Z-stacks were obtained at 20x (monkey) or 40x (mouse) with a 1 µm step size. Higher magnification was used for mouse to ensure the image boundaries were within the brain area of interest. From each z-stack, maximum intensity projections of 10 slices (10 µm) were generated. Neurons and astrocytes were counted using the CellCounter plugin in ImageJ (Schindelin et al., 2012).

2.3.3.1. GFAP staining to investigate primary branching

Stored 300 µm thick sections from mouse and monkey brains were stained for glial fibrillary acidic protein (GFAP). Sections were incubated in a solution of 1% donkey serum, 1% BSA, and 1% Triton X-100 in PBS. Sections were then incubated for 3 days at 4°C in the blocking/permeabilization solution (with the Triton X-100 concentration was lowered to 0.3%) containing the GFAP antibody (1:5000). Binding sites were revealed using a fluorophore-conjugated secondary antibody (all 1:100). Sections were incubated in the secondary solution for 3 days at 4°C and rinsed in PBS. Sections were incubated in PBS containing DAPI (5µg/mL) for 10 minutes. Sections were then mounted with Fluoromount-G (Southern Biotech) on slides with 2 stacked 0.12mm deep coverslip spacers (Grace Bio-Labs) to reduce tissue compression.

GFAP-labeled astrocytes were imaged using a Leica SP8 confocal microscope. Z-stacks were obtained with a 40x (NA 1.3) objective, 1024x1024 scan format, 2x optical zoom, and 0.35 µm z-steps. Stacks were converted to maximum intensity z-projections in ImageJ. The image was thresholded using the automated “Default” selection and binarized. An outlined area overlay

of the cell territory was generated by using the "Analyze Particles" tool with a minimum particle size of 5 μm^2. The area outside of the territory was then "cleared" and the binarized image was subjected to Sholl analysis with the Simple Neurite Tracer plugin. The center of the soma was marked as the starting radius with a step size of 4 µm.

2.3.3.2. Territory size and neuropil infiltration volume (NIV) in astrocytes transduced with AAV5-GfaABC1D

Animals received viral injections and were perfused as described above. Sections were stained following the same procedure above described for cell counts using primary antibodies against either mCherry (1:1000 mouse or 1:2500 rabbit) or GFP (1:2000), revealed with the appropriate fluorophore-conjugated secondary antibody, and counterstained with DAPI. Sections were then mounted with Vectashield (Vector Laboratories) on slides and coverslipped.

Astrocytes were imaged using a microscope (Leica DM5500B) equipped with a spinning disk confocal (VisiTech International) and CCD camera (Orca R2; Hamamatsu). Z-stacks were obtained 63x with a 0.1 µm step size with a resulting x-y pixel size of 0.105 by 0.105 µm/pixel. Astrocytes were selected for imaging if they 1) were well-isolated from other labeled cells 2) displayed adequate signal to noise ratio 3) resided with layer 5 of primary motor cortex or post-anterior commissural putamen in monkeys (as determined by distance to brain surface and pattern of DAPI staining) or dorsolateral striatum in mice and 4) had its nucleus visible within the slice. Images were analyzed in ImageJ. Stacks of 89-537 images (8.9-53.7 µm) were converted to maximum intensity z-projections. The image was thresholded and binarized. Threshold parameters varied by cell due to differences in the level of tag protein expression and background. An outlined area overlay of the cell territory was generated by using the "Analyze

Particles" tool with a minimum particle size of 5 μm^2. The overlay generated area and Feret's maximum diameter (the longest edge to edge distance of the overlay).

The raw z-stacks of cortical astrocytes were also loaded into Imaris (v 9.8.0). For each astrocyte, three ROIs measuring 10 µm x 10 µm x 10 µm were created. All ROIs were placed to avoid the soma and major branches. The surface function of Imaris was used to render 3D reconstructions of the astrocyte branches within the ROI boundary. The volumes of each ROI, termed neuropil infiltration volume (NIV) were recorded (Baldwin et al., 2021; Stogsdill et al., 2017). Three ROIs were averaged for each cell, resulting in 90 ROIs and 30 NIV averages for mouse and 42 ROIs and 14 NIV averages for monkey. One monkey which received a viral injection with the membrane tethering Lck sequence (GfaABC1d-Lck-GFP) was not included in NIV analysis.

2.3.3.3. Fractal dimension and NIV in astrocytes labeled by diI

A diOlistic device was constructed using pipe fittings, a pressure gauge, solenoid, relay, push button, and battery-operated air pump (see Heffernan and Galvan, 2023 for complete details). To prepare carriers of DiI-coated gold particles, 50 mg of gold particles (0.8-1.3 µm in diameter) were mixed with a 1.5 mg DiI/100% ethanol solution. The solution was spread even on a coverslip, allowed to dry, and scraped into a tube containing distilled water. The tube was sonicated with intermittent vortexing for 15 minutes. The solution was then pipetted onto parafilm-covered #8 washers and allowed to dry. As described in Heffernan and Galvan, 2023, the parameters used for the diOlistic device included 100 psi of pressure, 3 cm distance from top of brain section, and 20 µm filter paper. Sections were "shot," rinsed with PBS and left to incubate for 24 hours at room temperature. Sections were incubated in PBS containing DAPI (5µg/mL) for 10 minutes. Sections were then mounted with Fluoromount-G (Southern Biotech)

on slides with 2 stacked 0.12mm deep coverslip spacers (Grace Bio-Labs) to reduce tissue compression.

DiI-labeled astrocytes were imaged using a Leica SP8 confocal microscope. Z-stacks were obtained with a 40x (NA 1.3) objective, 1024x1024 scan format, 2x optical zoom, and 0.35 µm z-steps resulting in an x-y pixel size of 0.13 µm x 0.13 µm. Stacks were converted to maximum intensity z-projections in ImageJ. The image was thresholded using the automated "Huang" method and binarized. An outlined area overlay of the cell territory was generated by using the "Analyze Particles" tool with a minimum particle size of 5 μm^2. The overlay generated area and Feret's maximum diameter (the longest edge to edge distance of the overlay). The binarized image was additionally subjected to box counting via the ImageJ FracLac plugin. The fractal dimension is defined as the slope of $\frac{\log (N)}{\log (r)}$ where N is the number of boxes and r is the inverse of box size. The raw z-stacks were also loaded into Imaris. The NIV analysis is described above for analysis of virally labeled astrocytes. Three ROIs were averaged for each cell, resulting in 30 ROIs and 10 NIV averages for mouse and 36 ROIs and 12 NIV averages for monkey.

2.3.3.4. Density of inhibitory terminals within astrocyte territories

To reduce autofluorescence in the tissue, all sections were subjected to "photobleaching" prior to incubations. The sections were placed in 6-well transparent plates containing PBS in a refrigerator (4°C) equipped with broad-spectrum white lights. The well-plates were placed on a rack directly above the lights and remained exposed to light for 4 days. Following photobleaching, sections were stained and coverslipped using the same procedure described for cell counts and virally labeled astrocytes. Transduced astrocytes were stained for mCherry (1:1000 rabbit) and GABAergic synaptic terminals for vgat (1:7500).

Astrocytes were imaged using a Leica SP8 confocal microscope. Z-stacks of 5.4 µm were obtained with a 63x (NA 1.4) objective, 1024x1024 scan format, 1.8x optical zoom, and 0.3 µm z-steps resulting in an x-y pixel size of 95 nm x 95 nm. Laser settings were kept identical across all images. Stacks of 6 images (1.8 µm) were converted to maximum intensity z-projections in ImageJ, resulting in 3 maximum intensity z-projections per astrocyte. The channel containing the astrocyte was thresholded and binarized. An outlined area overlay of the cell territory was generated by using the "Analyze Particles" tool with a minimum particle size of 5 μm^2. The channel containing the vgat underwent background subtraction with a rolling ball radius of 50 pixels and was thresholded using the "Moments" method in ImageJ. The number of terminals was then determined by using the "Analyze Particles" tool with a particle size range of 0.2-6 μm^2. The number of terminals within the astrocyte territory and area of the territory was recorded.

2.3.3.5. Immunohistochemistry: mCherry/GFP immunoperoxidase for brightfield and electron microscopy

To verify the location of AAV injections, sections were incubated in a solution of 1% normal serum, 1% BSA, and 0.3% Triton X-100 in PBS. Sections were then incubated overnight in the blocking/permeabilization solution containing antibodies for mCherry (1:2500 mouse or 1:1000 rabbit) or GFP (1:2000). Binding sites were revealed using a biotinylated secondary antibody (see Table 2.2, all 1:200). Sections were incubated in the secondary solution for 90 minutes and rinsed in PBS. Sections were then incubated in an ABC solution (1:200, Vector Laboratories) containing 1% BSA and 0.3% Triton X-100 for 90 minutes. Followed by rinses in PBS and TRIS buffering solution (0.05M, pH 7.6), sections were incubated in TRIS buffer containing 0.025% 3,3'-diaminobenzidine tetrahydrochloride (DAB; Sigma), 10 mM imidazole,

and 0.006% hydrogen peroxide for 10 minutes, immediately followed by PBS rinses. Following mounting, sections were dehydrated in a graded series of alcohol and toluene, then coverslipped. Slides were scanned with an Aperio Scanscope CS system (Leica).

For electron microscope analysis, sections were first treated with 1% sodium borohydride as above, before being placed in a cryoprotectant solution, frozen at −80°C to maximize antibody penetration and washed in serial dilutions of cryoprotectant in PBS. After blocking with 1% normal serum and 1% bovine serum albumin in PBS, the sections were incubated for two days at 4°C in the primary antibody. The avidin-biotin complex (ABC) method was used to amplify signal. The sections were incubated in biotinylated secondary antibodies for 2 hours (see Table 2.2, all 1:200), and in the ABC solution (1:100; Vectastain Standard kit, Vector) for 90 minutes. Sections were rinsed in PBS and TRIS buffer (0.05 M, pH 7.6) before being placed in DAB solution for 10 minutes. Next, sections were rinsed in PBS and kept at 4°C overnight. The sections were then placed in PB for 10 min to desalt and postfixed in osmium tetroxide (1% in PB). They were washed in PB and dehydrated in a series of ethanol and propylene oxide. The 70% ethanol solution contained 1% uranyl acetate. The sections were embedded in resin overnight and placed on slides before being placed in the oven for 48 hours at 60°C. Blocks from primary motor cortex were cut from each animal and glued on top of resin blocks. After facing, serial ultrathin sections were cut on an ultramicrotome (Leica Ultracut T2, Leica, Nussloch, Germany). Sixty nanometer thick sections from the surface of the block were collected on copper single slot grids and stained with lead citrate for 5 minutes.

Stained grids were examined on an electron microscope (EM Model 1011; Jeol, Peabody, MA, USA) coupled with a CCD camera (Gatan Model 785; Warrendale, PA, USA). Each section was scanned at 5,000x to identify immunoperoxidase labeling. Peroxidase-labeled elements were

imaged at 40,000x. Using ImageJ, elements were identified according to ultrastructural features.(Peters et al., 1991) Images containing peroxidase-labeled astrocytes and synapses were categorized based on their spatial relationship with labeled astrocyte processes. Astrocyte processes which touched the axonal terminal were considered "pre" contacts, astrocytes which touched a dendrite or dendritic spine were considered "post" contacts. If the astrocyte touched both the pre- and post-synaptic elements, it was considered a "cleft" contact. Additionally, the widths of cleft-associated astrocyte processes were measured in ImageJ. At the cleft, the astrocyte process was measured at an angle approximately parallel to the visible synapse. If the membrane integrity of the astrocytic process making cleft contact was compromised, the process was not included in the width measurements.

2.3.4. Analysis of scRNAseq dataset

Expression data from the astrocyte cluster of rhesus macaque striatal scRNAseq data was obtained from the authors of He et al., 2021. The original dataset contained 80,902 cells and identified 31,258 genes. The astrocyte cluster contained 17,424 cells with an average of 2,672 genes per astrocyte. Within the astrocyte cluster, 5,813 astrocytes were from putamen, 7,800 from nucleus accumbens, and 3,811 from caudate. The differentially expressed genes for the striatal astrocyte cluster (containing putamen, nucleus accumbens, and caudate) were generated using Seurat's *FindMarkers* function and are available as supplemental information in (He et al., 2021). We then mined the rhesus macaque astrocyte cluster for a list of morphologically-associated genes in mouse astrocytes from previously published data.(Endo et al., 2022) We obtained the average expression of morphologically-associated genes in the rhesus macaque astrocyte cluster using Seurat's *AverageExpression* function.

Table 2.2. Antibodies

Antibody	Catalogue Number	Antibody Registry	Lot Number	Dilution
mCherry mouse	Takara 632543	AB_2307319	2111858A	1:2500
mCherry rabbit	Abcam AB167453	AB_2571870	1024587	1:1000
GFP chicken	Millipore 06-896	AB_11214044	DAM1543699	1:2000
NeuN rabbit	Millipore ABN78	AB_10807945	3974817	1:10000
Aldh1L1 mouse	UCDavis 75-140	AB_10673448	41-4BK-67	1:3000
S100β mouse	Abcam AB7852	AB_306138	GR3435645-1	1:200
GFAP rabbit	Abcam AB7260	AB_305808	3132965	1:5000
VGAT mouse	R&D MAB6847	AB_2814814	CGAJ0111111	1:7500
Fab donkey anti-mouse IgG	Jackson Lab	AB_2307338	NA	1:100
DAPI	Invitrogen D-1306	AB_2629482	2031179	5ug/ml
Donkey anti-mouse FITC	Jackson Lab 715-095-	AB_2340792	152099	1:100
Donkey anti-mouse RRX	Jackson Lab 715-295-	AB_2340831	158805	1:100
Donkey anti-rabbit FITC	Jackson Lab 711-095-	AB_2315776	157917	1:100
Donkey anti-rabbit RRX	Jackson Lab 711-295-	AB_2340613	154859	1:100
Donkey anti-chicken FITC	Jackson Lab 703-095-	AB_2340356	152661	1:100

2.3.5. Statistical analysis and figures

Data were first tested for normality using the D'Agostino-Pearson test. If the data was normally distributed, two group comparisons were made using two-tailed unpaired t-tests. Welch's correction was implemented for any analyses in which there were significantly unequal variances between groups. For analyses with more than two groups, 2-way repeated measure ANOVA followed by Holm-Sidak's test for multiple comparisons were run. For data that was not normally distributed, two group comparisons were made using unpaired Mann-Whitney tests. To evaluate the relationship between two variables, linear regressions or Pearson correlation was performed. The results of statistical analysis, n, and p-values are included in figure legends. N is defined as number of animals or cells depending on analysis and is described in the figure legend. Statistics were run using GraphPad Prism 9. Data are represented as mean ± SD. In all figure plots, p-values are represented by asterisk(s): $*$ for $p < 0.05$; $**$ for $p < 0.01$; $***$ for $p < 0.001$; $****$ for $p < 0.0001$. All schematics for figures were made using BioRender.com.

2.4. RESULTS

2.4.1. Strategy

We studied astrocytes from 4 functionally connected regions of the adult rhesus macaque and mouse brain: putamen/dorsolateral striatum (STR), external globus pallidus/globus pallidus (GPe), primary motor cortex (MCX), and primary somatosensory cortex (SCX). To assess potential cortical layer-specific differences, layers 2/3 and 5 were examined. We first investigated astrocyte density, neuron density, and astrocyte-to-neuron ratio in all 4 regions. We then investigated astrocyte primary branching structure using glial fibrillary acidic protein (GFAP) in layer 5 of primary motor cortex. To further investigate astrocyte morphology, we utilized an astrocyte-targeting adeno-associated virus (AAV) as well as diOlistics in striatum and cortex. Lastly, we characterized astrocyte ultrastructural relationships with synapses using 2D electron microscopy in primary motor cortex.

2.4.2. Astrocyte density is conserved across species and brain regions while neuron density varies considerably

We first examined neuron and astrocyte densities across different brain regions in mouse and rhesus macaque. Neurons and astrocytes were labeled by immunohistochemistry (IHC) for NeuN (neurons) and a cocktail of S100β/Aldh1L1 (astrocytes) and counterstained with DAPI (Figure 2.1A-C). Neuron densities varied by brain region in both species, though in all examined regions, densities were lower in monkeys (Figure 2.1D). Both brain regions ($F_{5,20}$ =19.79, $p<0.0001$, 2-way RM ANOVA) and species ($F_{1,4}$ = 184.6, p=0.0002, 2-way RM ANOVA) had significant effects on neuron density. Neuron density was significantly lower in monkeys than mice in striatum (p=0.0002, Sidak's test), motor cortex (L5 p=.0003; L2/3 p=0.003, Sidak's test), and somatosensory cortex (L5 p=0.0323; L2/3 p=0.0308, Sidak's test). In contrast, astrocyte densities were comparable between species and across most brain regions (Figure 2.1E). Brain region ($F_{5,20}$ =29.51, $p<0.0001$), but not species ($F_{1,4}$ = 2.604, p=0.1819), had a significant effect

on astrocyte density. Astrocyte density only varied significantly between mice and monkeys in the globus pallidus, where the density of astrocytes was higher in mice than monkeys ($p=0.0002$, Sidak's test).

In all brain regions except for the globus pallidus, the astrocyte density was lower than neurons (Figure 2.1E). The astrocyte-to-neuron ratio was also slightly higher in monkeys in all regions. However, this difference was only significant in the globus pallidus, which was driven by the higher neuronal and astrocyte densities in the mouse compared to monkey (Figure 2.1F). While there was not a consistent astrocyte-to-neuron ratio across structures or species, astrocyte and neuron density showed a weak negative correlation (Spearman correlation, $r = -0.4755$, $p=0.1215$) (Figure 2.1G). Taken together, these data suggest that astrocyte density is not dependent on neuronal density and is largely consistent across structures and species, even when neuronal density is variable.

2.4.3. Gross astrocyte morphological features across brain regions

Astrocytes within the striatum and motor cortex displayed similar morphology, reminiscent of canonical protoplasmic astrocytes of gray matter (Figure 2.2). The characteristically bushy shape was evident in both primate and mouse astrocytes. Interestingly, astrocytes within the GPe in both species displayed fewer branches than astrocytes in the striatum and motor cortex (Figure 2.2). Specifically, within primates, GPe astrocytes ignore territory borders, with long processes extending into the domains of neighboring astrocytes which are reminiscent of fibrous astrocytes (Figure 2.2). Given the low density of neurons in the GPe compared to other brain regions (Figure 2.1), the gross morphology of astrocytes and degree of branching could be partially driven by neuronal density.

2.4.4. Astrocyte primary branching scales with territory size

Individual astrocytes can interact with multiple neurons within their territory. The results examining neuron and astrocyte densities suggest that the territory of individual astrocytes in mice survey a greater number of neurons than in monkeys. For example, in the mouse striatum there are approximately 6 neurons/astrocyte versus 3 neurons/astrocyte in monkey striatum (inverse of astrocyte-to-neuron ratio, Figure 2.1). Next, we studied the gross and fine structure of astrocytes to examine how the morphology of these cells may relate to the cellular and chemical composition of their environment in each species. Subsequent analyses were conducted in primary motor cortex and/or striatum to address whether species differences in astrocyte morphology are present in a functionally connected area of cortex and subcortical structure.

To assess the primary branching structure of astrocytes, we used GFAP immunohistochemistry in mouse and monkey primary motor cortex. We chose layer 5 to avoid layer 1 interlaminar astrocyte processes which traverse layers 2-4 in monkey.(Falcone et al., 2021b) We did not include striatal astrocytes in this analysis because the striatum does not express an abundance of GFAP (Chai et al., 2017). Using 2D analyses, we determined the area and maximum diameter of the GFAP-immunoreactive astrocyte territory (Figure 2.3A-C). When compared to mouse, monkey astrocytes displayed a 2x larger territory area ($p<0.0001$, t-test with Welch's correction) and 1.4x larger diameter ($p<0.0001$ t-test) (Figure 2.3D-E). These data are consistent with previous studies (Oberheim et al., 2009). Sholl analysis revealed that monkey astrocytes displayed a higher number of GFAP+ branches (Figure 2.3F)(Sholl, 1953). We also quantified the number of primary branches for each astrocyte by counting those that arose from the soma (Figure 2.3G). Monkey astrocytes displayed 7 primary branches on average, versus 4 in mice ($p<0.0001$, t-test with Welch's correction). However, when accounting for the species differences in territory area, the maximum number of GFAP+ Sholl intersections was not

significantly different between species (Figure 2.3H). Further, the number of Sholl intersections increased with territory size within each species (Figure 2.3I).

Using GFAP immunostaining, we also looked for the previously described and morphologically distinct subtype of primate astrocytes, the varicose-projection astrocyte (VPA). VPAs have only been identified in humans and apes (Falcone et al., 2021a; Oberheim et al., 2009). However, we report the presence of varicosities on GFAP+ astrocytes in rhesus macaque cortex (Figure S2.1). Varicosities were found in one animal in layer 5 of the cortex, though we were unable to trace the process to the cell body of origin. The cell body is likely to reside in layer 5, layer 6, or white matter.

2.4.5. Primate astrocyte territory areas are larger with lower neuropil infiltration volumes

Although GFAP is widely used to identify astrocytes and assess morphology, it is not expressed in the finer branches and processes of astrocytes (Bushong et al., 2002). To assess species differences in fine morphological detail beyond primary branching structure, we injected AAV5-GfaABC1D-tdTomato or Lck-GFP (Figure S2.2). Since the promoter had not been used in primates before, we recently characterized the specificity and efficiency in the rhesus macaque. As described (Heffernan et al., 2022), the promoter has high specificity for astrocytes in the rhesus macaque brain with limited transduction in neurons and oligodendrocytes. The activity of the GfaABC1D promoter in mice has been previously well-described (Lee et al., 2008; Yu et al., 2020).

Following staining with antibodies against mCherry (to detect tdTomato) or GFP, astrocytes were identified and imaged. For subsequent analyses, astrocytes selected for imaging had to 1) be well-isolated from other labeled cells, 2) display adequate signal-to-noise ratio, 3) reside within layer 5 of primary motor cortex or putamen in monkeys or dorsolateral striatum in mice, and 4) have their nuclei visible within the slice. Since brain sections were 60 µm thick, we

did not acquire stacks containing entire astrocytes in the z-dimension. We verified that the image depth acquired in the z dimension did not determine astrocyte territory volume or Feret's diameter (Figure S2.3C-D). The theoretical 3D shape of an astrocyte is approximately spherical with the soma in the center, and thus, by ensuring that all measured astrocytes had a visible soma in the acquired stack, we effectively measured the largest possible territory in the x-y dimensions for each cell. In addition, we verified that the territory areas did not differ between the two fluorophores used (one monkey received AAV with GFP-Lck, while all other animals received tdTomato, Figure S2.3B). Astrocytes in primate primary motor cortex also displayed a 1.5-fold larger territory area ($p<0.0001$, t-test with Welch's correction) and 1.3-fold larger diameter ($p<0.0001$, t-test with Welch's correction)(Figure 2.4B, top). Similarly, astrocytes in primate striatum displayed a 1.5-fold larger territory area ($p<0.0001$, t-test with Welch's correction) and 1.3-fold larger diameter ($p<0.0001$, t-test with Welch's correction) compared to rodent striatal astrocytes (Figure 2.4B, bottom). To assess the distribution and density of fine branches within an astrocyte territory, we measured the neuropil infiltration volume (NIV) (Baldwin et al., 2021; Stogsdill et al., 2017). Remarkably, despite larger territories, we found that the NIV of monkey astrocytes was 1.8-fold smaller than mouse in both primary motor cortex ($p<0.0001$, t-test with Welch's correction) and striatum ($p<0.0001$, t-test)(Figure 2.4G-I).

Using GFAP immunoreactivity, we established that primary branching structure of the astrocyte is conserved between mouse and monkey. Further, with viral-mediated expression of fluorescent tag proteins, we found that the territory and diameters of primate astrocytes are larger in monkeys than mice, while mice have increased NIV compared to monkeys. Given that astrocyte branching structure may be severely affected by chemical fixation (Korogod et al., 2015), and viral labeling methods to transduce astrocytes may trigger a reactive phenotype, it

was possible that our observations resulted from species differences in fixation and astrocyte reactivity. Thus, to complement the viral-mediated labeling technique, we forwent transcardial fixation for a short immersion fixation period and utilized a diOlistic labeling method (Figure 2.5) to assess cortical astrocyte morphology. Consistent with our results in virally labeled and perfusion-fixed tissue (Figure 2.4), diOlistically-labeled cortical astrocytes in mice and monkeys displayed similar overall complexity in 2D as measured by fractal dimension (Figure 2.5E). In addition, similar to our results obtained with the AAV labeling method, monkey astrocytes displayed sparser astrocytic infiltration of the neuropil ($p=0.0164$, t-test)(Figure 2.5G).

2.4.6. Primate and mouse astrocyte territories cover the same number of axon terminals

Since we found a significant difference in astrocyte territory between species, we next investigated whether mouse and monkey astrocyte territories covered a comparable number of axonal terminals in primary motor cortex and striatum. We focused on inhibitory terminals because of the extensive literature on interneuron expansion across evolution, and thus suspected that they would reveal the greatest potential species differences (Krienen et al., 2020; Tepper and Bolam, 2004; Wildenberg et al., 2021). The analysis was conducted in virally labeled astrocytes (Figure 2.6). The territory of individual astrocytes in primary motor cortex in mice and monkeys encompassed a similar number of vgat+ axon terminals per territory ($p=0.7120$, t-test). The similarity of terminal numbers between species, despite larger territory size in the monkey, was due to a lower density of inhibitory terminals in monkey ($p<0.0001$, t-test)(Figure 2.6C-D). Interestingly, in the striatum, both vgat terminal density ($p<0.0001$, t-test with Welch's correction) and the number of vgat terminals per astrocyte territory ($p<0.0001$, Mann-Whitney)(Figure 2.6E-F) were lower in monkey.

2.4.7. Astrocyte-synapse relationships are the same in mouse and monkey

To assess spatial relationships between astrocytes and neuronal synapses, we prepared blocks of primary motor cortex from AAV5-GfaABC1D-injected animals for transmission electron microscopy. Astrocyte processes in contact with pre and/or post-synaptic elements were categorized as pre-synaptic, post-synaptic, or cleft-associated astrocytes (Figure 2.7B-D). The proportions of astrocyte contact types were similar between mouse and monkey with the majority (around 75%) of astrocyte processes contacting the synaptic cleft (Figure 2.7E). Given that the viral method used to label astrocytes may not transduce all astrocytes, we did not assess the proportion of synapses not contacted by astrocytes. Thus, our results do not inform about the proportion of synapses with or without astrocyte contacts. There are possible unexplored differences in the proportion of synapses without astrocyte contact between species.

Since we found that primate astrocytes displayed lesser neuropil infiltration volumes, we sought to determine whether primate astrocytes had smaller fine processes which would explain the disparity. Astrocyte processes are not simple cable structures, and thus we needed to determine a consistent method to measure processes by standardizing the location on the astrocyte and angle for the measurement. We measured cleft-associated astrocyte processes at the interface that touched the synaptic cleft and at an angle approximately parallel to the synapse. We found that the smallest astrocytic units, perisynaptic astrocytic processes (PAPs), are slightly smaller in monkeys than in mice ($p=0.0325$, Mann-Whitney). Monkey PAPs measured 222.3 nm on average compared to 258 nm for mouse (Figure 2.7F). The small differences in astrocyte PAP size may partly contribute to the species differences in NIV.

2.4.8. Primate and rodent astrocytes share morphologically-associated genes

Given the differences in astrocyte territory size and branching between species, we wondered what genes may influence morphological features. While species differences in astrocyte gene expression have been previously described, genes that regulate astrocyte

morphology in the primate are unexplored (Zhang et al., 2016). In mice, relating astrocyte morphological attributes to RNA-seq across 13 different brain regions using weighted gene co-expression network analysis (WGCNA) yielded a list of the top 5% morphologically-associated genes (Endo et al., 2022). We mined a rhesus macaque striatal single nucleus RNA-seq dataset(He et al., 2021) for the list of genes in Endo et al., 2022 (Figure 7A). Out of 50 genes, 47 were expressed in the rhesus macaque dataset with *SLC1A2*, *NTM*, *TCF4*, *SIK3*, *RGS20*, *DENND1A*, *RORB*, *SRGAP3*, *PANTR1*, and *CPEB4* showing the highest average expression (Figure 2.8B). The morphologically associated genes *SLC1A2*, *RGS20,* and *RORB* were also among the top astrocyte-enriched genes in the striatum (Figure 2.8C). These data suggest that the molecular correlates of astrocyte morphological complexity may be shared between mouse and primate.

2.5. DISCUSSION

A growing interest in glial cells has generated a myriad of new studies focused on the role of astrocytes in health and disease. While the literature concerning murine astrocytes has grown substantially, the field knows little about primate astrocytes due to technical and resource limitations. By using a variety of techniques to investigate astrocyte morphology in mice and rhesus macaques, we found a great deal of similarity between species.

We found that mice and monkeys displayed similar astrocyte densities despite varying neuronal densities. The astrocyte-to-neuron ratios were slightly higher in monkeys across all brain regions, though this was largely driven by differences in neuronal densities between the species. At the level of an individual astrocyte, monkey astrocytes displayed greater GFAP branching. However, the density of GFAP+ branches within an astrocyte territory were comparable between mouse and monkey due to the increased territory size of primate astrocytes. Taken together, our data shows that the primary branching of astrocytes is similar between

mouse and monkey. Our data also suggests that monkey astrocytes show a greater degree of territory overlap due to a similar density of astrocytes across species but larger astrocyte territory area in monkey. Our results are consistent with the finding that human astrocytes show a greater degree of overlap than mouse (Oberheim et al., 2009). Further studies are needed to investigate the potential molecular underpinnings of astrocyte territory organization in the primate. A wealth of genes that regulate territory formation have been identified in mice and we showed the majority of those genes are expressed in rhesus macaque astrocytes (Baldwin et al., 2021; Endo et al., 2022). However, a different or additional set of genes may be involved in territory regulation in the primate since our data suggest greater territory overlap in primate astrocytes.

To further test the hypothesis that mouse astrocytes were of similar complexity to monkey astrocytes, we measured neuropil infiltration volumes (NIVs) to assess the degree of fine process branching and extension into the surrounding neuropil (Baldwin et al., 2021; Stogsdill et al., 2017). Unexpectedly, we found a lower NIV in monkeys. This is notable because it was previously suggested that primate astrocytes were more complex than rodent (Oberheim et al., 2009). However, we do not interpret this lower NIV as a decrease in complexity. We suspect that the degree of branching between mouse and monkey astrocytes is the same, but due to the increased territory area in monkeys, the spacing between branches is greater when measured in volume. Differences in NIV were not entirely explained by differences in astrocyte process size. By measuring the dimension of perisynaptic astrocyte processes (PAPs) parallel to the adjacent synapse in electron micrographs, we found that the distribution of PAP sizes were only marginally smaller in monkeys compared to mice. Thus, the smallest fundamental unit of the astrocyte is similar across species.

There are functional implications from the assessed morphological features of astrocytes in this study. Astrocytes are known modulators of neuronal synapses, whether through the secretion of synaptogenic molecules (Allen and Lyons, 2018), clearance of neurotransmitters (Murphy-Royal et al., 2017), or release of neuroactive species (Araque et al., 2014). Alterations in the distance of PAPs to synapses could impact such functions (Bernardinelli et al., 2014; Kater et al., 2023). We therefore investigated if the spatial relationship between astrocytes and synapses were different between species in primary motor cortex. Synapses in monkey and mouse were contacted by PAPs in a similar fashion. The majority of synapses, around 75%, were contacted at the cleft, while few synapses were only contacted at their presynaptic or postsynaptic elements. Identifying astrocyte processes without labeling in 2D electron microscopy can be extremely challenging and unreliable, thus we relied on expression and immunoperoxidase labeling of tag proteins (tdTomato and GFP) under the GfaABC1D promoter. Since the expression of tag proteins can vary in an area of tissue and even within an individual cell, any assessment of synapses without astrocyte processes could have been due to a lack of transduction or lower levels of expression, rendering false-negative results. Therefore, it is possible that a different proportion of synapses are not contacted by PAPs across species. Additionally, we did not characterize symmetric versus asymmetric synapses, thus there could be species differences in the spatial relationship with a specific synapse type. Even so, we surmise that the core functions of astrocytes related to synapse formation, maintenance, and elimination are, in all likelihood, the same across species.

We determined that astrocytes in mouse and monkey have common spatial relationships with neuronal synapses, but we also investigated whether they interacted with a comparable number of synapses. It was proposed that primate astrocytes govern a significantly larger number

of neuronal synapses, implying a greater functional capacity and complexity than rodents (Oberheim et al., 2009). However, based on estimated synapse densities in human and mouse (10.34 and 23.28 $x10^8$ per mm^3 of layer 5 in cortex, respectively)(DeFelipe et al., 2002), we hypothesized that the synapse density inversely scaled with astrocyte territory size such that the number of synapses governed per astrocyte territory would be comparable between species. We focused on inhibitory synapses given the literature on interneuron expansion across evolution, and thus suspected that they would reveal the greatest potential species differences (Krienen et al., 2020; Wildenberg et al., 2021). Our data shows that the density of inhibitory synapses in primary motor cortex is higher in mice, but that mouse and monkey astrocytes govern a similar number of inhibitory synapses by territory area. The differences in synapse density between species are consistent with previous studies (DeFelipe et al., 2002; Wildenberg et al., 2021). Interestingly, the number of inhibitory synaptic terminals governed by an astrocyte in the striatum is significantly lower in monkeys than mice. This suggests that there may be region-specific differences in astrocyte morphology and function across species which should be investigated in future studies.

Our findings highlight the similarities between mouse and monkey astrocytes and add much needed clarity to the commonly held belief that primate astrocytes are more complex than rodent. We find that while territory sizes are larger for primate astrocytes, their morphology and synapse interaction negatively scale with increased size. Thus, the supposed computational power of astrocytes, if any, may be equivalent across species. Our study raises the question whether astrocyte territory size scales with increases in brain volume across all mammals, or if this increase is primate specific. Additionally, while the larger size of primate astrocytes does not result in increased synapse interaction and neuronal modulation, greater size could contribute to

greater vulnerability to oxidative stress (Li et al., 2021). It is conceivable that the core functions of astrocytes are shared across species, but the larger size of astrocytes in primates and perhaps humans make them more susceptible to insult. The functional relationship between astrocyte size and vulnerability to disease should be resolved in future studies. Overall, we provide a comprehensive assessment of astrocyte morphology in mouse and monkey, with significant implications for astrocyte morphology across primates, including humans. Our data inform future disease-related, physiological, and computational studies of astrocytes.

2.6. LIMITATIONS

We would be remiss if we did not discuss the limitations of this study. First and foremost, while we speculate that the morphological differences and similarities across species found in this study is applicable to human astrocyte morphology, we do not assess human astrocyte morphology. We also cannot address any species sex differences due to animal availability. We used a mix of male and female animals across experiments, but individual experiments only had female or male mice. Lastly, as this is a morphological study, we can only hypothesize about functional differences or similarities between species. Our findings nonetheless provide the basis to address these limitations in years ahead.

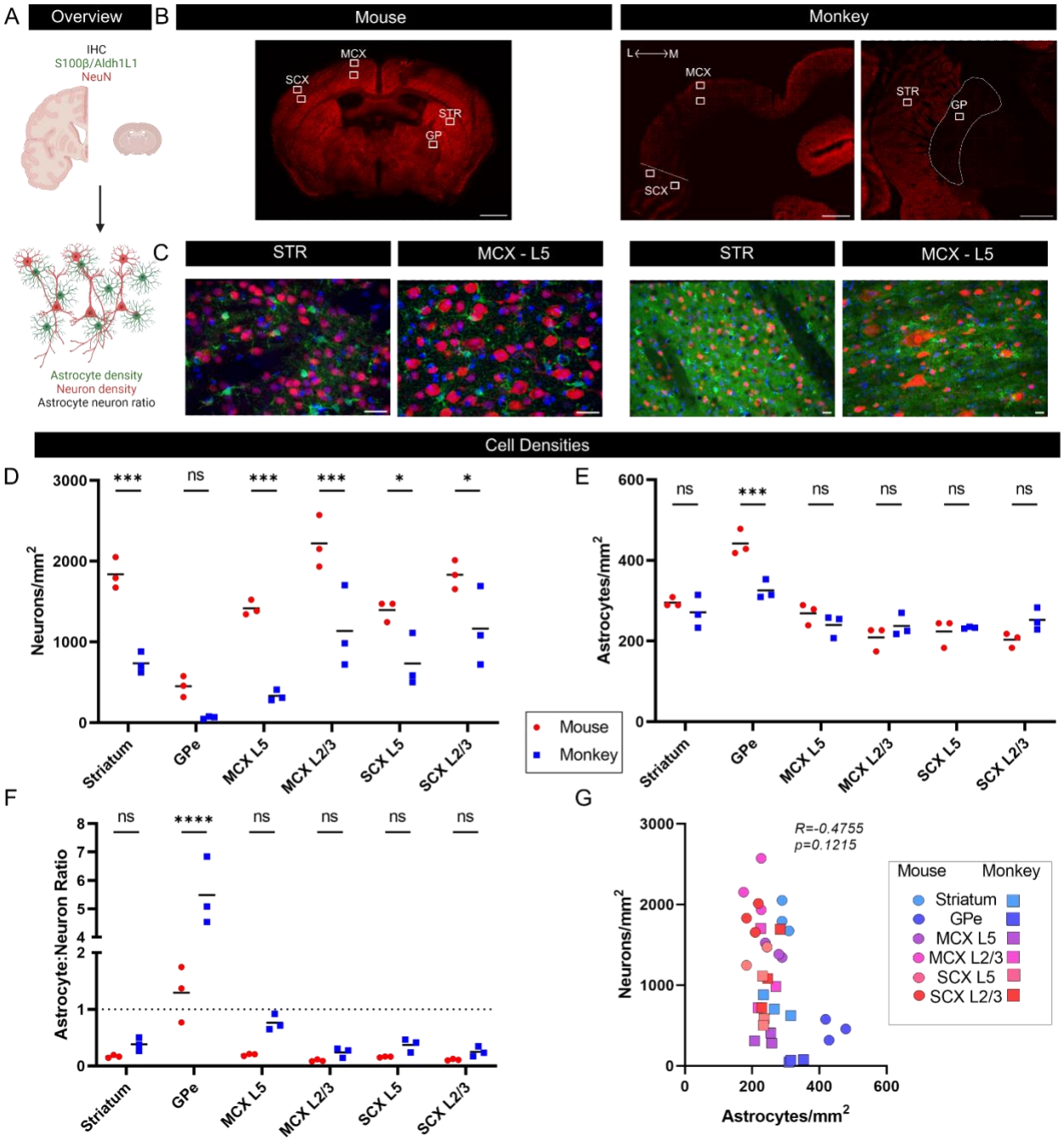

Figure 2.1 Astrocyte and neuron densities across the monkey and mouse brain.
(A) Overview of experiment: staining of mouse and monkey brain sections containing motor cortex, somatosensory cortex, striatum, and globus pallidus for astrocytes (Aldh1L1/S100β) and neurons (NeuN). Astrocyte densities, neuron densities, and astrocyte to neuron ratios were obtained. (B) Representative example of sampled brain regions from mouse (left) and monkey (right). SCX, somatosensory cortex; MCX, motor cortex; STR, striatum; GP, globus pallidus. Scalebars 2mm. (C) Representative examples of astrocyte (green) and neuron (red) labeling in striatum and motor cortex in mouse (left) and monkey (right), scalebars 20 µm. (D) Neuron

density measurements. 2-way repeated measures ANOVA, Sidak's multiple comparisons. (E) Astrocyte density measurements. 2-way repeated measures ANOVA, Sidak's multiple comparisons. (F) Astrocyte-to-neuron ratio measurements. 2-way repeated measures ANOVA, Sidak's multiple comparisons. (G) Correlation between astrocyte and neuron densities (Spearman correlation, r = -0.4755, p=0.1215). All data are shown as means (nmouse = 3, nsections=9; nmonkey = 3, nsections=9 per brain region).

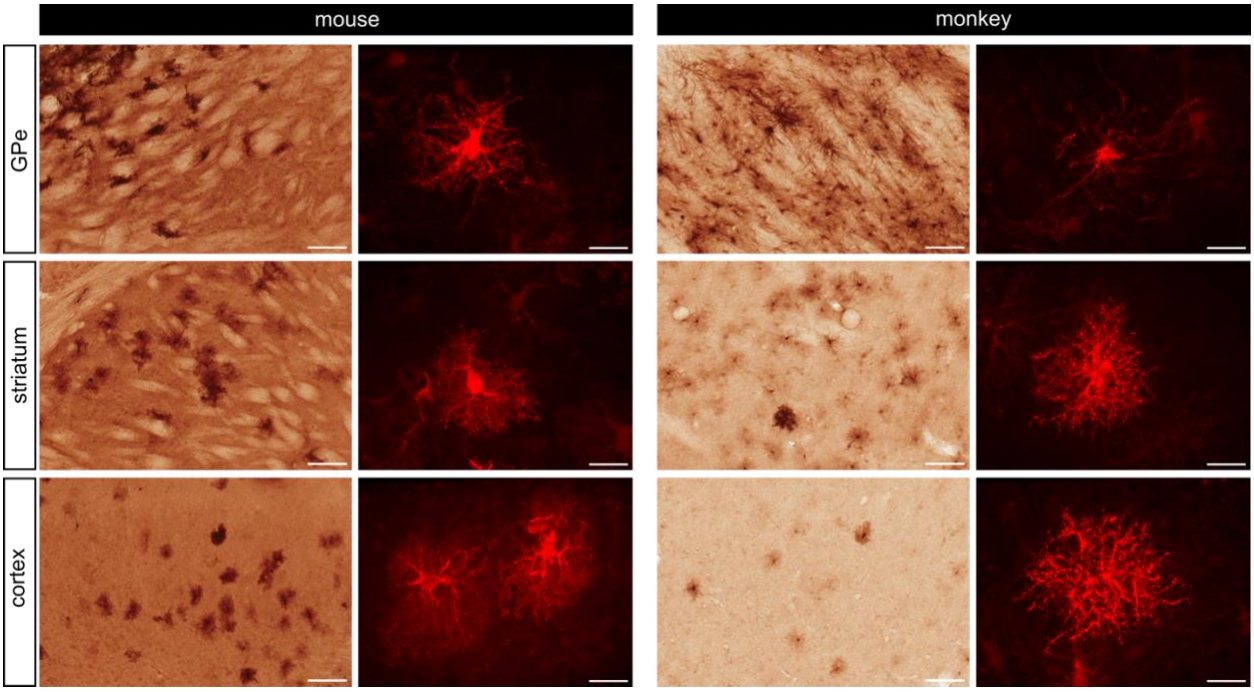

Figure 2.2 Gross astrocyte morphology across brain regions.
Representative examples of astrocyte tiling and gross morphology in GPe (top), striatum (middle), and motor cortex (bottom) in mice (left) and monkeys (right). Scalebars 100 µm for peroxidase images and 20 µm for fluorescent images.

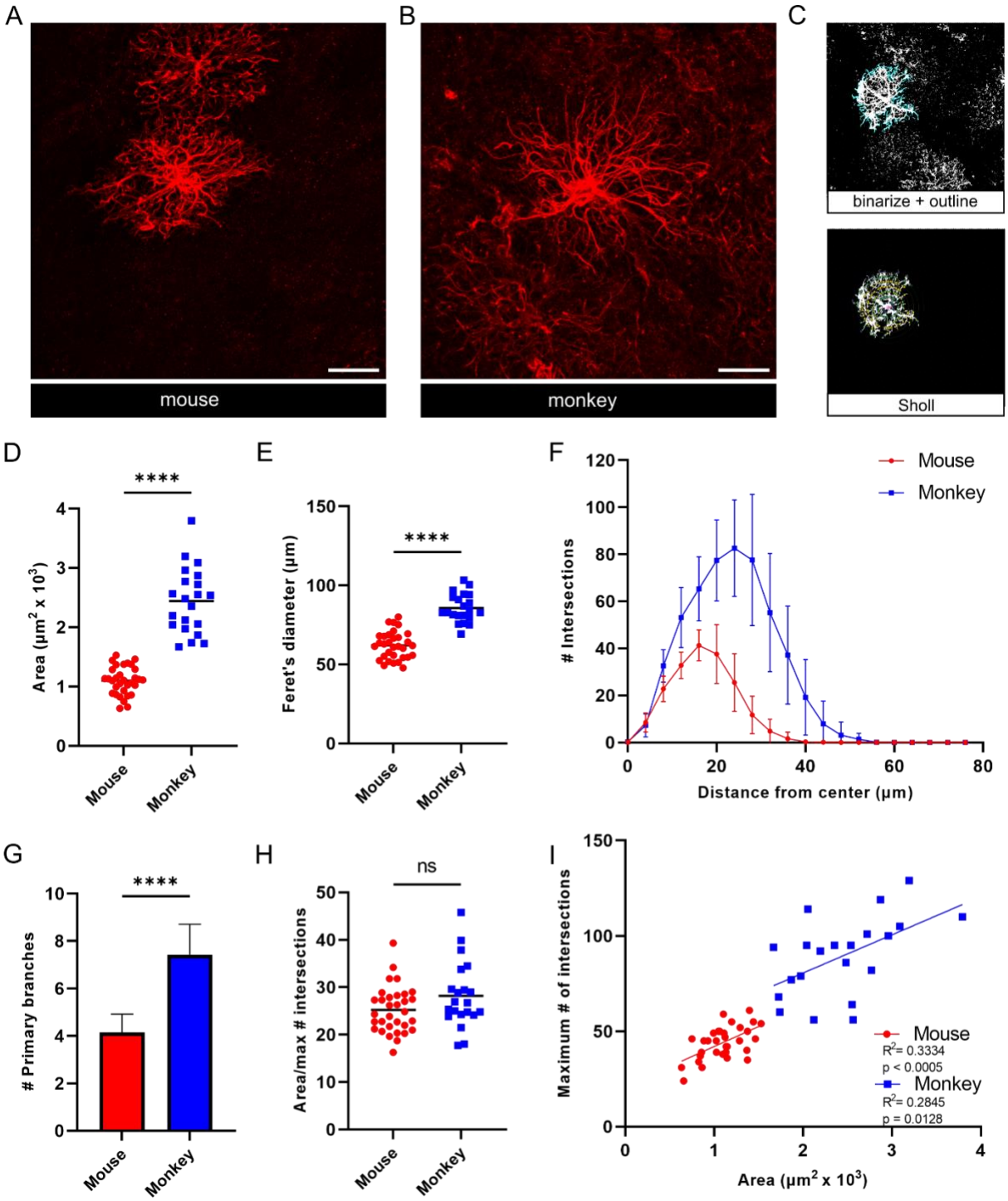

Figure 2.3 Astrocyte primary branching with GFAP.
(A) Representative maximum intensity z-projection of GFAP+ astrocyte in layer 5 of mouse motor cortex. (B) Representative maximum intensity z-projection of GFAP+ astrocyte in layer 5 of monkey motor cortex. All scalebars 20 µm. (C) Steps of processing: binarization, territory outline, and Sholl analysis. (D-E) Territory area ($p<0.0001$, t-test) and Feret's maximum

diameter ($p<0.0001$, t-test) of mouse and monkey GFAP+ astrocytes ($N_{monkey}= 2$, $N_{cells}= 21$ $N_{mouse}= 6$, $N_{cells}= 32$). (F) Sholl analysis of individual astrocyte morphologies. Data are represented as mean ± SD. (G) Number of GFAP+ primary branches in individual astrocytes ($p<0.0001$, t-test). Data are represented as mean ± SD. (H) Complexity ratio: territory area/maximum number of intersections ($p=0.0754$, t-test). (I) Linear regressions of maximum number of intersections and area.

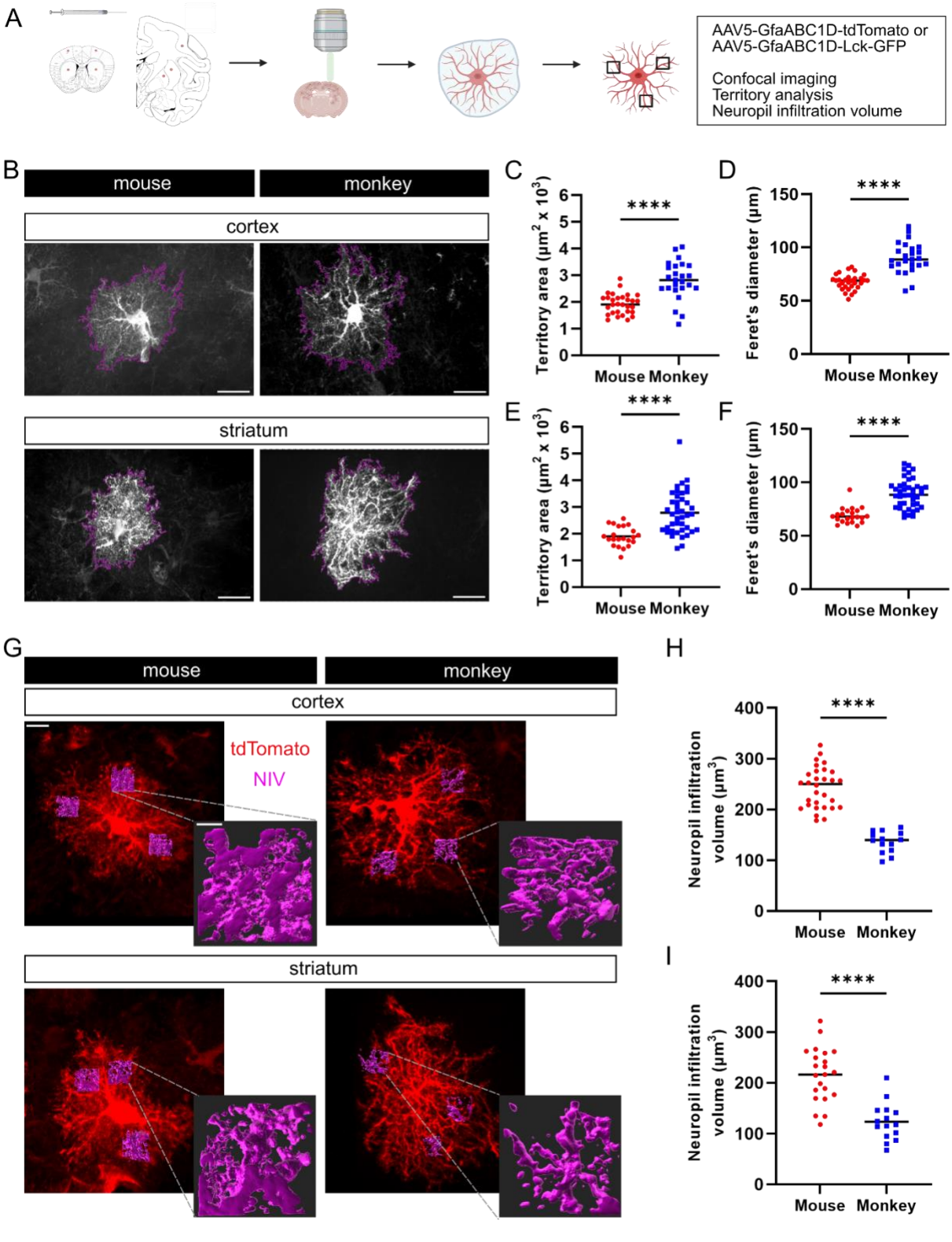
A
AAV5-GfaABC1D-tdTomato or
AAV5-GfaABC1D-Lck-GFP
Confocal imaging
Territory analysis
Neuropil infiltration volume
B
mouse
monkey
cortex
striatum
C
Territory area (μm² x 10³)
Mouse Monkey
****
D
Feret's diameter (μm)
Mouse Monkey
****
E
Territory area (μm² x 10³)
Mouse Monkey
****
F
Feret's diameter (μm)
Mouse Monkey
****
G
mouse
monkey
cortex
tdTomato
NIV
striatum
H
Neuropil infiltration volume (μm³)
Mouse Monkey
****
I
Neuropil infiltration volume (μm³)
Mouse Monkey
****

Figure 2.4 Comparison of astrocyte territories after viral transduction with the GfaABC1D promoter.

(A) Schematic of experimental procedure. (B) Example maximum intensity z-projections or astrocytes in mouse and monkey motor cortex layer 5 and striatum (putamen in monkey and dorsolateral striatum in mouse). All scalebars 20 µm. (C-D) Territory area ($p<0.0001$, t-test with Welch's correction) and Feret's maximum diameter ($p<0.0001$, t-test with Welch's correction) of cortical astrocytes ($N_{monkey}= 3$, $N_{cells}= 25$, $N_{mouse}= 5$, $N_{cells}= 30$). (E-F) Territory area ($p<0.0001$, t-test with Welch's correction) and Feret's maximum diameter ($p<0.0001$) of striatal astrocytes ($N_{monkey}= 2$, $N_{cells}= 41$, $N_{mouse}= 5$, $N_{cells}= 22$). (G) Representative examples of sites for neuropil infiltration volume (NIV) analysis in mouse (left) and monkey (right) in primary motor cortex (top) and striatum (bottom). Scalebar 10 µm on overview image and 2 µm on inset. (H) Neuropil infiltration volume ($p<0.0001$, t-test with Welch's correction) of cortical astrocytes ($N_{monkey}= 2$, $N_{cells}= 14$, $N_{mouse}= 5$, $N_{cells}= 30$). (I) Neuropil infiltration volume ($p<0.0001$, t-test) of striatal astrocytes ($N_{monkey}= 2$, $N_{cells}= 15$, $N_{mouse}= 5$, $N_{cells}= 22$). Only animals injected with AAV5-GfaABC1D-tdTomato were included in NIV analysis.

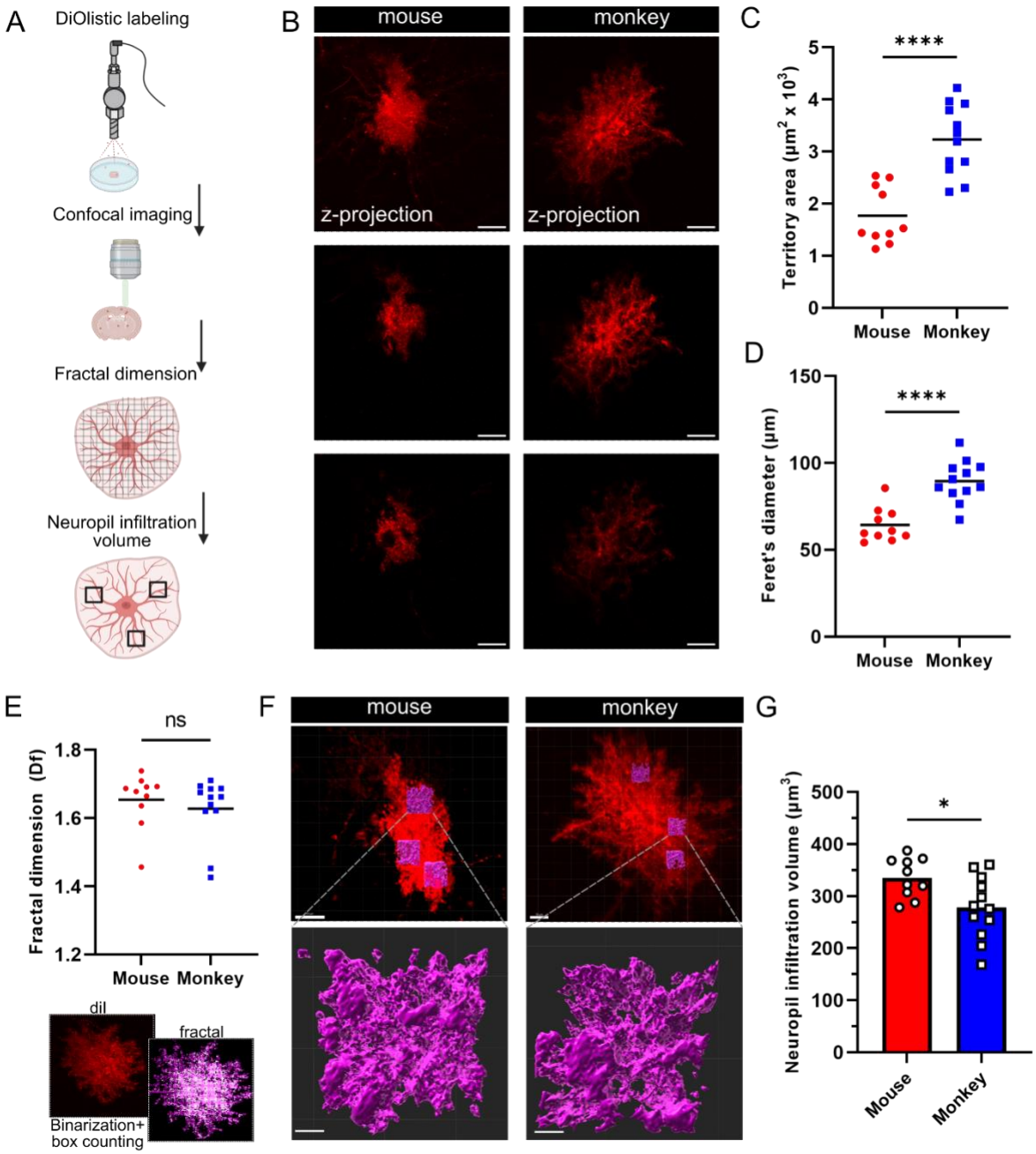

Figure 2.5 Morphology of fine astrocyte processes using diOlistics.
(A) Experimental overview. (B) Representative examples of diI-labeled astrocytes in mouse (left) and monkey (right). Maximum intensity z-projections (top) and individual slices (middle and bottom) of each cell. Scalebars 20 µm. (C-D) Territory area ($p<0.0001$, t-test, $N_{mouse}=6$ $N_{cells}= 10$, $N_{monkey}=2$ $N_{cells}= 12$) and Feret's diameter ($p<0.0001$, t-test) of cortical diI-labeled astrocytes. (E) Fractal dimension box counting ($p=0.4961$, t-test). (F) Representative examples of neuropil infiltration volume (NIV) sites and surface reconstructions in mouse (left) and monkey (right). (G) Neuropil infiltration volumes ($p=0.0164$, t-test).

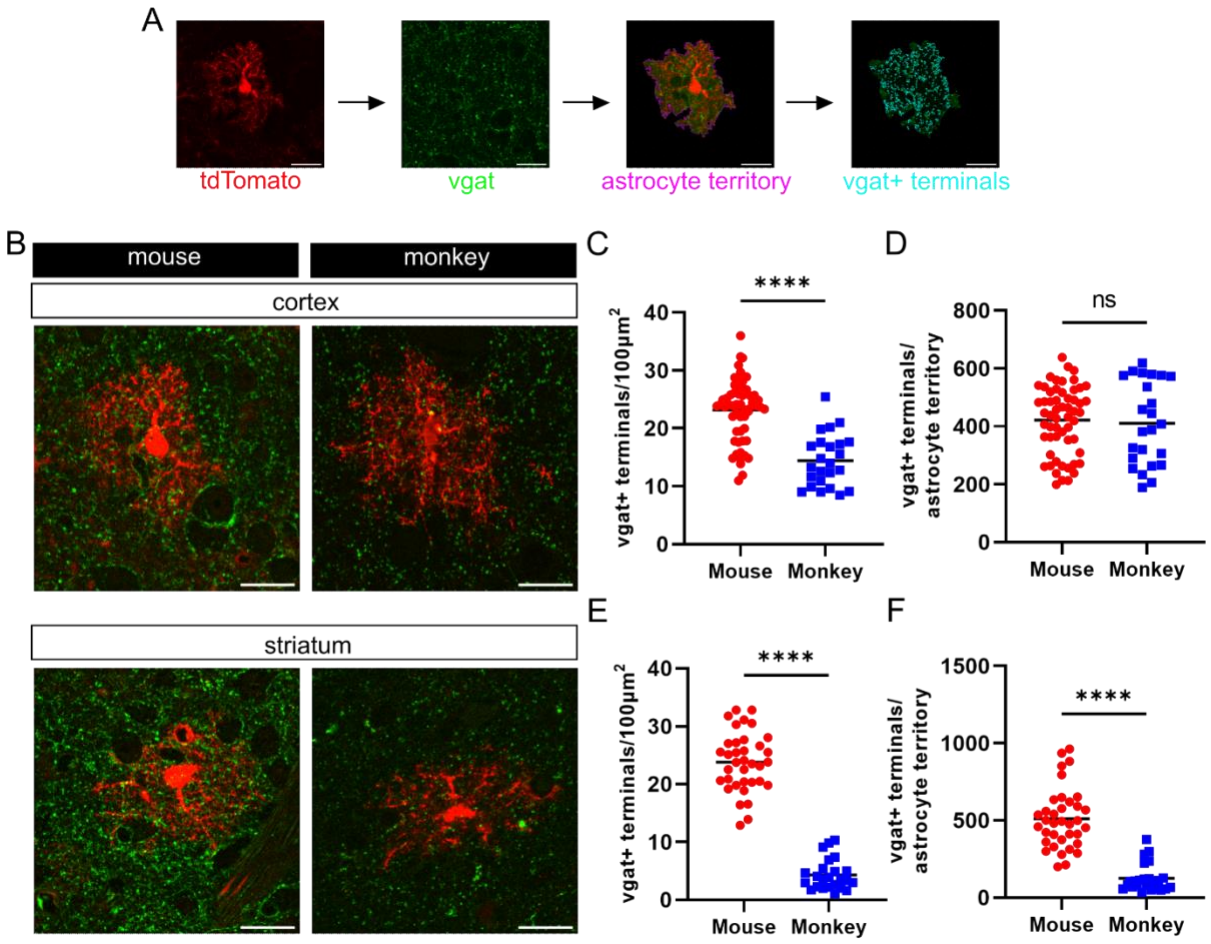

Figure 2.6 Astrocyte coverage of neuronal GABAergic terminals.
(A) Representative examples of image processing from right to left: tdTomato+ astrocyte, vgat labeling, outlining of the astrocyte territory, and quantification of the vgat+ terminals within the astrocyte territory. (B) Representative images of astrocytes and vgat staining in mouse (left) and monkey (right) primary motor cortex (top) and striatum (bottom). (C) Density of vgat+ terminals per 100 µm^2 in layer 5 of mouse and monkey motor cortex (N_{mouse}=4, $N_{astrocytes}$=19, N_{images}=57; N_{monkey}=2, $N_{astrocytes}$=8, N_{images}=24; t-test, $p<0.0001$). (D) Number of vgat+ terminals per astrocyte territory in primary motor cortex (t-test, $p=0.712$). (E) Density of vgat+ terminals per 100 µm^2 in striatum of mouse and monkey (N_{mouse}=4, $N_{astrocytes}$=12, N_{images}=36; N_{monkey}=2, $N_{astrocytes}$=8, N_{images}=24; t-test with Welch's correction, $p<0.0001$). (F) Number of vgat+ terminals per astrocyte territory in striatum (Mann-Whitney, $p<0.0001$). All scalebars 20 µm.

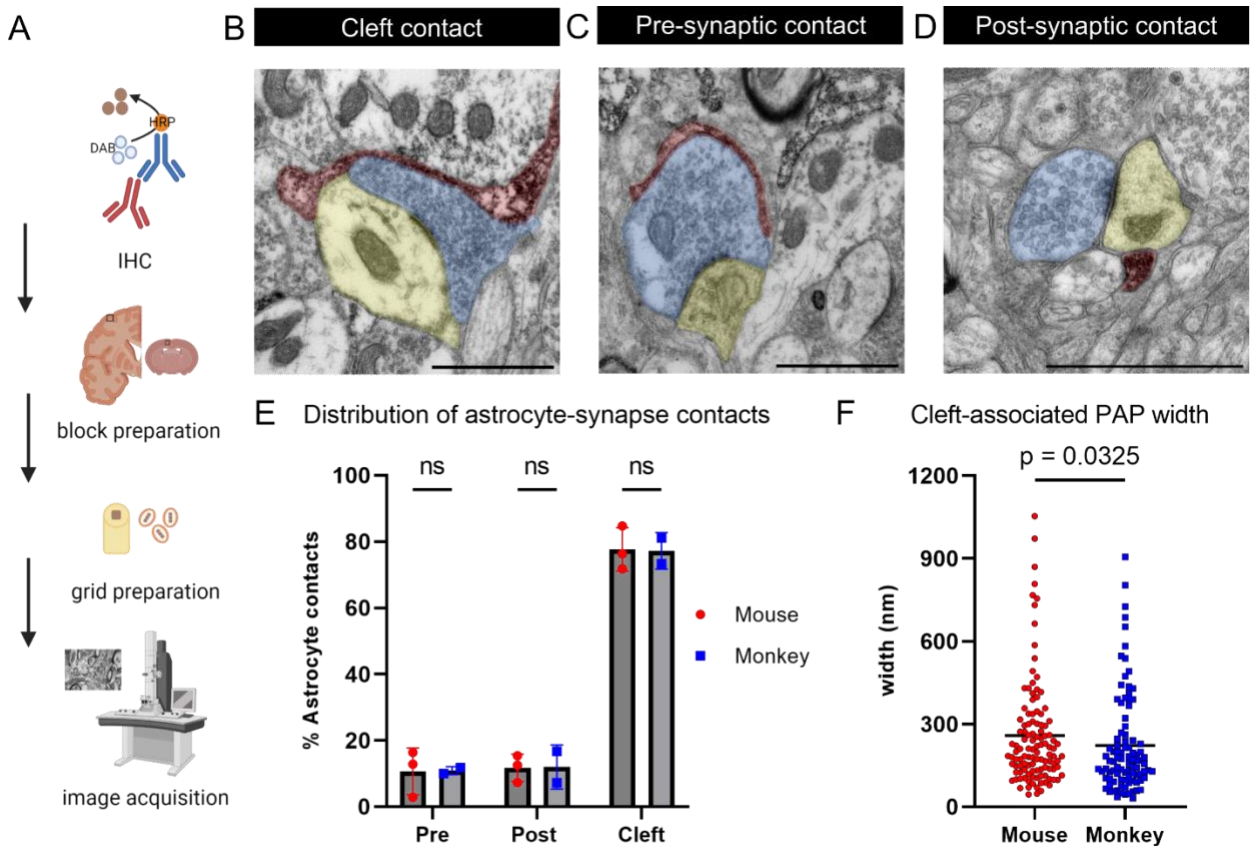

Figure 2.7 Spatial relationship between astrocyte processes and neuronal synapses.
(A) Schematic of experimental procedure. (B-D) Representative examples of astrocyte-synapse interactions. Astrocyte (red), axon terminal (blue), dendrite or dendritic spine (yellow). Scalebars are 1µm. (E) Distribution of the astrocyte-synapse contacts in mouse and monkey motor cortex (N_{mouse}=3, $N_{synapses}$=166; N_{monkey}=2, $N_{synapses}$=141). (F) Cleft-associated astrocyte processes were measured parallel to the synapse (N_{mouse}=3, $N_{synapses}$=115; N_{monkey}=2, $N_{synapses}$= 94; Mann-Whitney, p=0.0325).

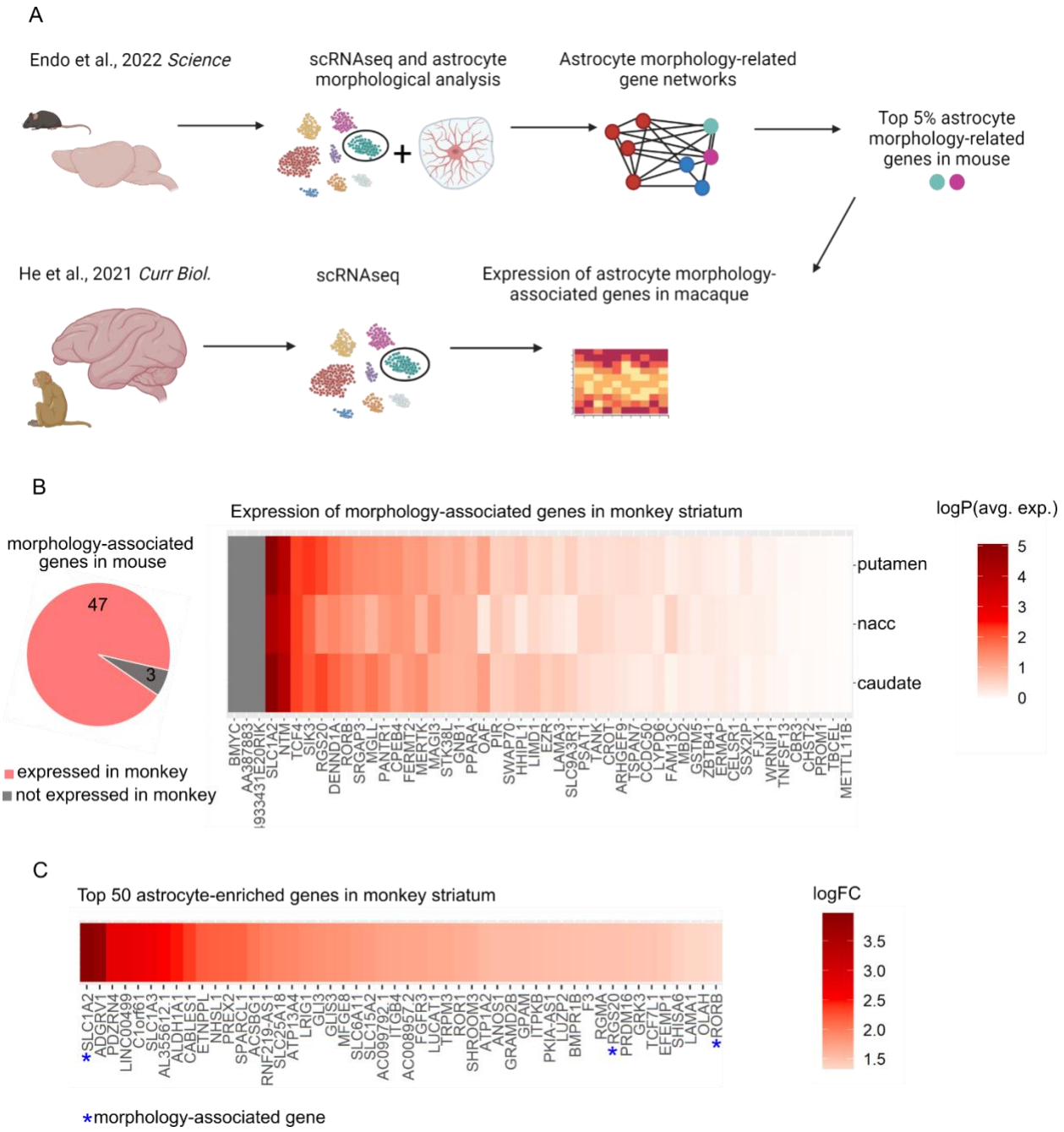

Figure 2.8 Expression of mouse astrocyte morphology-associated genes in primate astrocytes.

(A) Schematic of analysis. List of 50 morphology-associated astrocyte genes taken from Endo et al., 2023. A scRNAseq dataset of rhesus macaque striatum from He et al., 2021 was then parsed for the mouse morphology-associated astrocyte genes. (B) Expression of morphology associated genes in the rhesus macaque striatum (top – putamen; middle – nucleus accumbens (nacc); bottom – caudate). (C) The top 50 astrocyte-enriched genes (relative to other cell clusters) in the rhesus macaque striatum (putamen, nacc, and caudate combined). Morphology-associated genes marked by asterisks.

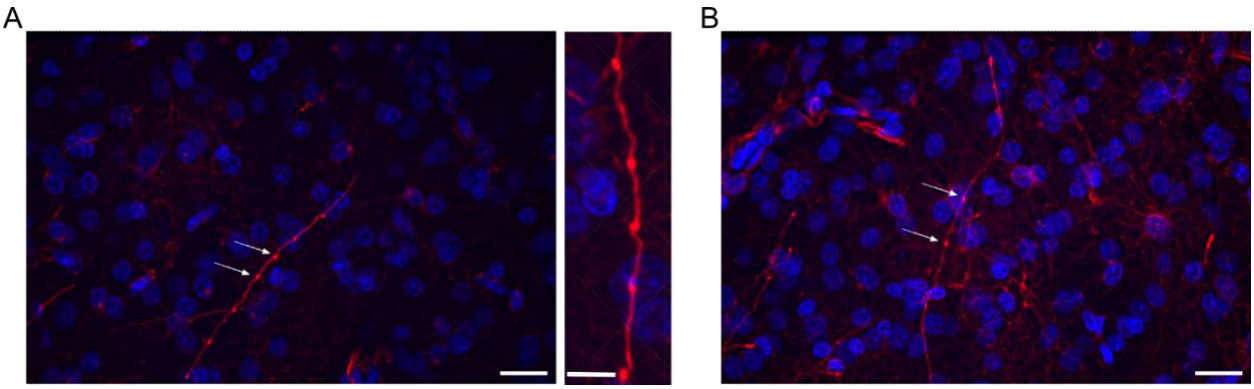

Supplementary Figure 2.1. Specialized features of primate astrocytes.
(A-B) Examples of GFAP+ varicosities found in rhesus macaque layer 5 of motor cortex. Scalebars 20 μm, inset 8 μm.

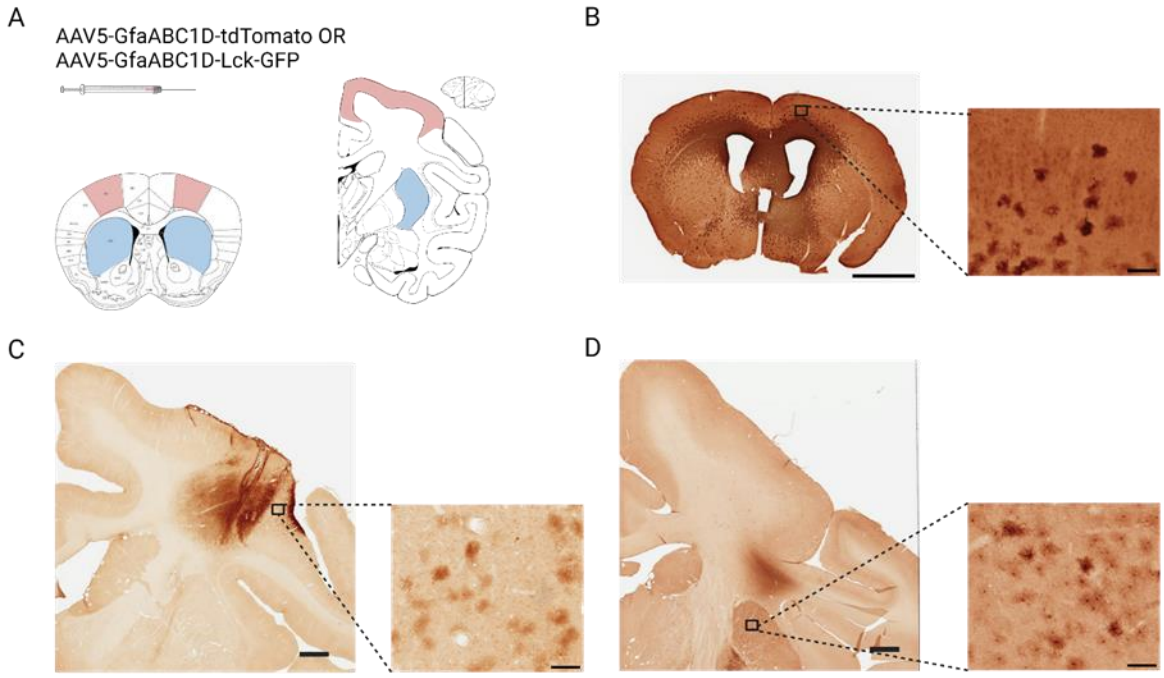

Supplementary Figure 2.2. Viral injection targets in mouse and monkey.
(A) Mice and monkeys received injections of AAV5-GfaABC1D-tdTomato or AAV5-GfaABC1D-Lck-GFP in motor cortex (red) and striatum (blue). (B) Representative example of transduction in mouse. (C) Example of transduction of astrocytes following injection with Lck-GFP in monkey. (D) Example of transduction of astrocytes following injection with tdTomato tag in monkey. Scale bars 2mm on whole sections, 100 μm on insets.

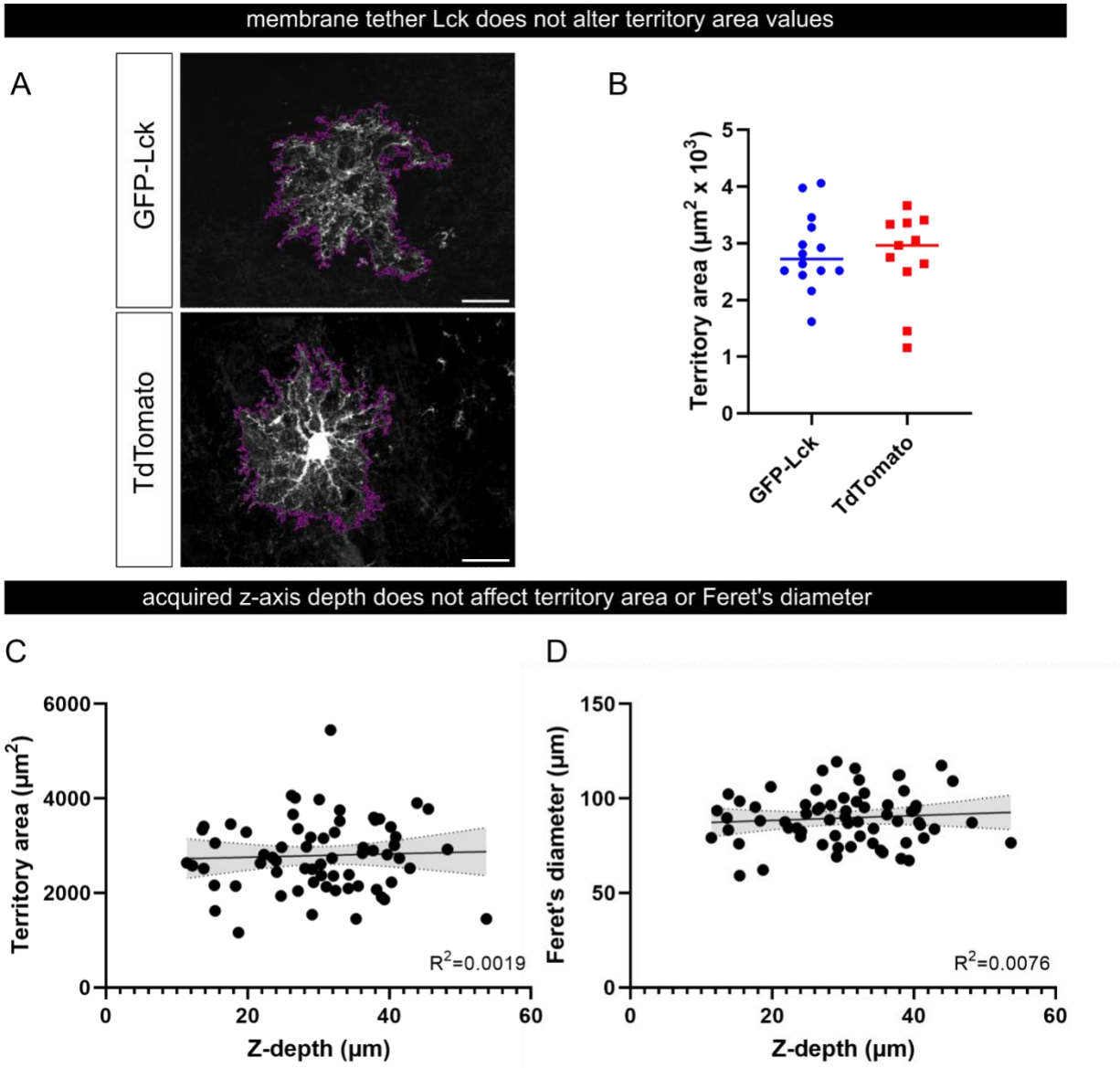

Supplementary Figure 2.3. Validation of GfaABC1D territory analysis method.
(A) Representative examples of astrocytes in layer 5 of motor cortex in monkey labeled by GFP-Lck (top) or tdTomato (bottom). Scalebars 20 µm. (B) Territory areas are comparable between GFP-Lck and TdTomato astrocytes (p = 0.7468, t-test). (C) The acquired depth in the z plane for a given astrocyte does not impact territory area measurements (Linear regression, R^2=0.0019, p=0.728). Data includes all cortical and striatal astrocytes from monkey (N_{cells}=66). (D) The acquired depth in z for a given astrocyte does not influence Feret's diameter measurements (Linear regression, R^2=0.0076, p=0.4861). Data includes all cortical and striatal astrocytes from monkey (N_{cells}=66).

CHAPTER 3: Exploring differences in astrocyte morphology and protein expression between normal and parkinsonian non-human primates

3.1 ABSTRACT

Astrocytes contribute to synaptic functions and ultimately behavior. The complex morphology of astrocytes allows for direct communication with neuronal synapses, blood vessels, and other glial cells. It was long believed that astrocytes were a homogenous population, but more recent studies have demonstrated that they display region specific functional and morphological properties. They are additionally involved in the formation, maintenance, and elimination of synapses, playing an important role in plasticity. The plastic nature of astrocyte morphology and function is seen across neurodegenerative disorders, and assessment of morphological changes may provide insight to functional changes in disease. To assess possible astrocyte dysfunction in parkinsonism, we investigated overall changes to astrocyte territory size in brain regions involved in motor function in control and 1-methyl-4-phenyl-1,2,3,6-tetrahydropyridine (MPTP) treated monkeys. In both the striatum and primary motor cortex, astrocyte territories were reduced in MPTP-treated monkeys. To assess if changes in astrocyte territory size were the result of astrocyte reactivity, we next investigated the expression of glial fibrillary acidic protein (GFAP), a known marker of astrocyte reactivity, across brain regions involved in motor function. Contrary to previous studies, we did not find increased immunoreactivity for GFAP in any brain region. Lastly, we assessed connexin-43 (cx-43) expression and localization in the external globus pallidus (GPe), an astrocyte-enriched and movement-associated brain region in which astrocyte dysfunction has been linked to parkinsonism in rodent models. Expression of cx-43 was unchanged between control and MPTP-treated monkeys, though there was an increase of cx-43 in astrocytic endfeet following dopamine depletion. Our data indicates that the use of GFAP to identify changes in dopamine depleted animals may not be conclusive, and that other astrocytic proteins (such as cx-43) may play a role in the pathological state.

3.2 INTRODUCTION

Astrocytes conform to the basic biological principle that form follows function. Astrocyte morphology adapts to changes in environment, which can reflect a disease process or contribute to the disease itself. Several notable changes in astrocyte morphology have been described in disease states such as changes in territory size, coverage of neuronal synapses, and a shift towards a reactive phenotype. Astrocyte reactivity likely falls on a spectrum, without clear phenotypic distinction between healthy and deleterious (Escartin et al., 2021). Increased glial fibrillary acidic protein (GFAP) immunoreactivity has been a common morphological and molecular (when assessed by 'omics') marker of astrocyte reactivity in neurodegenerative conditions (Eng et al., 1971). Other common astrocyte genes such as GJA1 (which codes for cx-43, the main gap junction-forming connexin expressed in astrocytes) have also been noted to increase in neurodegenerative diseases and influence astrocyte morphology (Baldwin et al., 2021; Ezan et al., 2012; Lagos-Cabré et al., 2017). While astrocyte reactivity cannot be determined by morphology alone, morphological analyses can provide insights into the molecular underpinnings of neurodegenerative states.

Specifically, within Parkinson's disease (PD) patients and animal models of parkinsonism, several notable changes in astrocyte morphology have been described. Dopamine depleted animal models (MPTP-treated rhesus macaques and 6-OHDA-treated rats) show increased GFAP expression in basal ganglia structures (Charron et al., 2014). Ultrastructurally, striatal astrocytes in MPTP-treated monkeys also show increased spatial coverage of glutamatergic synapses compared to controls (Villalba and Smith, 2011). However, the previous studies did not assess fine morphological changes or alterations in other neurodegenerative disease-associated astrocyte markers. Notably, few studies have addressed morphological

changes of astrocytes in parkinsonism, and none have examined morphology of astrocytes in motor cortical regions that are tightly connected to the basal ganglia.

Previous studies in rodents have identified astrocyte enrichment in the external segment of the globus pallidus GPe (Charron et al., 2014; Cui et al., 2016; Salvesen et al., 2015), a structure that forms part of the 'indirect' pathway of the basal ganglia and that has an important role in the pathophysiology of parkinsonism (Hegeman et al., 2016; Miller and DeLong, 1987; Soares et al., 2004). We additionally found higher densities of astrocytes in both mouse and monkey GPe compared to other structures, as discussed in Chapter 2 (see Figure 2.1). Astrocyte-to-neuron ratios are higher in the GPe compared to other structures, and this value is higher in the monkey GPe than in the mouse (Figure 2.1). The high density of astrocytes in the GPe may suggest a critical functional role, and perhaps augmented role in primate species. Ultrastructural studies have shown that GPe astrocytic processes wrap axonal terminals and are thus in the position to regulate synaptic transmission (Galvan et al., 2010). While GPe astrocytes likely play significant roles in supporting neuronal activity which is reflected by their morphological attributes, it is unclear whether they display altered morphology following dopamine depletion.

Given the literature regarding astrocyte dysfunction of GPe astrocytes in rodent models of parkinsonism (Chazalon et al., 2018; Cui et al., 2016), we investigated the morphological changes in astrocytes in the GPe and associated structures in the MPTP-treated monkey model of parkinsonism. Using GFAP and cx-43 immunostaining, and viral mediated transduction and visualization of astrocytes, we assess changes in astrocyte territory size and the expression and localization of reactivity-associated astrocyte markers.

3.3 MATERIALS AND METHODS

3.3.1 Animals

All procedures were approved by the Animal Care and Use Committee of Emory University and performed in accordance with the Guide for the Care and Use of Laboratory Animals (NRC, 2010) and the U.S. Public Health Service Policy on the Humane Care and Use of Laboratory Animals (revised 2015). All rhesus macaques were sourced from the Emory National Primate Research Center (ENPRC). The monkeys were maintained in a controlled environment with a 12-hour light/dark cycle, had free access to water, and were fed twice daily.

Three monkeys received weekly injections of 1-methyl-4-phenyl-1,2,3,6-tetrahydropyridine (MPTP; 0.2-0.8 mg/kg/week; Sigma, St. Louis, MO; total cumulative doses ranged from 4.1 to 18.4 mg/kg, total treatment time ranged from 1 to 10 months). Behavior was assessed weekly during MPTP treatment by a parkinsonism rating scale that includes bradykinesia, arm and leg akinesia, limb and trunk posture, action tremor, finger dexterity, cage activity, balance, and freezing; each item was scored 0-3 (absent to severe, 27 maximal score)(Devergnas et al., 2014b; Soares et al., 2004). Animals were treated with MPTP until they demonstrated moderate parkinsonism (defined as score of 11-15 in the rating scale and reduction in movement activity to ≤60% from baseline levels). Parkinsonism was considered stable if these measurements remain consistent for ≥4 weeks after the last MPTP injection.

Table 3.1. Animals

Sex	Species	Code	Age at perfusion	Group	Experiment(s)
F	Rhesus macaque	MR359	7 years 8 months	Control	Cx-43 IF, Cx-43 EM
F	Rhesus macaque	MR317	9 years 9 months	Control	GFAP, Cx-43 IF, Cx-43 EM
F	Rhesus macaque	MR357	4 years 8 months	Control	Cx-43 IF, Cx-43 EM
F	Rhesus macaque	MR324	16 years 6 months	Control	GFAP
F	Rhesus macaque	MR350	8 years 10 months	MPTP	GFAP
M	Rhesus macaque	MR271	2 years 9 months	Control	GFAP
M	Rhesus macaque	MR272	3 years 3 months	Control	GFAP
M	Rhesus macaque	MR269	5 years 1 month	MPTP	GFAP
M	Rhesus macaque	MR268	18 years 3 months	Control	GFAP
F	Rhesus macaque	MR245	13 years 7 months	MPTP	GFAP
F	Rhesus macaque	MR354	8 years 6 months	MPTP	TH, Cx-43 IF, Cx-43 EM

M	Rhesus macaque	MR273	6 years 3 months	MPTP	TH, GFAP, Cx-43 IF, Cx-43 EM
M	Rhesus macaque	MR362	6 years 10 months	MPTP	TH, Cx-43 IF, Cx-43 EM
F	Rhesus macaque	MR369	10 years 3 months	MPTP	AAV-GfaABC1D
M	Rhesus macaque	MR382	4 years 10 months	MPTP	AAV-GfaABC1D
M	Rhesus macaque	MR341	4 years 4 months	Control	AAV-GfaABC1D
M	Rhesus macaque	MR368	5 years 4 months	Control	AAV-GfaABC1D
F	Rhesus macaque	MR348	3 years 9 months	Control	AAV-GfaABC1D
M	Rhesus macaque	MR315	5 years 8 months	Control	TH
M	Rhesus macaque	MR316	5 years 8 months	Control	TH
M	Rhesus macaque	MR322	4 years 2 months	Control	TH
Experiment details: GFAP – GFAP immunofluorescence; Cx-43 IF – cx-43 immunofluorescence; Cx-43 EM – cx-43 immunoperoxidase for electron microscopy; AAV-GfaABC1D – viral injections					

3.3.2 AAV injections in monkeys

The procedure for viral injections in monkeys is described in detail in Chapter 2 (section 2.3.3).

3.3.3 Perfusion and tissue preparation

Monkeys were transcardially perfused with Ringer's solution followed by a fixative solution containing 4% PFA and 0.1% glutaraldehyde. Brains were post-fixed in 4% PFA for 24-48 hours at 4°C and then sectioned coronally at 60 µm on a vibratome (Leica). Sections from MR369 were cut on a freezing microtome at 50 µm. Sections were stored in an anti-freeze solution at -20°C until further processing. Prior to staining, all sections were first treated with 1% sodium borohydride, to reduce free aldehydes and Schiff bases resulting from glutaraldehyde fixation and rinsed in phosphate buffered saline (PBS; 0.01M, pH 7.4).

3.3.4 Tyrosine hydroxylase (TH) immunoperoxidase

Three sections per animal corresponding to approximate levels 12.45, 15.15, and 20.1 from the interaural line were selected for analysis (Paxinos et al., 2000). Sections were incubated in a solution of 1% normal serum, 1% BSA, and 0.3% Triton X-100 in PBS. Sections were then incubated overnight in the blocking/permeabilization solution containing antibodies for TH (see Table 3.2). Binding sites were revealed using a biotinylated secondary antibody (Table 3.2). Sections were incubated in the secondary solution for 90 minutes and rinsed in PBS. Sections

were then incubated in an ABC solution (1:200, Vector Laboratories) containing 1% BSA and 0.3% Triton X-100 for 90 minutes. Followed by rinses in PBS and TRIS buffering solution (0.05M, pH 7.6), sections were incubated in TRIS buffer containing 0.025% 3,3'-diaminobenzidine tetrahydrochloride (DAB; Sigma), 10 mM imidazole, and 0.006% hydrogen peroxide for 10 minutes, immediately followed by PBS rinses. Following mounting, sections were dehydrated in a graded series of alcohol and toluene, then coverslipped. Slides were scanned with an Aperio Scanscope CS system (Leica).

Images of scanned slides were acquired at a zoom of 0.5x in Aperio's ImageScope software and exported to ImageJ. For each section, the caudate and putamen were divided into dorsolateral and ventromedial areas, by drawing a line approximately parallel to the lateral edge of the structure. The image was then inverted, and the integrated density was measured in each area. Data is represented as proportion of the average integrated density in control animals.

3.3.5 GfaABC1D territory size

The procedures for staining and analysis are described in detail in Chapter 2 (section 2.3.4.2). The astrocytes analyzed from control animals are the same as those shown in Chapter 2.

3.3.6 GFAP immunoperoxidase

Two sections per animal, at approximately 12-16 interaural according to the Paxinos atlas (Paxinos et al., 2000), were incubated in a solution of 1% normal serum, 1% BSA, and 0.3% Triton X-100 in PBS. Sections were then incubated overnight in the blocking/permeabilization solution containing a GFAP antibody (see Table 3.2). Binding sites were revealed using a biotinylated secondary antibody (Table 3.2). Sections were incubated in the secondary solution for 90 minutes and rinsed in PBS. Sections were then incubated in an ABC solution (1:200, Vector Laboratories) containing 1% BSA and 0.3% Triton X-100 for 90 minutes. Followed by rinses in PBS and TRIS buffering solution (0.05M, pH 7.6), sections were incubated in TRIS

buffer containing 0.025% 3,3'-diaminobenzidine tetrahydrochloride (DAB; Sigma), 10 mM imidazole, and 0.006% hydrogen peroxide for 10 minutes, immediately followed by PBS rinses. Following mounting, sections were dehydrated in a graded series of alcohol and toluene, then coverslipped. Slides were scanned at 20x with an Aperio Scanscope CS system (Leica).

Slide images were opened in Aperio ImageScope software (Leica). The regions of interest (GPe, putamen, and motor cortex) were identified. Per structure, 3 snapshot images at 10x zoom were randomly taken and imported into ImageJ. The images were then cropped to 700 µm by 700 µm, avoiding any areas with gross damage or large blood vessels. The cropped images were then converted to an 8-bit format, inverted, thresholded, and binarized using the "Huang" method. The number of pixels with a value of 0 (black pixels), representing staining, was recorded, and represented as a proportion of all pixels in the image. The pixel proportion from 3 cropped images per region per slide were averaged together.

3.3.7 Cx-43 immunofluorescence

To reduce autofluorescence in the tissue, one section per animal was subjected to "photobleaching" prior to incubations. The sections were placed in 6-well transparent plates containing PBS in a refrigerator (4°C) equipped with broad-spectrum white lights. The well-plates were placed on a rack directly above the lights and left with the lights on for 4 days. Sections were incubated in a solution of 1% donkey serum, 1% BSA, and 0.3% Triton X-100 in PBS. Sections were then incubated overnight in the blocking/permeabilization solution containing an antibody against cx-43 (see Table 3.2). Binding sites were revealed using a fluorophore-conjugated secondary antibody (Table 3.2). Sections were incubated in the secondary solution for one hour and rinsed in PBS. Sections were incubated in PBS containing DAPI (5µg/mL) for 10 minutes. Sections were then mounted with Vectashield (Vector Laboratories) on slides and coverslipped.

Sections were imaged using a Leica SP8 confocal microscope. Three Z-stacks of 1.5 µm were obtained in the GPe with a 63x (NA 1.4) objective, 512x512 scan format, 2.4x optical zoom, and 0.3 µm z-steps resulting in an x-y pixel size of 143.5 nm x 143.5 nm. Laser settings were kept identical across all images. Stacks of images were converted to maximum intensity z-projections in ImageJ. The channel containing the cx-43 staining underwent background subtraction with a rolling ball radius of 50 pixels and was thresholded using the "Moments" method in ImageJ. The number of puncta was then determined by using the "Analyze Particles" tool with a minimum particle size of 0.15 μm^2. The number of puncta per image were recorded.

3.3.8 Cx-43 immunoperoxidase for electron microscopy

For electron microscope analysis, sections were first treated with 1% sodium borohydride as above, before being placed in a cryoprotectant solution, frozen at −80°C to maximize antibody penetration and washed in serial dilutions of cryoprotectant in PBS. After blocking with 1% normal serum and 1% bovine serum albumin in PBS, the sections were incubated for two days at 4°C in the primary antibody. The avidin-biotin complex (ABC) method was used to amplify signal. The sections were incubated in biotinylated secondary antibodies for 2 hours, and in the ABC solution (1:100; Vectastain Standard kit, Vector) for 90 minutes. Sections were rinsed in PBS and TRIS buffer (0.05 M, pH 7.6) before being placed in DAB solution for 10 minutes. Next, sections were rinsed in PBS and kept at 4°C overnight.

The sections were then placed in PB for 10 min to desalt and postfixed in osmium tetroxide (1% in PB). They were washed in PB and dehydrated in a series of ethanol and propylene oxide. The 70% ethanol solution contained 1% uranyl acetate. The sections were embedded in resin overnight and placed on slides before being placed in the oven for 48 hours at 60°C. Blocks from primary motor cortex were cut from each animal and glued on top of resin blocks. After facing, serial ultrathin sections were cut on an ultramicrotome (Leica Ultracut T2,

Leica, Nussloch, Germany). Sixty nanometer thick sections from the surface of the block were collected on copper single slot grids and stained with lead citrate for 5 minutes.

Stained grids were examined on an electron microscope (EM Model 1011; Jeol, Peabody, MA, USA) coupled with a CCD camera (Gatan Model 785; Warrendale, PA, USA). Each section was scanned at 5,000x to identify immunoperoxidase labeling. Peroxidase-labeled elements were imaged at 40,000x. Using ImageJ, elements were identified according to ultrastructural features (Peters et al., 1991). Fields containing peroxidase-labeled astrocytes and interfaces were acquired and categorized based on their spatial relationship. Interfaces were defined as the junction between axonal terminals and post-synaptic elements (dendrite or dendritic spine). Interfaces in which the axonal terminal was contacted by a cx-43+ astrocyte process were considered "pre" contacts. Interfaces in which the dendrite or dendritic spine were touched by cx-43+ astrocytes were considered "post" contacts. If the cx-43+ astrocyte touched both the pre- and post-interface elements, it was considered a "cleft" contact. Images of all blood vessels in the block were also acquired. Blood vessels with cx-43 labeling on astrocyte processes touching the basal lamina were counted.

Table 3.2. Antibodies

Antibody	**Catalogue Number**	**Antibody Registry**	**Lot Number**	**Dilution**
mCherry rabbit	Abcam AB167453	AB_2571870	1024587	1:1000
GFP chicken	Millipore 06-896	AB_11214044	DAM1543699	1:2000
GFAP rabbit	Abcam AB7260	AB_305808	3132965	1:5000
Cx-43 mouse	Millipore MABT528	AB_2110187	3256998	1:2500
TH Chicken	Abcam AB76442	AB_1524535	GR3358971-1	1:1000
DAPI	Invitrogen D-1306	AB_2629482	2031179	5ug/ml
Donkey anti-mouse RRX	Jackson Lab 715-295-	AB_2340831	158805	1:100
Donkey anti-rabbit RRX	Jackson Lab 711-295-	AB_2340613	154859	1:100
Donkey anti-chicken FITC	Jackson Lab 703-095-	AB_2340356	152661	1:100
Biot. Goat anti-rabbit	BA1000 Vector	AB_2313606	NA	1:200
Biot. Horse anti-mouse	BA2000 Vector	AB_2313581	NA	1:200
Biot. Goat anti-chicken	BA9010 Vector	AB_2336114	NA	1:200

3.3.9 Statistical analysis and figures

Normality was first determined using the D'Agostino Pearson test. Two group comparisons (normal, MPTP) were made using unpaired Mann-Whitney tests or unpaired t-tests. Proportions of cx-43 synapse contacts were assessed by chi-square. The results of statistical analysis, n, and p-values are included in figure legends. N is defined as number of animals or sections depending on analysis and is described in the figure legend. Statistics were run using GraphPad Prism 9. Data are represented as mean ± SD. In all figure plots, p-values are represented by asterisk(s): ∗ for $p < 0.05$; ∗∗ for $p < 0.01$; ∗∗∗ for $p < 0.001$; ∗∗∗∗ for $p < 0.0001$. All schematics for figures were made using BioRender.com.

3.4 RESULTS

3.4.1 Dopamine denervation in MPTP-treated monkeys

To complement behavioral observations of motor impairments in MPTP-treated monkeys, we assessed the degree of dopamine denervation in post-mortem tissue using tyrosine hydroxylase immunostaining. Reductions in tyrosine hydroxylase were seen across the anterior-posterior extent of the caudate and putamen compared to normal animals (Figure 3.1B-C). The level of decreased TH staining in the striatum corresponds to the mild-to-moderate degree of parkinsonism displayed by the animals (Figure 3.1A).

3.4.2 Astrocyte morphological features across GPe, putamen, and motor cortex in monkeys

We examined the morphology of astrocytes in regions of the basal ganglia (GPe and putamen) and in the primary motor cortex in normal and MPTP treated monkeys, revealing astrocytes with fluorescent proteins expressed by viral transduction. Astrocytes in putamen and motor cortex layer 5 show remarkably similar morphologies and territory sizes, as shown in Chapter 2 and reiterated by the images in figure 3.2. Interestingly, astrocytes within the GPe in monkeys show reduced branching arborization compared to the putamen and motor cortex (Figure 3.2). The morphology of GPe astrocytes more closely resembles fibrous astrocytes rather

than protoplasmic astrocytes, with fewer branches and intermingled territories. We then compared morphological features of astrocytes between normal and parkinsonian animals. We found reduced territory size in both putamen ($p=0.0281$, Mann-Whitney) and motor cortex ($p=0.018$, t-test) in MPTP-treated monkeys compared to healthy controls. Interestingly, we only found reduced Feret's diameter in putamen ($p=0.0292$, t-test) following MPTP, but the diameter in motor cortex was unchanged between groups ($p=0.5019$, t-test). Although the viral vector-labeling technique helped to identify astrocytes in GPe to assess their general morphology, it did not allow for studies of astrocyte territory size in the GPe. The cells do not follow the typical tiling pattern of protoplasmic astrocytes, resulting in overlapped territories between neighboring cells (as shown in the low magnification images in Figure 3.2B), a feature that prevented reliable characterization of individual astrocytes.

3.4.3 GFAP immunoreactivity in parkinsonism

To assess astrocyte reactivity following dopamine depletion, we utilized GFAP immunostaining in the GPe, striatum, and motor cortex. In healthy animals, GFAP expression is relatively higher in the GPe compared to the striatum (Chai et al., 2017; Cui et al., 2016). Additionally, previous studies showed increased GFAP expression in both the GPe and striatum in parkinsonian animals (Charron et al., 2014). To our knowledge, assessment of GFAP expression in the motor cortex in parkinsonian animals has not been previously reported. Due to the overlapping nature of astrocytes in the GPe (Figure 3.1), we could not identify individual astrocytes to assess GFAP expression and branching structure. As a representative measure, we calculated overall tissue densities of GFAP. The percent pixels occupied by GFAP+ astrocyte staining was not significantly different between control and MPTP-treated animals in either the GPe ($p=0.4$, Mann-Whitney, Figure 3.3C), striatum ($p>0.999$, Mann-Whitney, Figure 3.3D) or primary motor cortex ($p>0.9999$, Mann-Whitney, Figure 3.3E).

3.4.4 Cx-43 immunoreactivity in the GPe in parkinsonian animals

Astrocytes in the primate GPe display different morphological features, such as overlapping territories as described. Additionally, astrocytes within the GPe have displayed altered functions in dopamine depleted animals (Chazalon et al., 2018; Cui et al., 2016), as well as increased expression of cx-43 (Kawasaki et al., 2009). As cx-43 is highly expressed in the GPe versus striatum (Charron et al., 2014), and cx-30 is the predominant connexin expressed in cortex (Nagy et al., 1999), we next assessed expression of cx-43 in the GPe of control and MPTP-treated monkeys using immunofluorescence. Immunoreactive levels of cx-43 were unchanged following treatment with MPTP ($p=0.3401$, Mann-Whitney, Figure 3.4B). Additionally, the size of cx-43 puncta was similar between conditions ($p=0.6048$, Mann-Whitney, Figure 3.4C).

3.4.5 Cx-43 ultrastructural localization in GPe in parkinsonian animals

Though we did not find differences in the expression levels of cx-43 between control and parkinsonian monkeys in the GPe with confocal microscopy, we used electron microscopy to assess whether the ultrastructural localization of cx-43 could be affected following dopamine depletion. Since cx-43 may be involved in the release of neuroactive species and is additionally localized within astrocytic endfeet that contact blood vessels (Chever et al., 2014; Cibelli et al., 2021; Stehberg et al., 2012), we focused on the expression of cx-43 on astrocyte processes in contact with neuronal synapses or vasculature. We found that cx-43+ astrocytic endfeet were more frequently found in MPTP-treated animals than in controls ($p=0.0857$, Mann-Whitney, Figure 3.5B-C). In relation to neuronal elements, the majority of cx-43+ astrocyte processes contacted pre-synaptic elements (axonal terminals) only, while smaller proportions contacted either the post-synaptic element (dendrites or spines) or established a contact that spanned the pre- and post-synaptic elements (the synaptic cleft (Figure 3.3D)). The proportion of the type of

synaptic element contacted by cx-43+ astrocyte processes were similar between control and MPTP-treated monkeys (p=0.2312, chi-square, Figure 3.5F). The number of pre- and post-synaptic element interfaces were not significantly different between control and MPTP-treated monkeys (p=0.8571, Mann-Whitney, Figure 3.5E), and thus did not affect the distribution of cx-43+ astrocyte contacts.

3.5 DISCUSSION

Our results demonstrate altered astrocyte morphology in movement-related brain areas following dopamine depletion. All animals in the study treated with MPTP showed reduction of tyrosine hydroxylase immunoreactivity consistent with mild-to-moderate parkinsonism (Galvan et al., 2014). Astrocytes territories in both primary motor cortex and striatum were reduced in MPTP-treated monkeys compared to controls. Despite a reduction in territory size, the Feret's diameter in motor cortex was unchanged, suggesting an elongation of the astrocytes and change from a more spherical shape to ovoid. Reduction of astrocyte territory size has not been assessed or described in brain sections from human PD patients of mouse models of parkinsonism. However, *in vitro* assessments of astrocytes generated from induced pluripotent stem cells of PD patients have described decreases in astrocyte size and complexity (Ramos-Gonzalez et al., 2021). The mechanisms underlying reduced territory size remain unknown but could be due to direct toxic effects of MPTP or secondary effects, such as a loss of axonal terminals in the investigated brain regions. MPTP is converted to MPDP in astrocytes, which is then released and converted into its active and toxic form, MPP+, in the extracellular space (Schildknecht et al., 2017). The toxicity of MPTP is likely lower (though not benign) in astrocytes compared to dopaminergic neurons, which express high levels of dopamine transporters which have a high affinity for MPP+ (Ransom et al., 1987; Schildknecht et al., 2015). Thus, it is possible that reduced astrocyte territory sizes are the result of MPTP toxicity.

We were unable to quantitatively assess changes in astrocyte territory between control and MPTP-treated monkeys in the GPe. Interestingly, astrocytes in the primate GPe do not display a typical protoplasmic astrocyte morphology. GPe astrocytes have long processes with little branching, often traversing neighboring astrocyte territories. This morphology is more typical of white matter fibrous astrocytes (Andriezen, 1893). The visual lack of complexity in GPe astrocytes could be due to low neuronal density (as described in Chapter 2) in the structure. GPe astrocyte morphology also appears different from other brain structures using electron microscopy. Rather than assuming the canonical tripartite synapse spatial relationship with neuronal synapses, in which as astrocyte process makes contact with a synaptic cleft (Araque et al., 1999; Villalba and Smith, 2011), GPe astrocytes instead wrap themselves around the entire synaptic complex as previously described (Galvan et al., 2005). This unique spatial relationship should be investigated in future 3D electron microscopy studies, as it remains unclear if this relationship is unique to primates and if it changes in disease states.

In contrast with previous studies showing increased GFAP (Charron et al., 2014; Henning et al., 2008) and cx-43 expression (Kawasaki et al., 2009) following dopamine depletion, we did not find any differences between control and MPTP-treated animals. Across three structures (primary motor cortex, putamen, and GPe), GFAP levels were not significantly different between groups. This suggests that the astrocytes do not display a reactive phenotype, which is consistent with postmortem samples from the aforementioned brain regions in Parkinson's patients (Charron et al., 2014). While we did not find increased GFAP in primary motor cortex, putamen, or GPe, it is possible that there are changes in other brain regions more directly affected by MPTP toxicity (or the pathological process in PD), such as the substantia nigra. Postmortem assessment of brain tissue from patients with PD revealed that GFAP levels inversely correlated

with pathological burden in the substantia nigra (Tong et al., 2015). Therefore, in animal studies in which there is a marked increase in GFAP expression (Charron et al., 2014; Henning et al., 2008), astrocyte reactivity is likely the result of the method of dopamine depletion.

Similarly, cx-43 expression levels and size of puncta at the light microscopy were unchanged in the GPe MPTP-treated monkeys. The size of cx-43 positive puncta was approximately the same across groups, suggesting a comparable ratio of hemichannels to gap junctions. In rodent models of parkinsonism, cx-43 levels were increased in the GPe and striatum (Kawasaki et al., 2009; Rufer et al., 1996; Wang et al., 2013). However, expression of cx-43 was assessed shortly after neurotoxin administration, increasing the likelihood that changes of cx-43 were a temporary response to the toxin rather than a PD-relevant mechanism. Our animals stopped receiving MPTP many weeks to months prior to perfusion, and thus we would not capture the potential transient increase in cx-43 possibly seen in other studies.

Although expression levels of cx-43 did not change following MPTP administration, we assessed the ultrastructural localization of cx-43 in the GPe. In MPTP-treated monkeys, we found increased cx-43 expression in astrocyte endfeet, though this change was not significantly different from controls. This increase in localization to endfeet has also been described in the GPe dopamine depleted rats (Charron et al., 2014). The function of cx-43 in astrocytic endfeet is unknown, though its expression is tightly related to the expression of aquaporin-4, suggesting a role in water exchange with the vasculature (Boulay et al., 2018; Cibelli et al., 2021). Further, astrocytes appear edematous following deletion of cx-43 and blood brain barrier integrity is reduced (Ezan et al., 2012). Thus, the increase in blood vessel-associated cx-43 expression may be a compensatory mechanism to maintain blood brain barrier integrity. Though controversial, blood brain barrier integrity is reportedly decreased across neurodegenerative diseases, but the

mechanisms underlying this change are unknown (Knox et al., 2022). If the blood brain barrier is in fact disrupted, increased cx-43 expression in endfeet should occur in other brain regions as well.

We also assessed the localization of astrocyte cx-43 in relation to neuronal synapses. Approximately 75% of all dendrite-terminal interfaces were not contacted by a cx-43+ astrocyte process, suggesting that cx-43 does not play a significant and direct role in the modulation of synaptic activity in the GPe. In MPTP-treated monkeys, the distribution of cx-43+ astrocyte contacts with synapses remained the same as control monkeys. For synapses in contact with cx-43+ processes in both control and MPTP-treated monkeys, the majority of contacts were made with pre-synaptic axonal terminals. Unpaired cx-43 hemichannels may therefore play a modulatory role of presynaptic neurotransmitter release. Such a mechanism has been described in the hippocampus, in which cx-43 hemichannels altered neuronal excitability via the release of ATP (Chever et al., 2014; Torres et al., 2012). Altogether, our data suggests that astrocytes following dopamine depletion to not show cardinal morphological changes associated with reactivity but do display smaller territory areas and altered localization of cx-43, which may contribute to the pathophysiology of parkinsonism, and should be assessed in future studies.

3.6 LIMITATIONS

In this study we used immunoperoxidase labeling of cx-43 rather than immunogold which would have allowed for better spatial resolution and possible quantification of cx-43 hemichannels versus gap junctions (Galvan et al., 2006). Additionally, were unable to reliably quantify symmetric and asymmetric synapses, thus it is possible that cx-43+ astrocyte processes preferentially contact one synapse type versus another, and that this relationship is changed following dopamine depletion.

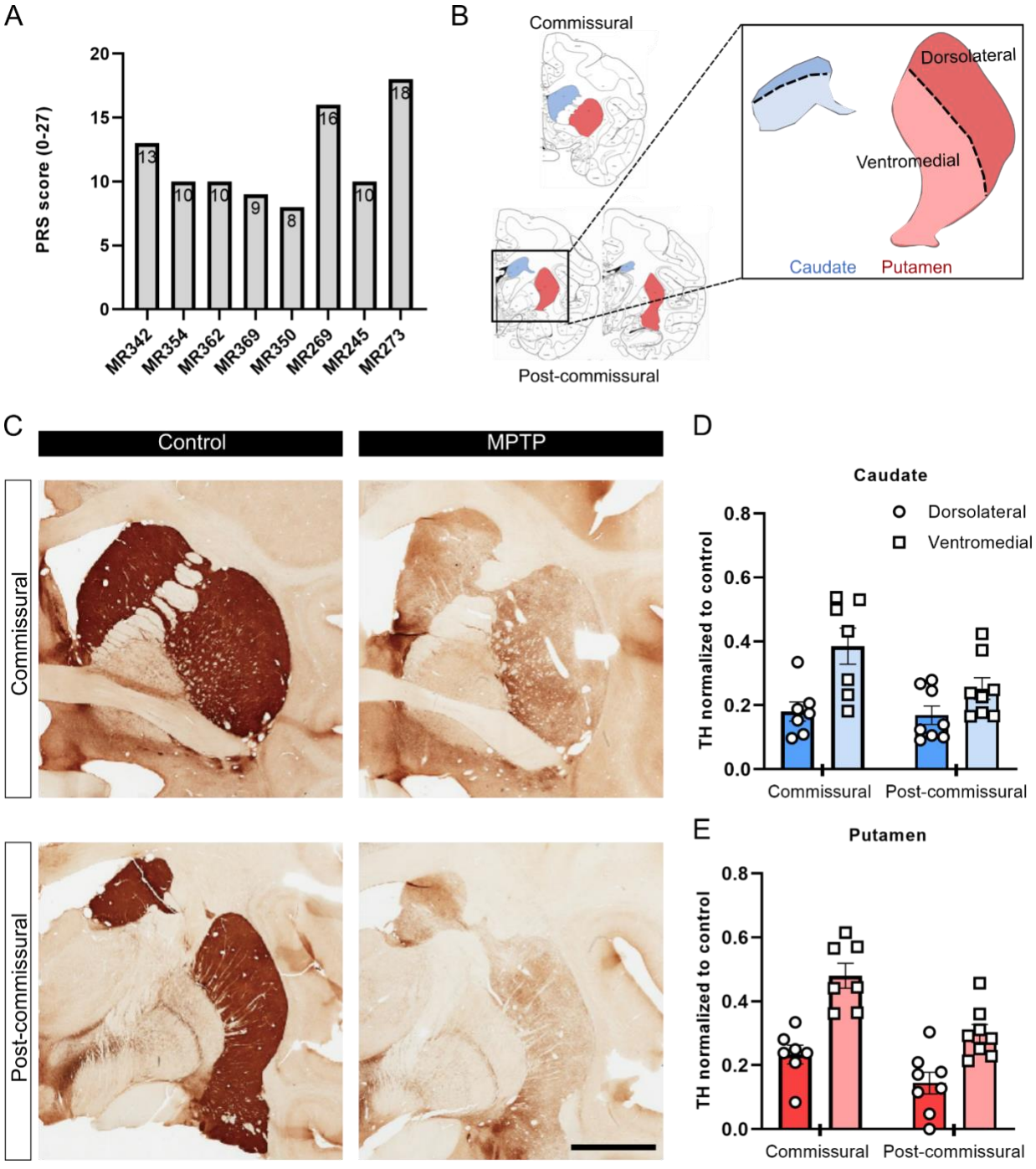

Figure 3.1 Tyrosine hydroxylase in control and MPTP-treated animals.
(A) PRS scores of MPTP-treated animals once they displayed stable parkinsonism. (B) Schematic of staining and regions for analysis. (C) Representative examples of TH staining in pre- and post-commissural sections in control and MPTP-treated animals. Scalebar 5mm. (D) Integrated densities of TH staining in the caudate relative to control animals. (E) Integrated densities of TH staining in the putamen relative to control animals (Control, N=3; MPTP, N=8).

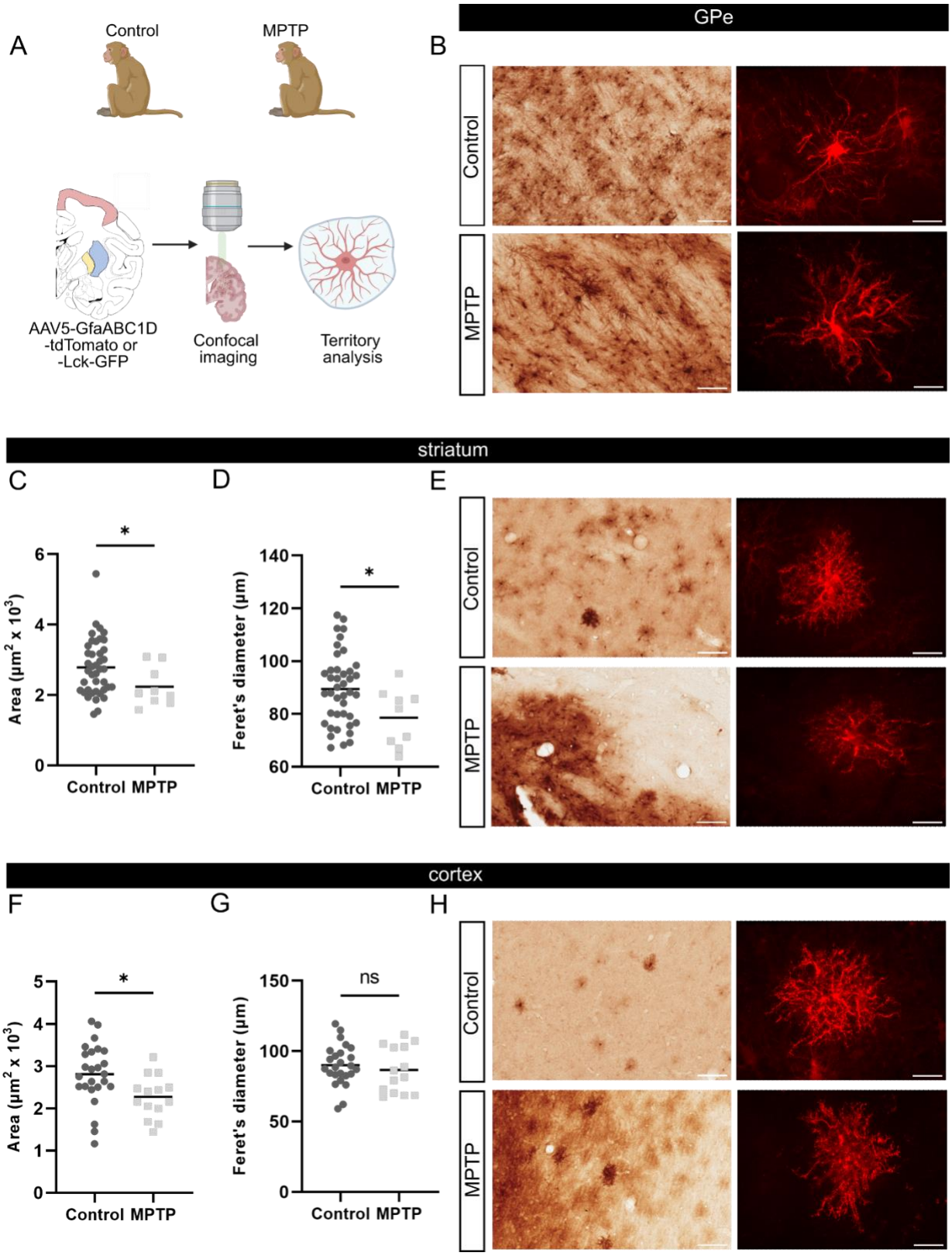
A
Control
MPTP
AAV5-GfaABC1D
-tdTomato or
-Lck-GFP
Confocal
imaging
Territory
analysis
B
GPe
Control
MPTP
striatum
C
Area (µm² x 10³)
Control MPTP
D
Feret's diameter (µm)
Control MPTP
E
Control
MPTP
cortex
F
Area (µm² x 10³)
Control MPTP
G
Feret's diameter (µm)
ns
Control MPTP
H
Control
MPTP

Figure 3.2 Astrocyte territories in the GPe, striatum, and motor cortex of control and MPTP-treated monkeys.

(A) Schematic of experimental procedures (motor cortex, striatum (putamen), and GPe shown in pink, blue, and yellow respectively). (B) Examples of astrocytes in the GPe of control (top) and MPTP (bottom) monkeys. (C) Territory area of astrocytes in striatum in control and MPTP monkeys ($N_{control}$= 2, N_{cells}= 41, N_{MPTP}= 2, N_{cells}= 9; p=0.0281, Mann-Whitney). (D) Feret's diameter of astrocytes in striatum (p=0.0292, t-test). (E) Examples of astrocytes in the striatum. (F) Territory area of astrocytes in primary motor cortex in control and MPTP monkeys ($N_{control}$= 2, N_{cells}= 25, N_{MPTP}= 3, N_{cells}= 14; p=0.018, t-test). (G) Feret's diameter of astrocytes in primary motor cortex (p=0.5019, t-test). (H) Examples of astrocytes in primary motor cortex. Scalebars in peroxidase images are 100 µm, scalebars on fluorescent images are 20 µm.

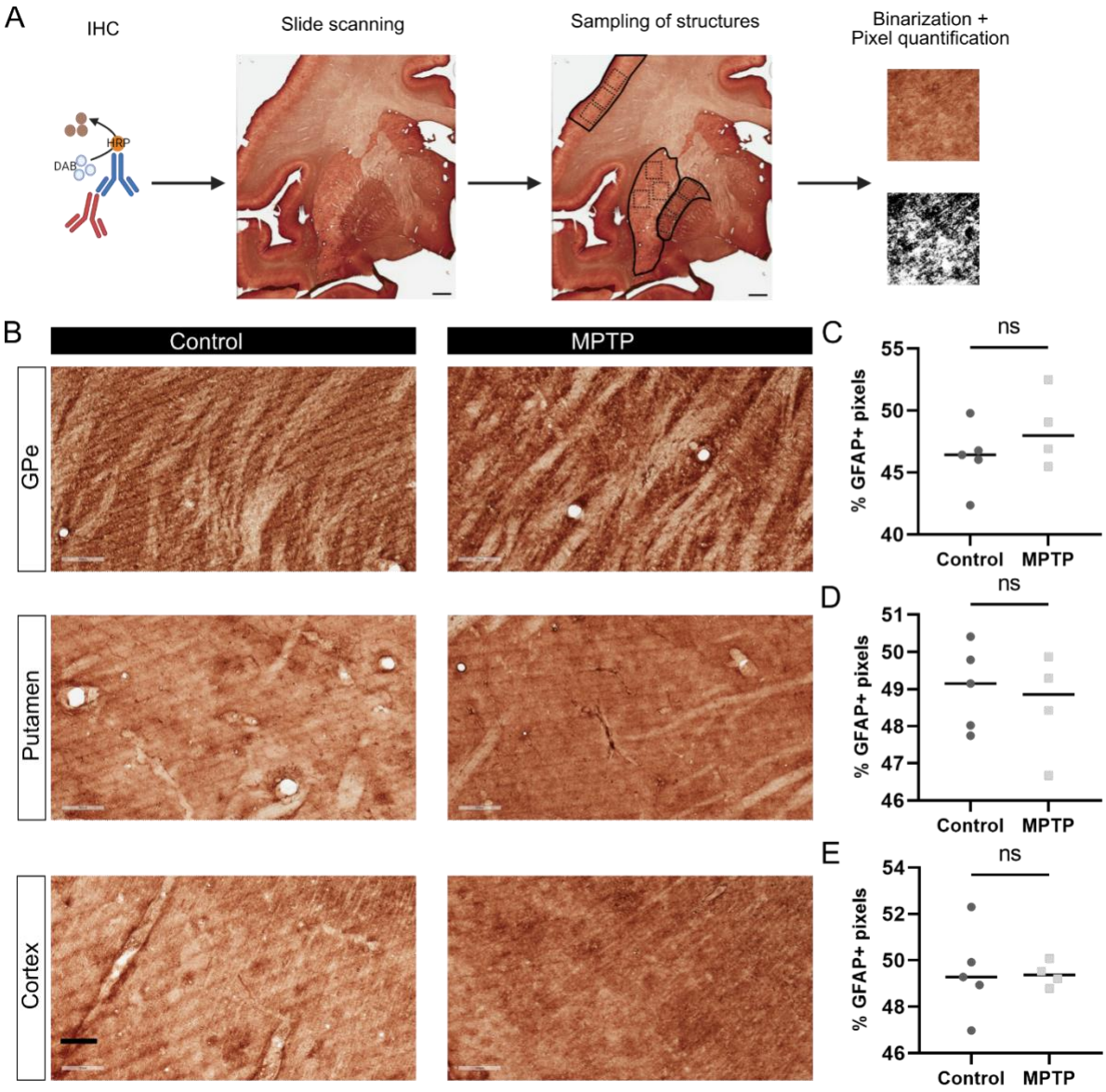

Figure 3.3 GFAP immunoreactivity in the GPe, putamen, and motor cortex of control and MPTP-treated monkeys.

(A) Schematic of staining and analysis. Scalebars 2 mm. (B) Representative images showing GFAP immunoreactivity in the GPe, putamen, and motor cortex in control and MPTP-treated monkeys. Scalebars 200 µm. (C) Percent of pixels covered by GFAP staining in control and MPTP-treated monkeys in the GPe (p=0.4127, Mann-Whitney). (D) Percent of pixels covered by GFAP staining in control and MPTP-treated monkeys in the putamen (p=0.9048, Mann-Whitney). (E) Percent of pixels covered by GFAP staining in control and MPTP-treated monkeys in the primary motor cortex (p>0.9999, Mann-Whitney) (Control, N=5 monkeys; MPTP, N=4 monkeys).

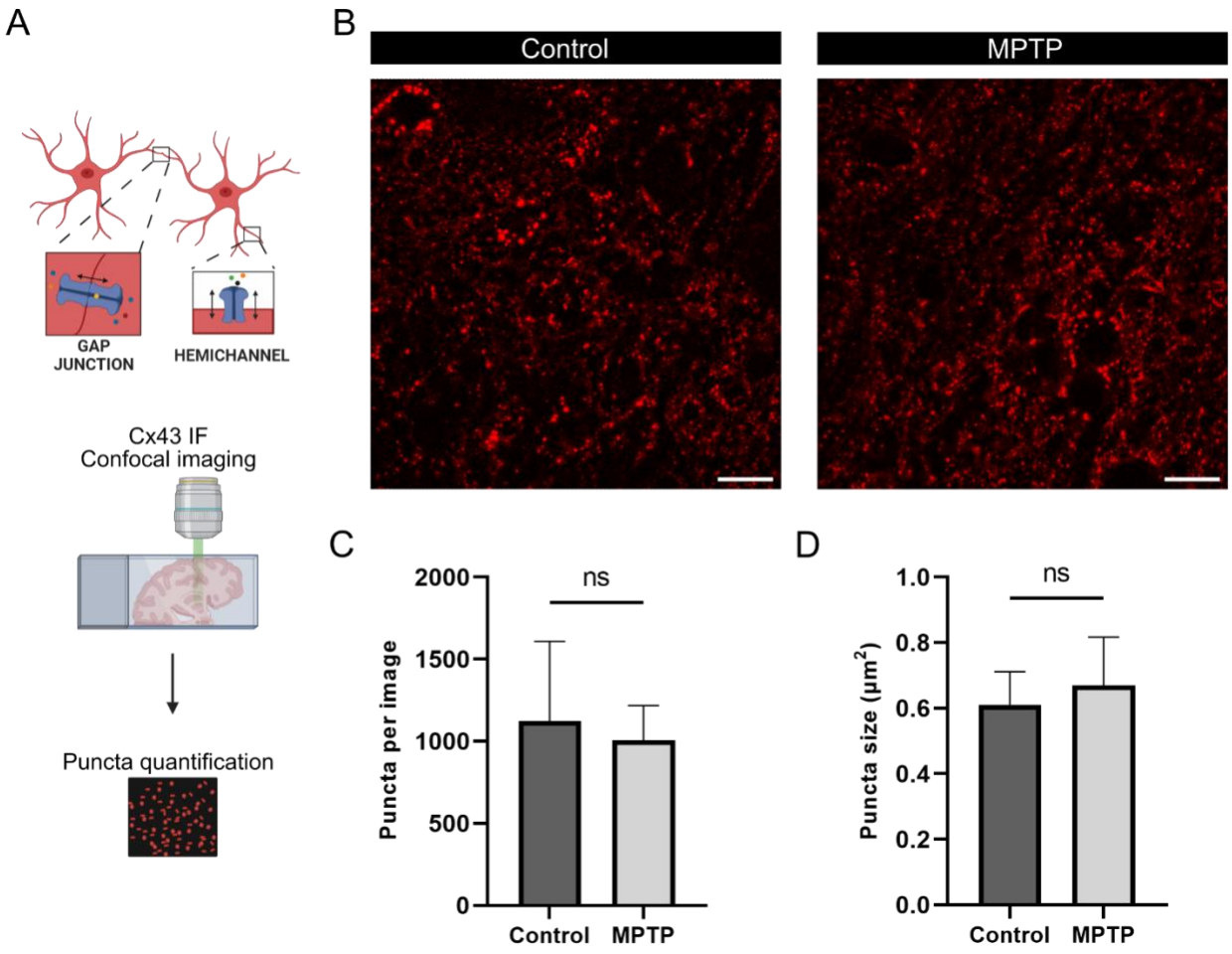

Figure 3.4 Cx-43 levels in the GPe of control and MPTP-treated animals.
(A) Schematic showing structure of gap junctions and hemichannels as well as the experimental setup. (B) Representative examples of cx-43 staining in the GPe of control (left) and MPTP-treated (right) monkeys. Scalebars 10 µm. (C) Average number of puncta per image (3 monkeys per group and 3 images per monkey; p = 0.3401, Mann-Whitney). (D) Average puncta size (3 monkeys per group and 3 images per monkey; p = 0.6048, Mann-Whitney).

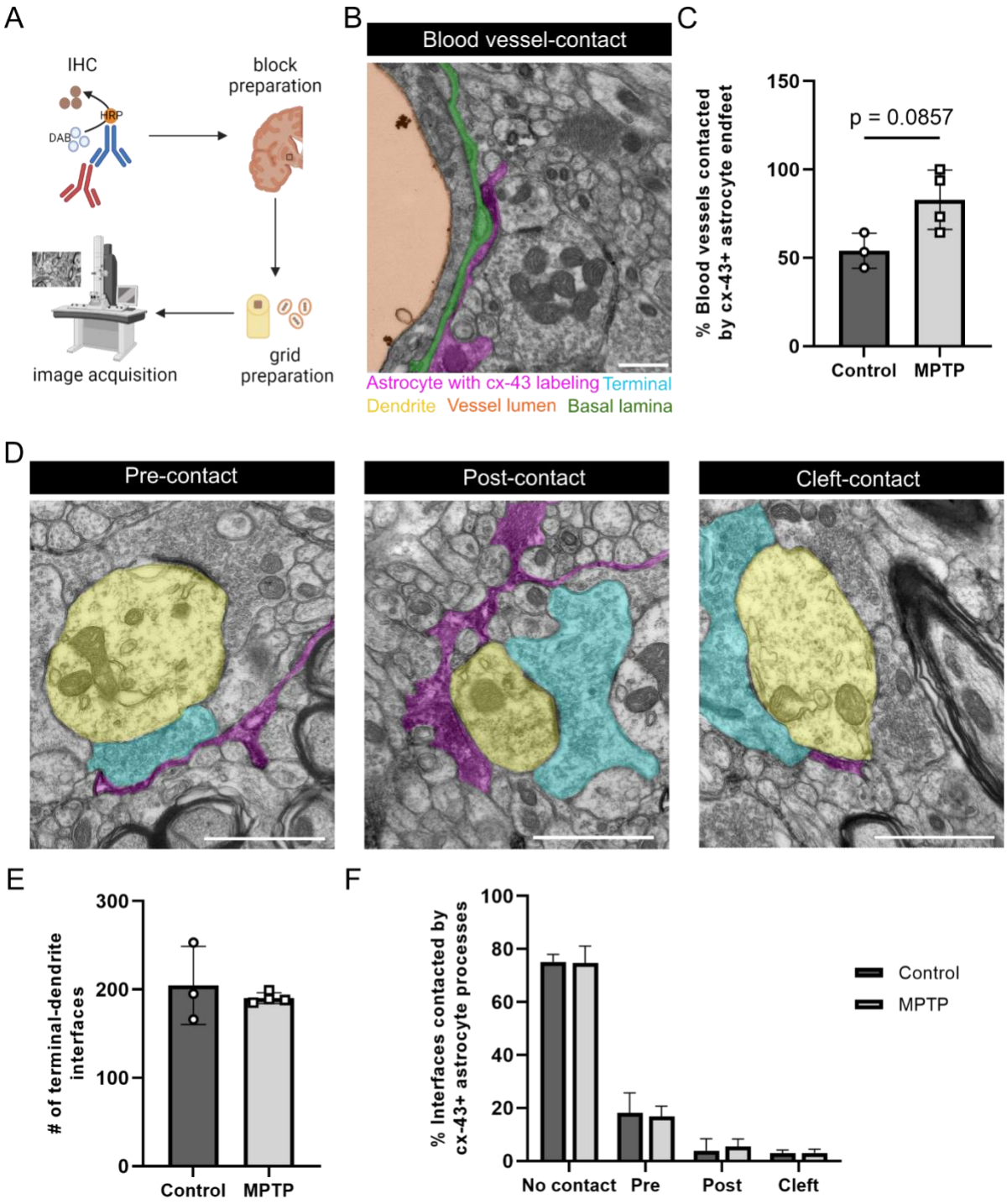

Figure 3.5 Localization of cx-43 in the GPe of control and MPTP-treated animals. (A) Schematic of tissue preparation. (B) Example of cx-43+ astrocyte process (magenta) contacting blood vessel (orange). Scalebar 1 µm. (C) Percentage of blood vessels contacted by cx-43+ astrocyte processes (p=0.0857, Mann-Whitney). (D) Examples of "pre," "post," and "cleft" contact types (dendrites: yellow; axonal terminals: cyan; cx-43+ astrocyte process: magenta). Scalebars 1 µm. (E) Total number of dendritic-terminal interfaces in control and

MPTP-treated monkeys in an equivalent area of tissue (3-4 monkeys per group, p=0.8571, Mann-Whitney). (F) Percentage of interfaces with cx-43+ astrocyte process contacts (3-4 monkeys per group, p=0.2312, chi-square).

CHAPTER 4: Functional assessment of astrocytes in the globus pallidus of normal and parkinsonian non-human primates

4.1 ABSTRACT

Depletion of striatal dopamine in Parkinson's disease (PD) results in abnormal neuronal activity throughout the basal ganglia circuitry, including aberrant oscillatory neuronal activity. Current circuit models of PD pathophysiology do not address astrocytic involvement, despite recent work demonstrating that astrocytes are essential for modulation of neuronal activity through a variety of functions. In addition, astrocytes form extensive networks via connexin-dependent gap junctions which have the potential to drive neuronal network activity. Connexin-43 (cx-43), the main protein that forms gap junctions in astrocytes, can be blocked *in vivo* with the use of mimetic peptides. We investigated how astrocyte networks modulate local neuronal activity in the external globus pallidus (GPe), a basal ganglia structure that displays astrocytic dysfunction in parkinsonism. Using mimetic peptides and *in vivo* electrophysiological recordings, we find that cx-43 blockade does not have clear effects on the firing properties of individual GPe neurons. However, we show that cx-43 blockade may exacerbate pathological changes in local field potentials following dopamine depletion. Our findings suggest that GPe astrocytes, through cx-43, may regulate the population activity of GPe neurons.

4.2 INTRODUCTION

In PD patients and animal models of parkinsonism, motor deficits are related to aberrant neuronal firing rates and patterns in basal ganglia, and related thalamic and cortical structures. In addition, there is increased inter-neuronal synchronization and pathologic oscillatory activity in these structures (Galvan et al., 2015b). Oscillations are generated by synchronized firing of large neuronal networks and increased power of oscillations relies on enhanced strength of neuronal synchrony. Oscillations may be sustained over time or influenced by transient burst events (Ede et al., 2018). In healthy individuals, beta oscillations (approximately 8-35 Hz) may signal the current sensorimotor state (Engel and Fries, 2010). However, beta oscillations are substantially

increased in PD patients (Brown et al., 2001). Additionally, symptom severity is correlated with increased oscillatory activity below 15 Hz and decreased activity above 15 Hz in the motor cortex and basal ganglia of the non-human primate (NHP) 1-methyl-4-phenyl-1,2,3,6-tetrahydropyridine (MPTP) model of parkinsonism (Devergnas et al., 2014a). Changes in beta oscillatory power have received considerable attention because they are significantly attenuated by current antiparkinsonian treatments such as dopaminergic medications and DBS (Jenkinson and Brown, 2011).

Despite implications in the symptoms of parkinsonism, the origin of the oscillatory activity remains unknown. While some investigators argue for a striatal origin, others focus on the subthalamic nucleus (STN)-GPe loop (Bevan et al., 2002; McCarthy et al., 2011; Nevado-Holgado et al., 2014). Due to the recurrent inhibitory-excitatory connections of the GPe and STN, the loop is prone to oscillations (Bevan et al., 2002). In addition to recurrent inhibitory-excitatory connections that facilitate oscillations, the GPe displays changes in neuronal activity and influence over other basal ganglia structures in parkinsonism. In parkinsonian monkeys, GPe neurons have lower firing rates and increased incidences of bursting compared with healthy animals (Tachibana et al., 2011). The changes in firing rate and bursting seen in MPTP treated monkeys were also found in the GPe of PD patients (Hutchison et al., 1994). This change in GPe outflow influences activity of other basal ganglia structures, particularly the STN (Fan et al., 2012). Manipulation of GPe activity by electrical stimulation or pharmacological intervention decreased pathological activity in the STN, and disruption of the loop either by lesion of the GPe or STN stimulation reduces beta oscillations in MPTP treated monkeys (Meissner et al., 2005; Soares et al., 2004). Additionally, selective optogenetic or electrical stimulation of GPe-STN projecting neurons in a rodent model of PD improved motor symptoms (Mastro et al., 2017; Spix

et al., 2021). Thus, the GPe may be a significant contributor to pathological neuronal activity in parkinsonism.

Astrocytes represent an understudied contributor to pathological oscillations and abnormal neuronal activity. Specifically within the GPe, astrocytes demonstrate deleterious functions in dopamine depleted animals, such as changes in glutamate and GABA metabolism which directly impact neuronal activity (Chazalon et al., 2018; Cui et al., 2016). Astrocytes form extensive networks via gap junction channels composed of connexins (primarily cx-43), providing a means of long-distance communication and redistribution of many neuroactive substances such as neurotransmitters and ions (Chever et al., 2016; Pannasch et al., 2011). Nonspecific blockade of gap junctions in the GPe of dopamine depleted mice resulted in decreased beta oscillatory activity and recovered motor function, however, it remains uninvestigated whether neuronal or astrocytic gap junctions contributed to this result (Phookan et al., 2015). To investigate the potential contribution of astrocyte gap junctions to the aberrant GPe neuronal activity in parkinsonism, we utilized cx-43 blockers during neuronal recordings in MPTP-treated rhesus monkeys. Monkeys treated with MPTP reliably reproduce the pathophysiology of parkinsonism, as the connectivity of the basal ganglia and related structures in non-human primates closely resembles that in humans (Parent, 1986), and MPTP leads to a parkinsonian state that replicates most of the motor impairments of PD patients (Emborg, 2007). Furthermore, based on my results (Chapter 2), the morphology of astrocytes and the astrocyte-neuronal interactions in monkeys are likely to be more similar to humans than in other animal models.

4.3 MATERIALS AND METHODS

4.3.1 Animals

All procedures were approved by the Animal Care and Use Committee of Emory University and performed in accordance with the Guide for the Care and Use of Laboratory

Animals (NRC, 2010) and the U.S. Public Health Service Policy on the Humane Care and Use of Laboratory Animals (revised 2015). All rhesus macaques were sourced from the Emory National Primate Research Center (ENPRC). The monkeys were maintained in a controlled environment with a 12-hour light/dark cycle, had free access to water, and were fed twice daily.

Table 4.1. Animals

Sex	Code	Age at perfusion	Group	Experiment(s)
F	MR359	7 years 8 months	Control	Single unit, LFP
M	MR368	5 years 4 months	Control	Single unit, LFP
F	MR354	8 years 6 months	MPTP	Single unit, LFP, TH
F	MR342	7 years 6 months	MPTP	Single unit, TH
M	MR362	6 years 10 months	MPTP	Single unit, LFP, TH
F	MR350	8 years 10 months	MPTP	Single unit, TH
F	MR369	10 years 4 months	MPTP	LFP, TH
M	MR315	5 years 8 months	Control	TH
M	MR316	5 years 8 months	Control	TH
M	MR322	4 years 2 months	Control	TH
Experiment details: Single unit – extracellular recordings of individual neurons with drug injections, LFP – local field potential recordings with drug injections, TH – tyrosine hydroxylase staining.				

4.3.2 Recording chamber placement surgery

Prior to chamber placement surgery, all animals were trained to sit in a primate chair using positive reinforcement methods. Once acclimated to the primate chair, the monkeys underwent surgery to place the chambers. Each animal was sedated with ketamine (10mg/kg), intubated for isoflurane anesthesia (maintained at 1-3%), and placed in a stereotactic frame. The anesthesia was administered and monitored by a veterinary technician. Vital signs were monitored during the surgery (heart rate, respiration, oxygen saturation, and CO2). Two trephine holes were made in the skull, exposing the dura mater. The exposed dura was then covered by two stainless steel recording chambers (Crist Instruments, Hagerstown, MD; inner chamber diameter = 16 mm) positioned at a 20-30^{o} angle from vertical and directed stereotaxically to the basal ganglia (according to (Paxinos et al., 2000). The chambers were embedded into an acrylic skull cap, along with a stainless-steel head holder and bone screws. At the end of the surgery, the

incision was sutured in layers, and the subject recovered from anesthesia before returning to its home cage. Post-operatively, the subject was treated with buprenorphine (0.03 mg/kg) and banamine (1 mg/kg) as analgesics, as well as rocephin (25 mg/kg) to prevent infection.

4.3.3 MPTP treatment and motor assessment

Five monkeys received weekly injections of MPTP (0.2-0.8 mg/kg/week; Sigma, St. Louis, MO; total cumulative doses ranged from 4.1 to 18.4 mg/kg, total treatment time ranged from 1 to 10 months). Behavior was assessed weekly during MPTP treatment by two methods: 1) A parkinsonism rating scale that includes bradykinesia, arm and leg akinesia, limb and trunk posture, action tremor, finger dexterity, cage activity, balance, and freezing; each item was scored 0-3 (absent to severe, 30 maximal score)(Devergnas et al., 2014b; Soares et al., 2004). 2) Quantification of the spontaneous overall movement using a custom video analysis algorithm (Caiola et al., 2019). Animals were treated with MPTP until they demonstrated mild-to-moderate parkinsonism (defined as score of 5-10 for mild and 11-15 for moderate in the rating scale and reduction in movement activity to ≤60% from baseline levels). Parkinsonism was considered stable if these measurements remain consistent for ≥4 weeks after the last MPTP injection.

4.3.4 Tyrosine hydroxylase (TH) immunoperoxidase

Three sections per animal corresponding to approximate levels 12.45, 15.15, and 20.1 from the interaural line were selected for analysis (Paxinos et al., 2000). Sections were incubated in a solution of 1% normal serum, 1% BSA, and 0.3% Triton X-100 in PBS. Sections were then incubated overnight in the blocking/permeabilization solution containing antibodies for TH (see Table 3.2). Binding sites were revealed using a biotinylated secondary antibody (Table 3.2). Sections were incubated in the secondary solution for 90 minutes and rinsed in PBS. Sections were then incubated in an ABC solution (1:200, Vector Laboratories) containing 1% BSA and 0.3% Triton X-100 for 90 minutes. Followed by rinses in PBS and TRIS buffering solution

(0.05M, pH 7.6), sections were incubated in TRIS buffer containing 0.025% 3,3'-diaminobenzidine tetrahydrochloride (DAB; Sigma), 10 mM imidazole, and 0.006% hydrogen peroxide for 10 minutes, immediately followed by PBS rinses. Following mounting, sections were dehydrated in a graded series of alcohol and toluene, then coverslipped. Slides were scanned with an Aperio Scanscope CS system (Leica).

Images of scanned slides were acquired at a zoom of 0.5x in Aperio's ImageScope software and exported to ImageJ. For each section, the caudate and putamen were divided into dorsolateral and ventromedial areas, by drawing a line approximately parallel to the lateral edge of the structure. The image was then inverted, and the integrated density was measured in each area. Data is represented as proportion of the average integrated density measured in control animals.

4.3.5 Electrophysiological mapping of brain regions and overall experimental design

Electrophysiological mapping sessions were conducted to identify the location of the GPe in the chamber, using the characteristic firing patterns of the structure (DeLong, 1973, 1971). Neurons in the GPe were identified by their location ventral to the putamen as well as their high frequency and persistent activity. Once the GPe was identified, I proceeded with the injection experiments. All recordings were performed in awake monkeys. Monkeys were monitored during recording sessions via video (and in some cases, electroencephalogram) for levels of arousal. The animals were sitting in a primate chair with their heads restrained, but arms and legs free to move. In each recording session, the dura was pierced with a guide cannula. The guide cannula housed a custom-made probe ("injectrode") that combined an injection tubing and a standard tungsten recording electrode (impedance of 0.5- 1.0 MΩ at 1 kHz; FHC, Bowdoinham, ME) (Kliem and Wichmann, 2004). The injectrode was coupled to a peristaltic pump (CMA 402,

CMA Microdialysis, Sweden) and positioned in the GPe using a microdrive (NAN Instruments, Israel).

Two types of GPe injections were done in separate experiments. To assess the contribution of astrocyte networks and hemichannel activity in the GPe to aberrant neuronal firing rates and patterns in parkinsonism, I injected a small volume (microinjection) of Gap27 during extracellular recordings of GPe neurons. I used commercially available scrambled Gap27 (Gap27sc) as a control (Stehberg et al., 2012). To assess the contribution of astrocytic networks in the GPe to pathological oscillatory activity in the basal ganglia-thalamo-cortical motor circuit, I injected a larger volume (bolus injection) of Gap27 or Gap27sc with LFP recordings in GPe.

4.3.6 Drugs

The cx-43 mimetic peptide Gap27 (300 µM; Tocris), and the Gap27sc peptide (300 µM; AnaSpec) were used. The choice of concentration was based on previous *in vivo* rodent data showing effects on local field potentials and testing *in vitro* (Bazzigaluppi et al., 2017; Boitano and Evans, 2000; EbrahimAmini et al., 2021). This concentration also avoided non-specific binding while impacting hemichannels (<5 minutes) and gap junctions (>20 minutes) at different time courses (Decrock et al., 2009; Wang et al., 2012).

Preliminary experiments in our lab using high performance liquid chromatography (HPLC, Emory HPLC Bioanalytical Core), verified that the Gap27 peptide was not degraded after passing through the injection system. The drugs were dissolved in artificial cerebrospinal fluid (aCSF, comprised of (in mM) 143 NaCl, 2.8 KCl, 1.2 CaCl2, 1.2 MgCl2, 1 Na2HPO4).

4.3.7 Microinjections with simultaneous single-unit recordings

Once lowered into the GPe, the electrode was left in position for at least one minute before the start of recording. Following 2-3 minutes of baseline recording, 0.2 µl of Gap27 (300 µm, Tocris-BioTechne, Minneapolis, MN) or in control experiments, scrambled Gap27 peptide

(Gap27sc, 300 µm, Anaspec, Freemont, CA) was infused at a rate of 0.2 µl/minute. The injectrode was left in place and activity was recorded for a minimum of 5 minutes following injection. Extracellular neuronal electrical signals were recorded, amplified (DAM-80 amplifier; WPI, Sarasota, FL), filtered (300-5,000 Hz; Krohn-Hite, Brockton, MA), and displayed on a digital oscilloscope (DL1540; Yokogawa, Tokyo, Japan). Neuronal signals were digitized (sampling rate 50 kHz) and stored on a hard drive using a data acquisition interface (Power1401; CED, Cambridge, UK) and commercial software (Spike2, CED) for off-line analysis.

4.3.8 Analysis of single-unit recordings

Spike sorting was performed offline using a template matching algorithm and principal component analysis (Spike2). To confirm that the template waveform contained a single neuron, inter-spike interval (ISI) histograms were generated. Only records with less than 2% of ISIs falling below 2 ms were used for further analysis. We then generated isolation scores for each neuron (Joshua et al., 2007). Only neurons with an isolation score greater that 0.8 (scale 0-1) were included in further analysis. Neuronal recordings that met both ISI histogram and isolation score criteria were exported to MatLab for further analysis. ISI data was parsed into 60-second bins to examine several parameters including firing rate, ISI coefficient of variation, proportion of spikes in bursts, and proportion of time in decelerations (Sanders et al., 2013). Bursting and deceleration was detected using the surprise detection algorithm with a cutoff surprise value of 3 (Legéndy and Salcman, 1985). The proportion of ISIs within bursts and proportion of time in decelerations was then calculated. To evaluate drug effects, the effect ratio was calculated as the effect/baseline, where the baseline period was considered to be the minute before injection start, and the effect period was the minute immediately after injection termination.

To further investigate effects of Gap27 on individual neuron activity in the GPe, we used permutation tests. Using a custom MatLab script, we isolated the 1000 ISIs of recording prior to

injection start and the 1000 ISIs of recording following injection completion and concatenated the two records. The code then randomly shifted the line of demarcation, that is the line that separates the "pre-injection" portion of the record from the "post-injection" portion of the record 250 times. For each shift of ISI sequences, a z-value was calculated. The final permutation statistic evaluated what proportion of z-values of the shifted ISI sequences would be larger than the absolute z-value of the original sequence. A permutation statistic less than 0.05 was considered significant.

4.3.9 Drug bolus injections with simultaneous local field potential recordings

The injection and recording procedure were the same as single unit recordings (section 4.3.7) except for the following parameters. Following 10 minutes of baseline recording, 2 µl of Gap27 (300 µm, Tocris) or Gap27sc peptide (300 µm, Anaspec) was infused at a rate of 0.2 µl/minute. The injectrode was left in place 45-60 minutes after the end of the injection. LFPs were obtained by filtering the signal (0.5-100 Hz 4^{th} order Butterworth; Krohn-Hite, Brockton, MA). The signals were digitized (sampling rate 50 kHz) and stored on a hard drive using a data acquisition interface (Power1401; CED, Cambridge, UK) and commercial software (Spike2, CED) for off-line analysis.

4.3.10 Analysis of local field potential recordings

The Spike2 files were downsampled from 50 kHz to 5 kHz and exported as MatLab files. The MatLab files were then opened in Python. All analysis was conducted offline using a custom Python script to implement the "Fitting Oscillations One Over F" (FOOOF) algorithm (Donoghue et al., 2020). First, power spectral density was computed using the Welch technique with Hamming windowing and a fast Fourier transform segment length of 8192 samples with no overlap, resulting in a final spectral resolution of 0.61 Hz and time resolution of 1.64 seconds across the 0-40 Hz range (higher frequencies were not included in analysis). Power spectral

density was computed for baseline (60 seconds preceding the start of the injection), as well as for 60-second epochs at 30-, 45-, and 60-minutes post-injection. Then, power spectral densities were parameterized using FOOOF. Settings for the algorithm were set as: peak width limits: 1-12; max number of peaks: 8; minimum peak height: 0; peak threshold: 1; and aperiodic mode: fixed. Power spectra were parameterized across the frequency range 0 to 40 Hz. All recordings yielded an average R^2 of 0.9831 and standard error of 0.068 for the algorithm fit. Once all parameterized power spectra were computed, percent change from baseline recordings were assessed for the 3 post-injection timepoints (30-, 45-, and 60-minutes post-injection).

4.3.11 Statistical analysis and figures

Normality was first assessed using the D'Agostino-Pearson test. Two group comparisons were made using unpaired Mann-Whitney or unpaired t-tests. The results of statistical analysis, n, and p-values are included in figure legends. N is defined as number of animals or neurons depending on analysis and is described in the figure legend. Statistics were run using GraphPad Prism 9. Data are represented as mean ± SD. In all figure plots, p-values are represented by asterisk(s): $*$ for $p < 0.05$; $**$ for $p < 0.01$; $***$ for $p < 0.001$; $****$ for $p < 0.0001$. All schematics for figures were made using BioRender.com.

4.4 RESULTS

4.4.1 MPTP treatment induces parkinsonism

We assessed the degree of dopamine depletion with postmortem immunostaining for tyrosine hydroxylase (TH). MPTP-treated animals had reduced TH levels in both caudate and putamen compared to normal animals, with the greatest reduction occurring in post-commissural dorsolateral regions (Figure 4.1A-D). This pattern of dopaminergic denervation after MPTP treatment is consistent with previous publications (Masilamoni and Smith, 2018). We also assessed the degree of parkinsonism in monkeys treated with MPTP using a modified Parkinson's disease Rating Scale (PRS). Most animals qualified as mildly parkinsonian, with 4

out of 5 receiving final PRS scores of 8-10. One animal qualified as moderately parkinsonian with final PRS score of 11 (Figure 4.1E). All animals demonstrated stable parkinsonian symptoms, having received mild-to-moderate range PRS scores for at least 4 weeks prior to MPTP cessation. MPTP-treated monkeys also displayed overall reductions in activity compared to baseline, as assessed by video analysis (Figure 4.1F).

4.4.2 Changes in GPe neuronal firing following dopamine denervation

We first assessed the baseline firing properties of GPe neurons. We found that GPe neurons in parkinsonian animals had a baseline firing rate of 47.25 ± 24.55 spikes/second compared to 65 ± 28.33 spikes/second in control animals (p=0.0153, t-test, Figure 4.2B). These results confirmed previous findings showing that GPe neurons have lower firing rates and increased bursting and pausing patterns in dopamine depleted animals (Soares et al., 2004; Wichmann and Soares, 2006). There was a trend toward higher interspike interval coefficient of variation (ISI CV) in parkinsonian animals (1.377 ± 0.8044 in control and 1.671 ± 0.7424 parkinsonian), though this was not statistically significant (p=0.0753, Mann-Whitney, Figure 4.2C). Both the proportion of spikes in bursts (p=0.008, t-test, Figure 4.2D) and time spent in decelerations (p=0.0119, t-test, Figure 4.2E) were greater in parkinsonian animals which is consistent with previous studies in humans and animal models (Hutchison et al., 1994; Miller and DeLong, 1987; Wichmann and Soares, 2006).

4.4.3 Changes in GPe local field potentials following dopamine denervation

We assessed the periodic and aperiodic features of GPe LFPs. Consistent with previous studies, we found increased power following MPTP in the 7-15 Hz range (p=0.0382, Multiple Mann-Whitney with Holm Sidak correction, Figure 4.3B), which corresponds to low beta power in monkeys (Devergnas et al., 2014b). We did not find significant differences between control and parkinsonian animals in other frequency ranges (3-7 Hz, p=0.559; 15-23 Hz, p=0.551; 23-25

Hz, p=0.847). The aperiodic offset was significantly lower in parkinsonian monkeys (p<0.0001, Mann-Whitney, Figure 4.3C) as well as the aperiodic exponent (p=0.0293, Mann-Whitney, Figure 4.3D).

4.4.4 Effects of connexin-43 blockade in GPe single neuron activity

To assess the effects of blocking cx-43 on individual neuron activity in the GPe in control and MPTP-treated monkeys, we injected a small volume (2 µl) of Gap27 or Gap27sc. We compared firing rate and proportion of spikes in bursts at baseline (one minute before injection) and post-injection (one minute following injection termination). We did not find that Gap27 altered the firing rate in control (p=0.3622, Mann-Whitney, Figure 4.4A) or MPTP monkeys (p=0.7345, Mann-Whitney, Figure 4.4B) compared to Gap27sc control injections. We also looked at the effects of Gap27 in the proportion of spikes in bursts, given the increased bursting in dopamine depleted animals and that cx-43 knockout animals have reduced neuronal bursting (Chever et al., 2016; Miller and DeLong, 1987; Wichmann and Soares, 2006). Infusions did not alter the proportion of spikes in bursts in control (p=0.0885, Mann-Whitney, Figure 4.4C) or MPTP monkeys (p=0.7921, Mann-Whitney, Figure 4.4D) compared to Gap27sc control injections. Permutation tests suggested that Gap27 did not have an effect on neuronal firing patterns, as the number of neurons that had a z-value more extreme that their shifted null distribution was similar between Gap27sc and Gap27 in control and MPTP-treated monkeys (Table 4.2).

Table 4.2. Permutation analysis of GPe neurons following drug injection

	Control		MPTP	
	# of neurons	Permutation < 0.05	# of neurons	Permutation < 0.05
Gap27sc	13	5	8	4
Gap27	15	6	12	7

4.4.5 Effects of cx-43 blockade in GPe local field potentials in parkinsonian animals

Since we found significant differences in 7-15 Hz power, aperiodic offset, and aperiodic exponent between control and parkinsonian groups (section 4.4.3, Figure 4.3), we selected these parameters to analyze effects of cx-43 blockade in parkinsonian animals. We first examined the time course of the drug effects, by comparing these parameters at 30-, 45-, and 60-minute post-injection to baseline (Figure 4.5A-C). For all selected parameters, on average, the largest change from baseline was found at 45-minutes post-injection. We then compared Gap27sc and Gap27 effects at 45-minutes post-injection from baseline. When compared to Gap27sc control injections, Gap27 did not have a significant effect in the 7-15 Hz power ($p=0.7802$, Mann-Whitney, Figure 4.5D). However, when compared to Gap27sc, infusions of Gap27 significantly reduced the aperiodic offset ($p=0.022$, Mann-Whitney, Figure 4.5E) and aperiodic exponent ($p=0.0435$, Mann-Whitney, Figure 4.5F).

4.5 DISCUSSION

Our results confirm previous findings that both individual neuronal firing patterns and local field potentials in the GPe are affected following dopamine depletion. All animals in the study treated with MPTP showed reduction of tyrosine hydroxylase immunoreactivity and motor impairments consistent with mild-to-moderate parkinsonism (Devergnas et al., 2014b; Galvan et al., 2014; Wichmann et al., 2001). Neurons in the GPe displayed reduced firing rates, increased bursting, and increased time spent in decelerations consistent with previous studies in animal models (Galvan et al., 2011; Miller and DeLong, 1987), and also in PD patients (Hutchison et al., 1994). Local field potential (LFP) recordings in the GPe also displayed increased power in the 7-15 Hz range. Increased power below 15 Hz is associated with dopamine depletion in parkinsonian monkeys across basal ganglia structures and may correspond to exacerbated beta power activity seen in Parkinson's disease patients (Devergnas et al., 2014b).

The LFPs also displayed decreased aperiodic offset and aperiodic exponent in parkinsonian animals. While the underlying mechanisms contributing to the aperiodic components of the power spectral density (PSD) are unknown, studies suggest it may reflect the excitation-inhibition balance and/or sum of pre- and post-synaptic currents (Baranauskas et al., 2012; Donoghue et al., 2020; Gao et al., 2017). Reduced aperiodic PSD components have been seen in the STN of parkinsonian rodents (Kim et al., 2022) and PD patients (Wiest et al., 2023), and treatment with levodopa reversed the decreased aperiodic offset and exponent, suggesting that it is directly related to changes caused by dopamine depletion (Kim et al., 2022). As the STN and GPe are reciprocally connected, our finding of decreased aperiodic offset in the GPe of parkinsonian monkeys could be a manifestation of the dysregulation in STN-GPe network (Kovaleski et al., 2020).

Blockade of cx-43 did not cause any consistent changes in individual neuron firing rates or patterns. The lack of consistent effects of Gap27 in firing rate or bursting may be, at least in part, due to the variable nature of GPe neuron activity. Neurons in the GPe are known for characteristic high frequency activity interspersed with bursting, although a minority of neurons exhibit low frequency activity with prominent bursting (DeLong, 1971; Katabi et al., 2023). While it was previously thought that individual neurons fell into one of these categories, longer recordings suggest that an individual cell can transition between the two firing patterns (Elias et al., 2008). Such temporal variability makes interpretation of the drug's effects on the neuron's activity challenging, even in our experiments that comprised several minutes before and after infusion of a drug. Furthermore, the GPe neuronal population is not homogeneous. Rodent studies have described subpopulations of GPe neurons with characteristic protein expression and firing properties (Courtney et al 2023). However, extracellular recordings in the GPe in monkeys

do not allow for reliable identification of these cell types. For this reason, we cannot rule out the possibility of astrocyte cx-43 hemichannels and gap junctions exerting effects preferentially on subtypes of neurons in the GPe.

Although Gap27 did not result in consistent changes in 7-15 Hz power, we found other effects of Gap27 on local field potentials in parkinsonian animals. Injection of Gap27 specifically affected the aperiodic PSD components, further exacerbating the decreased offset and exponent seen in parkinsonian animals at baseline. There may be various mechanisms underlying this effect. Aperiodic components have been correlated with fMRI BOLD signals, suggesting a possible neuro-vascular contributor to this parameter of the LFP (Winawer et al., 2013). As fMRI BOLD signal is related to neural circuit energy consumption (Sokoloff, 1977), and astrocytes are responsible for uptake and distribution of metabolites from the blood (Rouach et al., 2008), the increase in cx-43 in the endfeet of MPTP-treated monkeys (described in Chapter 3) and changes to the aperiodic offset following Gap27 injection suggest that cx-43 may partly participate in this exchange.

4.6 LIMITATIONS

First, our studies did not include a dose-response curve of Gap27. The generation of a dose response curve is limited by the inability to directly measure astrocyte coupling *in vivo*, the primary target of Gap27. Astrocyte coupling can only be measured in *ex vivo* slice preparations. While the drug has been shown to block astrocytic gap junctions in *ex vivo* slices (Bellot-Saez et al., 2018; Boitano and Evans, 2000), the exact time course and concentration *in vivo* has not been thoroughly characterized. Thus, we selected the concentration and time course for analysis based on other studies *in vivo*, *ex vivo*, and *in vitro* (Bazzigaluppi et al., 2017; Bellot-Saez et al., 2018; EbrahimAmini et al., 2021), but we cannot rule out that the concentration was too low to produce electrophysiological effects. Second, cx-43 also forms gap junctions between endothelial cells.

Thus, the effects seen on the PSD could be the result of actions on endothelial gap junctions rather than astrocyte gap junctions. Even so, the reduced aperiodic offset and exponent seen in parkinsonian animals following Gap27 injections is interesting and should be further investigated.

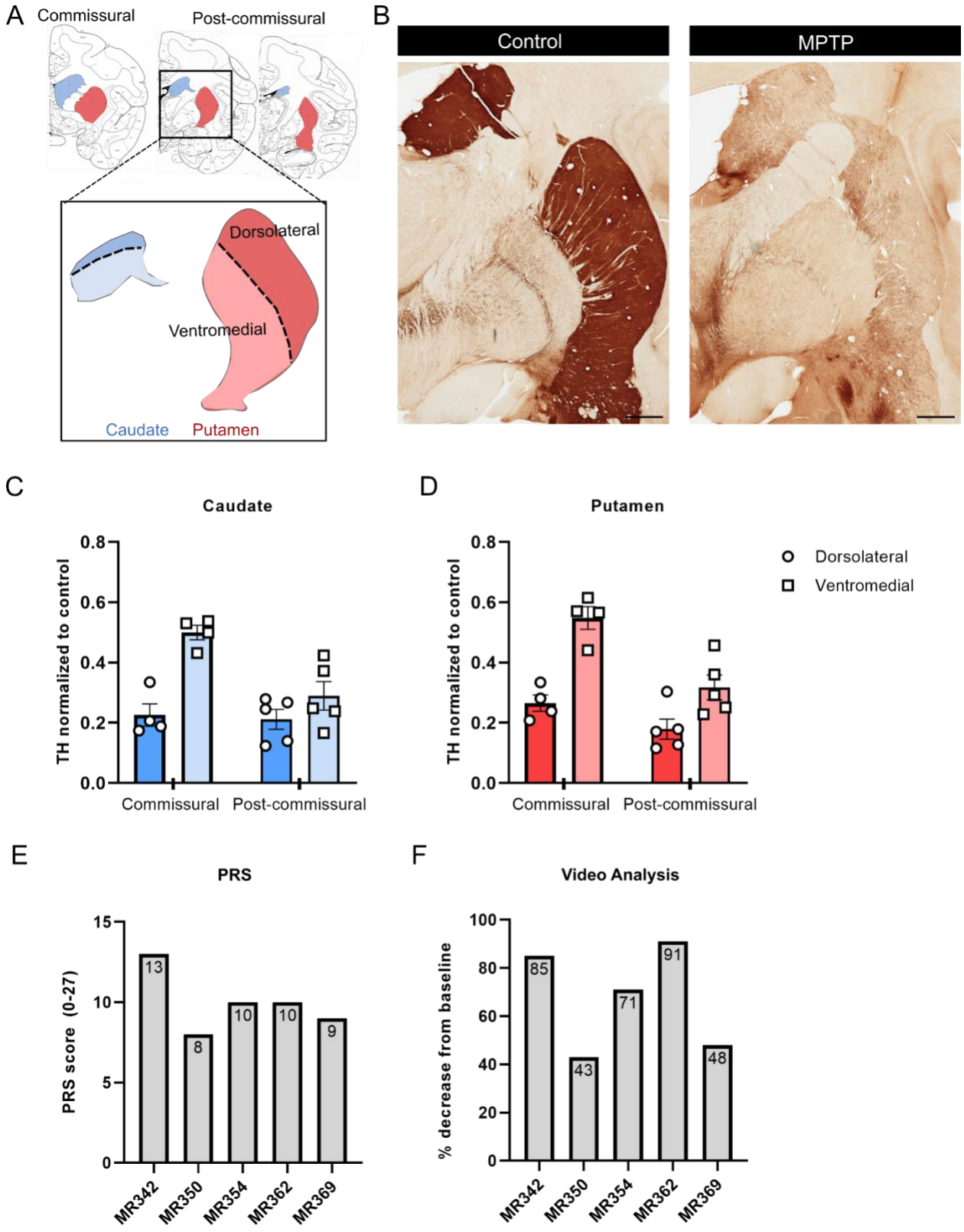

Figure 4.1 Parkinsonism Rating Scale (PRS) and tyrosine hydroxylase (TH) immunoreactivity in animals following MPTP treatment.

(A) Schematic of regions selected for TH integrated density analysis. (B) Representative examples of TH staining in control and MPTP treated monkeys. Scalebars 2mm. (C) Integrated density of TH staining in the caudate of MPTP-treated monkeys relative to control monkeys. Commissural and post-commissural as well as dorsolateral and ventromedial areas were measured separately. (D) Integrated density of TH staining in the putamen. For TH staining quantification, $N_{control}$=3 monkeys, N_{MPTP}=5 monkeys. (E) PRS scores of MPTP treated animals once they displayed stable parkinsonism. (F) Video analysis of percent reduction in movement from baseline for MPTP treated animals.

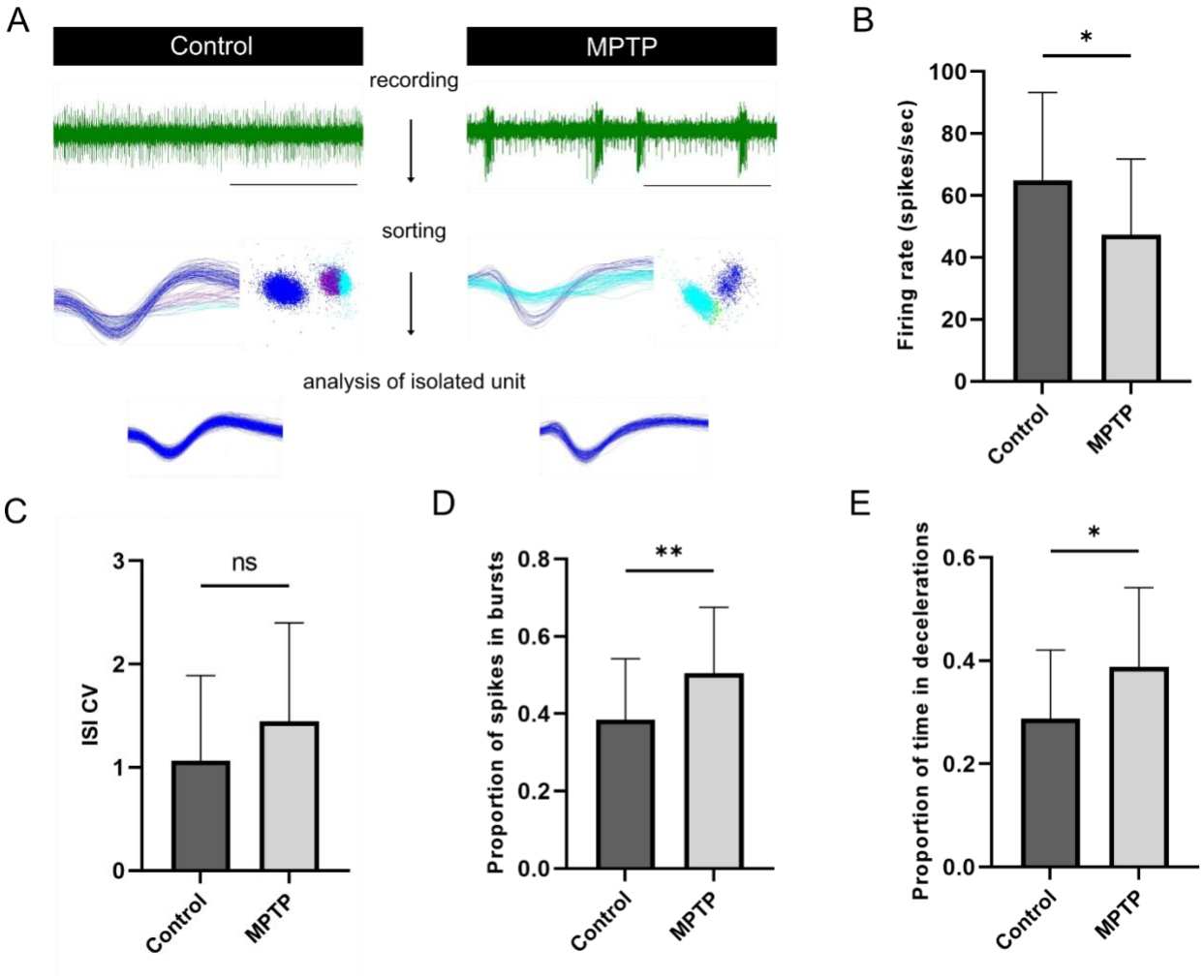

Figure 4.2 Electrophysiological effects of MPTP treatment on individual neurons in the GPe.

(A) Schematic of experimental workflow: top: raw traces from extracellular recordings (scalebars 1 sec) middle: isolated cell (royal blue) from noise and others (cyan, purple, and green) with principal components analysis bottom: isolated cells used for further analysis. (B) Mean firing rates from 60 seconds of recording of individual neurons in the GPe of control and MPTP treated monkeys (p=0.0153, t-test). (C) Interspike interval coefficient of variation (p=0.0753, Mann-Whitney). (D) Proportion of spikes in bursts (p=0.008, t-test) (E) Proportion of time in decelerations (p=0.0119, t-test). For all panels, number of neurons $N_{control}$=28 from 2 monkeys; N_{MPTP}=28, from 4 monkeys.

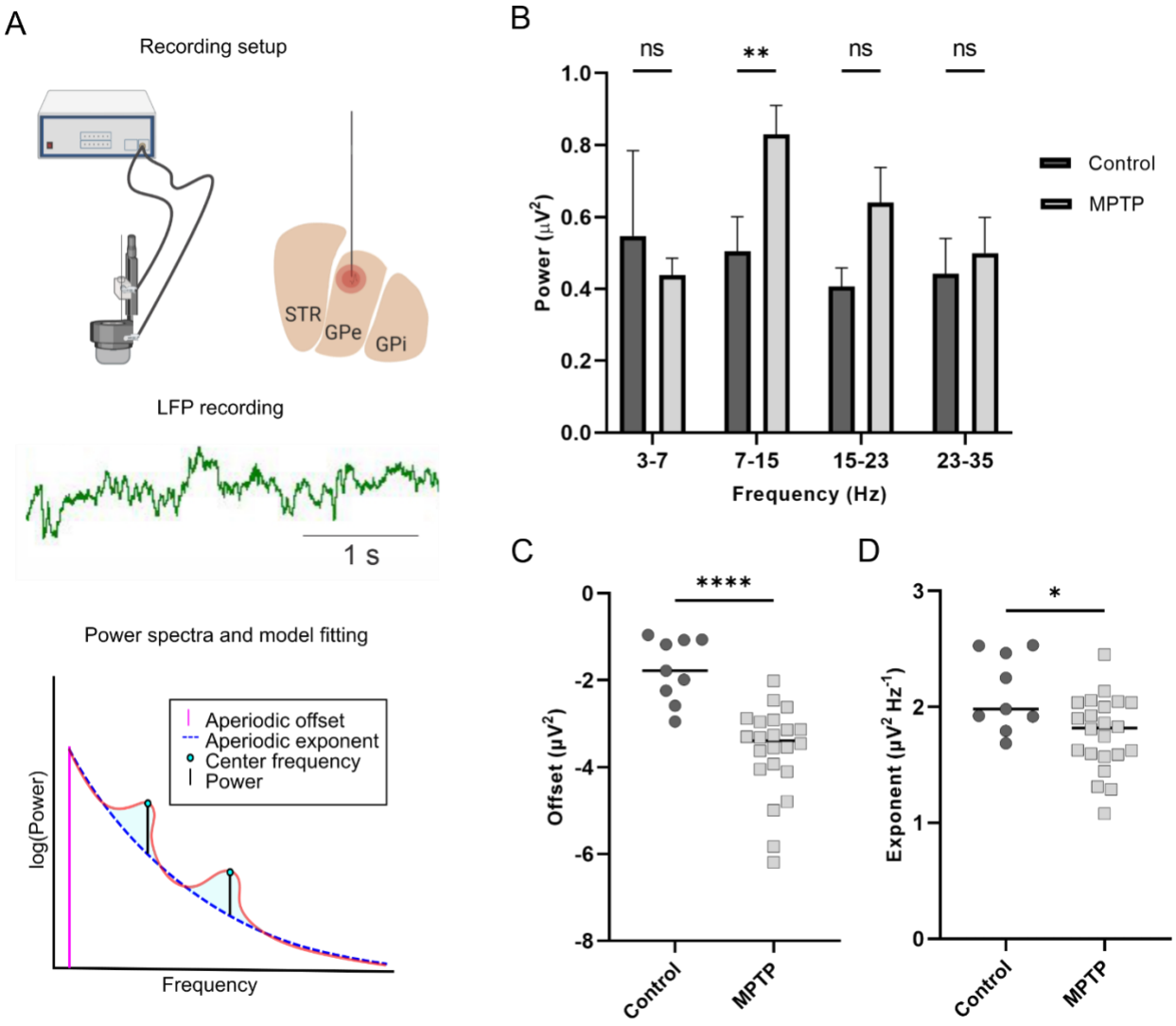

Figure 4.3 Electrophysiological effects of MPTP treatment on local field potentials in the GPe.

(A) Schematic of workflow: top: recording setup, middle: raw LFP recordings, and bottom: generation of power spectra and model fitting. (B) Power spectrum from 60 seconds of baseline recording in control and MPTP monkeys (3-7Hz: p=0.559, 7-15Hz: p=0.0382, 15-23Hz: p=0.5509, 23-35Hz: p=0.847, Multiple Mann-Whitney with Holm-Sidak correction, number of recordings $N_{control}$=9 from 2 monkeys; N_{MPTP}=20 from 4 monkeys). (C) Aperiodic offset (p<0.0001, Mann-Whitney, $N_{control}$=9 from 2 monkeys; N_{MPTP}=22 from 4 monkeys). (D) Aperiodic exponent (p=0.0293, Mann-Whitney, $N_{control}$=9 from 2 monkeys; N_{MPTP}=22 from 4 monkeys).

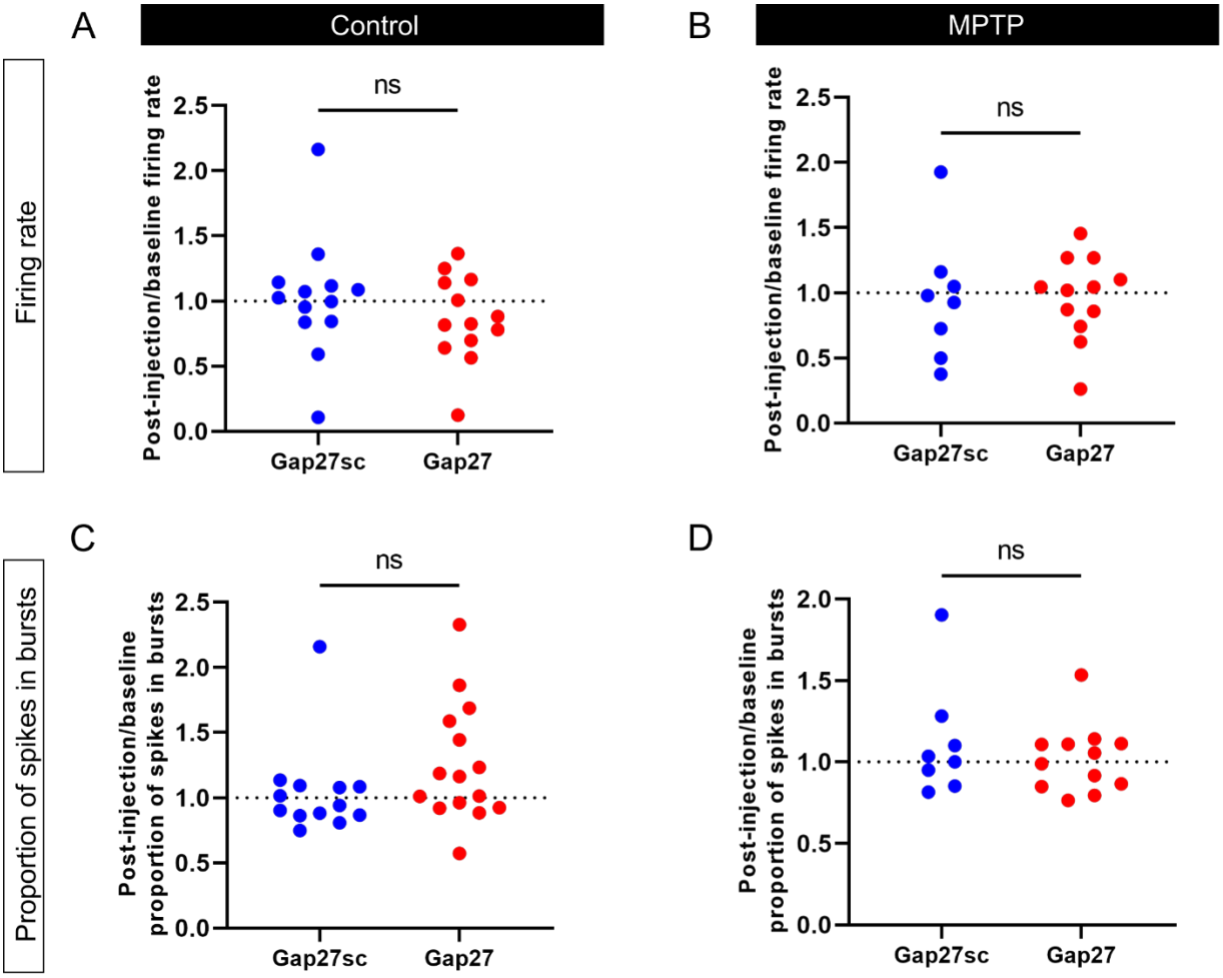

Figure 4.4 Effects of Gap27 on the firing of individual GPe neurons.
(A) Effect ratio (effect/baseline) of firing rate in control monkeys following injection of scrambled Gap27 or Gap27 (p=0.3622, Mann-Whitney). (B) Effect ratio of firing rate in MPTP-treated monkeys (p=0.7345, Mann-Whitney). (C) Effect ratio of proportion of spikes in bursts in control monkeys (p=0.0885, Mann-Whitney). (D) Effect ratio of proportion of spikes in bursts in MPTP-treated monkeys (p=0.07921, Mann-Whitney). For Gap27sc recordings, $N_{control}$=15 from 2 monkeys; N_{MPTP}=8 from 4 monkeys and for Gap27 recordings, $N_{control}$=13 from 2 monkeys; N_{MPTP}=12 from 4 monkeys.

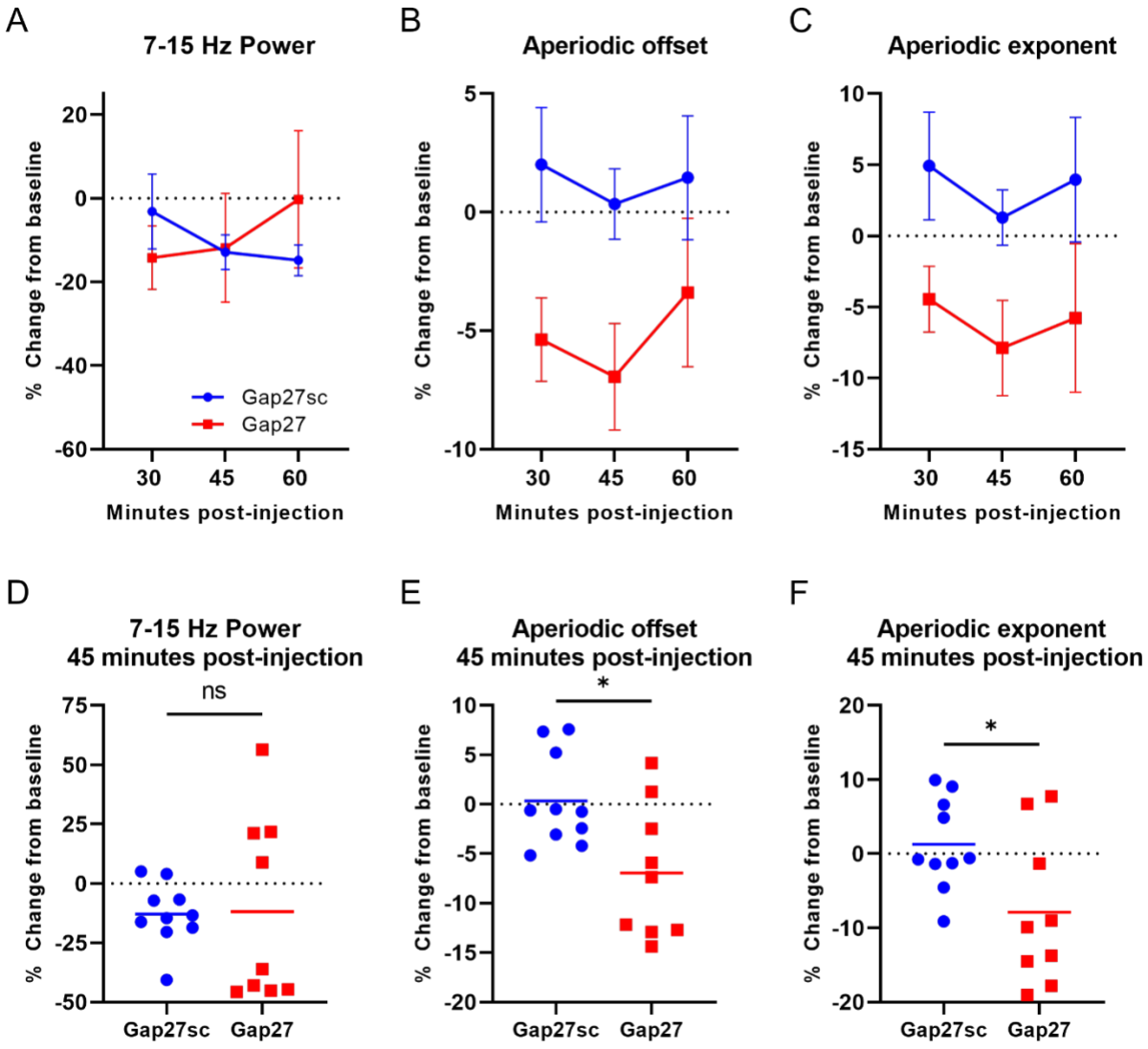

Figure 4.5 Effects of Gap27 on GPe local field potentials in MPTP-treated monkeys. (A) Percent change in 7-15 Hz power 30 minutes, 45 minutes, and 60 minutes following intracerebral injections of Gap27 or scrambled Gap27 peptide. (B) Change in aperiodic offset 30-60 minutes following drug injections. (C) Change in aperiodic exponent 30-60 minutes following drug injections. (D) Change in 7-15 Hz power 45 minutes following drug injection ($p=0.7802$, Mann-Whitney). (E) Change in aperiodic offset 45 minutes following drug injection ($p=0.022$, Mann-Whitney). (F) Change in aperiodic exponent 45 minutes following drug injection ($p=0.0435$, Mann-Whitney). For all panels, $N_{Gap27sc}=10$, $N_{Gap27}=9$ from 3 animals.

CHAPTER 5: Discussion

5.1 SUMMARY OF RESULTS

In the first study (Chapter 2), we identified core commonalities between mouse and rhesus macaque astrocytes. Prior investigations into both the morphology and functions of astrocytes in health and disease had been largely limited to rodents. But this remains a significant issue, since previous literature also suggested that primate astrocytes were more complex than rodent astrocytes (Oberheim et al., 2009, 2006). If this were the case, then fundamental differences in the form and function of astrocytes could have significant implications for the understanding of astrocytes in disease. Thus, to systematically compare astrocyte morphology between species, we used a multi-technique approach. Immunohistochemical examination of neuronal and astrocytic markers in several brain regions revealed that neuron densities were lower in monkeys compared to mice, while astrocyte densities were comparable between species. Neuronal densities were also variable by brain region in both species. Immunohistochemical examination of glial fibrillary acidic protein (GFAP) then revealed increased astrocyte territory area in monkeys, but comparable primary branch densities between species. Extending these findings, viral vector and diOlistic-mediated labeling of astrocytes revealed decreased neuropil infiltration volumes in monkeys. The decreased neuropil infiltration volume was partly due to thinner astrocyte processes, which was examined using electron microscopy. Hence it suggests that primate astrocytes do display a greater degree of overlap with neighboring astrocytes, and that they have slightly thinner processes. However, our work also demonstrates that astrocytes are remarkably similar across species, and that their astrocyte complexity scales with size to optimally cover the neuropil and allow them to perform their essential physiological roles.

The essential roles of astrocytes are perturbed across a host of neurodegenerative diseases and are often reflected in morphological changes. Therefore, as reported in Chapter 3, we

examined the potential effects of the MPTP parkinsonism model on astrocyte morphology in non-human primates. Using viral vector-mediated labeling of astrocytes in control and MPTP-treated parkinsonian monkeys, we found that astrocyte territory areas across in primary motor cortex and striatum were reduced in MPTP-treated monkeys. As GFAP expression is commonly increased across neurodegenerative diseases (Escartin et al., 2021), we also wondered if its expression was increased in brain regions affected in parkinsonism. We did not find a marked increase in GFAP in the primary motor cortex, striatum, or external globus pallidus (GPe) in contrast to previous studies (Charron et al., 2014). Since the GPe is astrocyte-enriched (as shown in Chapter 2) and displays astrocyte dysfunction in rodent models of parkinsonism (Chazalon et al., 2018; Cui et al., 2016), we further investigated MPTP-induced changes in GPe astrocytes. Increased expression of connexin-43 (cx-43) had been described in the globus pallidus of dopamine depleted rodents (Kawasaki et al., 2009; Wang et al., 2013), and thus we assessed if cx-43 expression increased in the GPe of our MPTP-treated monkeys. In contrast to previous studies, we did not find a significant increase in cx-43 expression compared to control monkeys.

Despite the lack of altered cx-43 expression between control and MPTP-treated monkeys, we wondered if the function of cx-43 was altered in the GPe of parkinsonian animals. Previous studies have noted increased neuronal synchronization and oscillatory activity in the GPe of parkinsonian animals (Hammond et al., 2007; Nini et al., 1995; Schwab et al., 2017), and studies in other brain regions have shown that astrocytes influence neuronal synchronization (Fellin et al., 2004; Szabó et al., 2017). Use of a non-specific gap junction blocker had successfully reduced pathological oscillatory activity in the GPe and improved motor function in dopamine depleted rodents (Phookan et al., 2015). Thus, we utilized a cx-43 selective blocker to investigate the role of astrocyte connexin-coupled networks to pathological neuronal activity in the MPTP-

treated monkey. Overall, we did not find any effects of cx-43 blockade on the firing rates or patterns of individual neurons in control or MPTP-treated monkeys. However, we did find an effect of cx-43 blockade on the aperiodic component of local field potentials (LFP) in MPTP-treated monkeys. The effect of cx-43 blockade further exacerbated the reduced aperiodic component found in MPTP-treated monkeys. The change in aperiodic components of LFPs could serve as potential biomarker for PD-related changes in brain activity. Changes in aperiodic components of the LFP have recently been described in dopamine depleted rodents (Kim et al., 2022) and PD patients (Wiest et al., 2023), but had not been previously assessed in non-human primates. The changes in the aperiodic component of the LFP in the GPe as well as increased cx-43 expression in astrocyte endfeet could indicate altered glio-vascular interactions following dopamine depletion.

5.2 CRITICAL ASSESSMENT OF METHODOLOGY

We have used a range of methods and analyses in this dissertation, but we would be remiss if we did not address the limitations of our approach. In this section, we take a critical look at the methodology in this dissertation and discuss the measures taken to address any limitations with consideration for future work.

5.2.1 Immunohistochemistry

First and foremost, immunohistochemistry relies on specificity of the antibodies used (Saper, 2005). We only used antibodies that were listed on the antibody registry and had been rigorously tested through the manufacturer. In addition, we simultaneously ran controls during our immunohistochemical reactions, such as endogenous tissue background controls and omission of primary antibody controls (Saper and Sawchenko, 2003). All antibodies used in this dissertation, except for NeuN, Aldh1L1, and S100β, have also been used for electron microscopy

studies in our labs. Thus, we were able to further validate the antibody's specificity for a given antigen based on the expected cellular subcellular localization.

Background labeling is another issue, particularly within primate tissues. This background can vary between individuals and even within an individual. Poor perfusion of the animal and remaining red blood cells can result in high levels of endogenous peroxidase and endogenous fluorescence in the brain tissue. This can be remedied to an extent by incubating sections in hydrogen peroxide to block endogenous peroxidases. While the quality of tissue is of primary importance, steps can also be taken during data acquisition to minimize the effects of background staining. For immunoperoxidase-based analyses (GFAP in control and MPTP-treated monkeys in Chapter 3) we addressed this by using image binarization for quantification. Using mean gray value assessments incorporates both specific staining and background staining into the quantification. By using a common binary threshold, across all sections, we were able to isolate staining from background, even when staining intensities varied from sample to sample. In fluorescent staining of primate tissues, background is often due to the accumulation of lipofuscin, a pigment which is increased in older animals and primates (Brizzee et al., 1975). To address background labeling in fluorescent analyses, we once again often utilized standard binarization and thresholding. In addition, for punctate stains such as vgat, we photobleached sections prior to staining to eliminate inter-individual variation in lipofuscin.

We also had to consider the depth of antibody penetration (and the resulting labeling of proteins of interest) within our tissue sections. As we typically use 50-60 µm thick sections in our lab, we often see decreased labeling in the middle of the tissue sections when examined under a fluorescent microscope. To avoid any confounds from this limitation, we restricted analysis to the superficial region of the tissue (10 µm thick z-stacks from the surface of the

section, where labeling was robust) for cell counts in Chapter 2. We additionally used 5.4 µm thick z-stacks from the surface for vgat staining and cx-43 staining. In addition, we increased detergent concentration and primary and secondary antibody incubation times for GFAP staining in 300 µm thick sections in Chapter 2. We found that these changes resulted in even staining throughout the thickness of the section.

Lastly, we had to consider the effects of tissue fixation. Strong fixation is required for adequate ultrastructural preservation of the tissue and electron microscope observation. Thus, we typically use 4% paraformaldehyde and 0.1% glutaraldehyde for perfusions, followed by a 24-hour immersion post-fixation in 4% paraformaldehyde. While this usually results in excellent preservation of the ultrastructure, it has the potential to mask antigen epitopes. To minimize this, we incubate sections in sodium borohydride prior to staining to reduce some of the free aldehydes and Schiff bases introduced during fixation (Heffernan et al., 2023). For tissue labeled with the diOlistic method, we found that transcardial perfusion with 4% paraformaldehyde and 0.1% glutaraldehyde prevented clear labeling of individual cells (Heffernan and Galvan, 2023). Thus, we decided to perfuse animals with Ringer's solution and use a brief immersion fixation with 4% paraformaldehyde, which remedied the issue.

5.2.2 Electrophysiology

The experiments described in Chapter 4 used injection of pharmacological compounds in the brain, with simultaneous recording of single neurons and local field potentials. Performing intracerebral drug injections during *in vivo* extracellular recordings in awake rhesus macaques is technically challenging. There are several factors that must be controlled and considered for reliable data acquisition and interpretation. First, each experiment required acute placement of the electrode in the desired area of interest, as the electrodes are not chronically implanted. This requires extensive knowledge of the recording chamber placement, brain atlas, and

electrophysiological characteristics of different brain regions (DeLong, 1973, 1971). Thus, we carried out several recording sessions in which we mapped the location of the brain structures within the recording chamber based on the expected atlas coordinates and electrophysiological properties. This is not perfect, though in the case of my project, the GPe has distinct firing properties which are easily discernible from the putamen (DeLong, 1973, 1971). During recordings, while sitting in a primate chair with heads restrained, our monkeys are awake and free to move their arms and legs. Animal movement can cause artifacts in the recording. However, once acclimated to recordings and sitting in the primate chair, most animals sit calmly with little movement. This is much preferred to using anesthetics, which has effects on neuronal activity (Magill et al., 2000). Even in the absence of anesthetics, neuronal activity in basal ganglia structures is affected by level of arousal, and thus we also monitored our monkeys by video to ensure that they are awake during active recording (Devergnas et al., 2014b; Gatev and Wichmann, 2009).

Pharmacological experiments *in vivo* can be affected by multiple aspects including specificity, time course, and diffusion of the drug under study. Although in rodent studies multiple pilot and control experiments are routinely performed to determine the optimal conditions, for practical and ethical reasons this is not possible in non-human primate experiments. Therefore, I conducted a thorough investigation of the available literature to guide my experiments. Specific to intracerebral drug injections during neuronal recordings, the drug's specificity and concentration are of paramount importance. Astrocytes are electrically silent, and thus the only way to currently measure astrocyte activity *in vivo* is through calcium imaging or other biosensors. Additionally, the functions of astrocyte gap junctions are reportedly broad, ranging from potassium buffering to metabolite exchange, and thus blockade of gap junctions

may affect other processes not reflected in calcium transients (Bazzigaluppi et al., 2017; Chever et al., 2016; Pannasch et al., 2011; Rouach et al., 2003). Therefore, a dose response curve for Gap27 has not been generated *in vivo*. Gap27 has been demonstrated to block dye transfer in brain slices and has induced changes in neuronal oscillatory activity *in vivo* at a similar concentration used in our studies (Bellot-Saez et al., 2018). Gap27 was also specific for cx-43 and not other connexins when tested *in vitro* (Wright et al., 2009). However, we cannot rule out the possibility that the concentration of the drug was too low to produce effects.

Other potential pitfalls include identifying the time course of a drug effect. For our experiments, the time window of drug effect course was determined based on effects seen at similar drug concentrations in previous studies, and by looking at all recordings and determining the timepoint with the average greatest difference from baseline activity. In previous studies, it was shown that blockade of cx-43 gap junctions began approximately 15 minutes following drug application *in vitro* and was sustained for over an hour (Boitano and Evans, 2000). At the concentration used in our studies (300 uM), blockade of cx-43 hemichannels occurs on the order of minutes *in vitro* (Wang et al., 2012). However, even with these considerations, it is possible that the time course of the compound in our experiments differed from previous studies.

We also cannot determine the area of drug diffusion with certainty. For intracerebral injections and individual neuron recordings, we used a small volume which is comparable to other studies (Bogenpohl et al., 2013). For intracerebral injections and local field potential recordings, we used a larger volume which could have spread to surrounding structures such as the putamen and internal globus pallidus. Thus, we cannot rule out that any effects seen in the local field potential recordings were driven by Gap27 diffusion into other brain regions.

5.2.3 MPTP-treated monkeys as a model for parkinsonism

We also must consider limitations of the model itself. While MPTP-treated monkeys display the cardinal motor symptoms of Parkinson's patients and pathologically replicate dopaminergic depletion along with other minor pathological changes seen in PD (Masilamoni and Smith, 2018), they do not have aggregated alpha-synuclein or Lewy bodies. Parkinson's disease in humans also results in the aggregation of alpha-synuclein (Braak et al., 2003; Stefanis, 2012). Alpha synuclein pathology in astrocytes and subsequent astrocyte reactivity have been reported in PD patients (Chou et al., 2021; Song et al., 2009). Thus, by using MPTP-treated monkeys, we may be missing an entire pathological component of the disease which is of high relevance to astrocytic function.

5.3 FUTURE DIRECTIONS

There are several future studies which could stem from this work. As we found changes in the aperiodic component of the local field potential in MPTP-treated monkeys, the potential of this change as a biomarker should be further investigated. Contributions of electrode characteristics, brain region, degree of arousal, degree of dopaminergic denervation, and severity of motor function should all be assessed in conjunction with local field potential recordings. The time course of changes to the aperiodic component are of particular interest, as they may precede clinical motor manifestations of the disease. If changes to the aperiodic component are detectable by electroencephalogram (EEG), it could provide a non-invasive and early diagnostic tool. An early diagnostic tool may be of great importance as motor symptoms typically present after a substantial proportion of dopaminergic neurons have been lost (Lang and Lozano, 1998; Marsden, 1990).

Another potential line of research could focus on identifying astrocyte-enriched genes that are differentially expressed in control and MPTP-treated monkeys. Using the list of morphologically-associated genes generated from mice (Endo et al., 2022), which was also used

in Chapter 2, one could then specifically target morphologically-associated genes that are dysregulated in MPTP-treated monkeys, and investigate if these genes contribute to the decreased astrocyte territory size we identified Chapter 3. A related set of studies could focus on the relationship between astrocyte territory size and synaptic density, as it is possible that the reduced territory size in MPTP-treated monkeys is a consequence of decreased synaptic density in those brain regions. Indeed, decreased density of glutamatergic synapses has been identified in the striatum of MPTP-treated monkeys, in parkinsonian rodents, and in PD patients (Ingham et al., 1989; Villalba and Smith, 2011; Zaja-Milatovic et al., 2005).

A separate study could investigate morphological changes of astrocytes in the substantia nigra pars compacta (SNc), the primary site of dopaminergic loss in PD patients and neurotoxin models of the disease, as well as the putamen, the primary receiving site of SNc-dopaminergic input, throughout the time course of dopaminergic cell death. Groups could include control monkeys, MPTP-treated pre-symptomatic monkeys, as well as monkeys with mild-to-moderate motor deficits. Methods used to assess astrocyte morphology in Chapters 2 and 3 could be used to assess timepoint-specific changes. A better understanding of astrocyte-related changes in disease progression could identify new therapeutic targets.

There is a wealth of astrocyte-focused studies that could be conducted now that we have validated several tools in the non-human primate to assess astrocyte morphology. While functional studies of astrocytes are always challenging, regardless of the model system, future studies could also take advantage of the astrocyte-specific promotor, GfaABC1D, to express opsins, DREADDS, or biosensors in astrocytes (Heffernan et al., 2022).

REFERENCES

Abbott, N.J., Patabendige, A.A.K., Dolman, D.E.M., Yusof, S.R., Begley, D.J., 2010. Structure and function of the blood–brain barrier. Neurobiol. Dis., Special Issue: Blood Brain Barrier 37, 13–25. https://doi.org/10.1016/j.nbd.2009.07.030

Abdi, A., Mallet, N., Mohamed, F.Y., Sharott, A., Dodson, P.D., Nakamura, K.C., Suri, S., Avery, S.V., Larvin, J.T., Garas, F.N., Garas, S.N., Vinciati, F., Morin, S., Bezard, E., Baufreton, J., Magill, P.J., 2015. Prototypic and arkypallidal neurons in the dopamine-intact external globus pallidus. J. Neurosci. Off. J. Soc. Neurosci. 35, 6667–6688. https://doi.org/10.1523/JNEUROSCI.4662-14.2015

Abecassis, Z.A., Berceau, B.L., Win, P.H., García, D., Xenias, H.S., Cui, Q., Pamukcu, A., Cherian, S., Hernández, V.M., Chon, U., Lim, B.K., Kim, Y., Justice, N.J., Awatramani, R., Hooks, B.M., Gerfen, C.R., Boca, S.M., Chan, C.S., 2020. Npas1+-Nkx2.1+ Neurons Are an Integral Part of the Cortico-pallido-cortical Loop. J. Neurosci. 40, 743–768. https://doi.org/10.1523/JNEUROSCI.1199-19.2019

Abudara, V., Bechberger, J., Freitas-Andrade, M., De Bock, M., Wang, N., Bultynck, G., Naus, C.C., Leybaert, L., Giaume, C., 2014. The connexin43 mimetic peptide Gap19 inhibits hemichannels without altering gap junctional communication in astrocytes. Front. Cell. Neurosci. 8, 306. https://doi.org/10.3389/fncel.2014.00306

Adamsky, A., Kol, A., Kreisel, T., Doron, A., Ozeri-Engelhard, N., Melcer, T., Refaeli, R., Horn, H., Regev, L., Groysman, M., London, M., Goshen, I., 2018. Astrocytic Activation Generates De Novo Neuronal Potentiation and Memory Enhancement. Cell 174, 59-71.e14. https://doi.org/10.1016/j.cell.2018.05.002

Allen, N.J., Eroglu, C., 2017. Cell Biology of Astrocyte-Synapse Interactions. Neuron 96, 697–708. https://doi.org/10.1016/j.neuron.2017.09.056

Allen, N.J., Lyons, D.A., 2018. Glia as Architects of Central Nervous System Formation and Function. Science 362, 181–185. https://doi.org/10.1126/science.aat0473

Andriezen, W., 1893. The neuroglia elements of the brain. Br Med J 2, 227–30.

Araque, A., Carmignoto, G., Haydon, P.G., Oliet, S.H.R., Robitaille, R., Volterra, A., 2014. Gliotransmitters Travel in Time and Space. Neuron 81, 728–739. https://doi.org/10.1016/j.neuron.2014.02.007

Araque, A., Parpura, V., Sanzgiri, R.P., Haydon, P.G., Araque, A., Parpura, V., Sanzgiri, R.P., Haydon, P.G., 1999. Tripartite synapses: glia, the unacknowledged partner. Trends Neurosci. 22, 208–215. https://doi.org/10.1016/S0166-2236(98)01349-6

Aristieta, A., Barresi, M., Azizpour Lindi, S., Barrière, G., Courtand, G., de la Crompe, B., Guilhemsang, L., Gauthier, S., Fioramonti, S., Baufreton, J., Mallet, N.P., 2021. A Disynaptic Circuit in the Globus Pallidus Controls Locomotion Inhibition. Curr. Biol. CB 31, 707-721.e7. https://doi.org/10.1016/j.cub.2020.11.019

Aten, S., Kiyoshi, C.M., Arzola, E.P., Patterson, J.A., Taylor, A.T., Du, Y., Guiher, A.M., Philip, M., Camacho, E.G., Mediratta, D., Collins, K., Boni, K., Garcia, S.A., Kumar, R., Drake, A.N., Hegazi, A., Trank, L., Benson, E., Kidd, G., Terman, D., Zhou, M., 2022. Ultrastructural view of astrocyte arborization, astrocyte-astrocyte and astrocyte-synapse contacts, intracellular vesicle-like structures, and mitochondrial network. Prog. Neurobiol. 213, 102264. https://doi.org/10.1016/j.pneurobio.2022.102264

Baldwin, K.T., Tan, C.X., Strader, S.T., Jiang, C., Savage, J.T., Elorza-Vidal, X., Contreras, X., Rülicke, T., Hippenmeyer, S., Estévez, R., Ji, R.-R., Eroglu, C., 2021. HepaCAM

controls astrocyte self-organization and coupling. Neuron 109, 2427-2442.e10. https://doi.org/10.1016/j.neuron.2021.05.025

Ballard, P.A., Tetrud, J.W., Langston, J.W., 1985. Permanent human parkinsonism due to 1-methy 1–4-phenyl-1,2,3,6-tetrahydropyridine (MPTP): Seven cases. Neurology 35, 949–949. https://doi.org/10.1212/WNL.35.7.949

Baranauskas, G., Maggiolini, E., Vato, A., Angotzi, G., Bonfanti, A., Zambra, G., Spinelli, A., Fadiga, L., 2012. Origins of 1/f2 scaling in the power spectrum of intracortical local field potential. J. Neurophysiol. 107, 984–994. https://doi.org/10.1152/jn.00470.2011

Bazzigaluppi, P., Weisspapir, I., Stefanovic, B., Leybaert, L., Carlen, P.L., 2017. Astrocytic gap junction blockade markedly increases extracellular potassium without causing seizures in the mouse neocortex. Neurobiol. Dis. 101, 1–7. https://doi.org/10.1016/j.nbd.2016.12.017

Bellot-Saez, A., Cohen, G., Schaik, A. van, Ooi, L., Morley, J.W., Buskila, Y., 2018. Astrocytic modulation of cortical oscillations. Sci. Rep. 8, 1–13. https://doi.org/10.1038/s41598-018-30003-w

Bennett, M.V.L., Contreras, J.E., Bukauskas, F.F., Sáez, J.C., 2003. New roles for astrocytes: Gap junction hemichannels have something to communicate. Trends Neurosci. 26, 610–617. https://doi.org/10.1016/j.tins.2003.09.008

Bernardinelli, Y., Randall, J., Janett, E., Nikonenko, I., König, S., Jones, E.V., Flores, C.E., Murai, K.K., Bochet, C.G., Holtmaat, A., Muller, D., 2014. Activity-Dependent Structural Plasticity of Perisynaptic Astrocytic Domains Promotes Excitatory Synapse Stability. Curr. Biol. 24, 1679–1688. https://doi.org/10.1016/j.cub.2014.06.025

Bevan, M.D., Magill, P.J., Terman, D., Bolam, J.P., Wilson, C.J., 2002. Move to the rhythm: oscillations in the subthalamic nucleus-external globus pallidus network. Trends Neurosci. 25, 525–531. https://doi.org/10.1016/s0166-2236(02)02235-x

Blumenfeld, H., 2010. Basal Ganglia, in: Neuroanatomy Through Clinical Cases. Sinauer Associates, Inc., Sunderland, MA, pp. 740–768.

Bogenpohl, J., Galvan, A., Hu, X., Wichmann, T., Smith, Y., 2013. Metabotropic glutamate receptor 4 in the basal ganglia of parkinsonian monkeys: Ultrastructural localization and electrophysiological effects of activation in the striatopallidal complex. Neuropharmacology 66, 242–252. https://doi.org/10.1016/j.neuropharm.2012.05.017

Boitano, S., Evans, W.H., 2000. Connexin mimetic peptides reversibly inhibit Ca2+signaling through gap junctions in airway cells. Am. J. Physiol.-Lung Cell. Mol. Physiol. 279, L623–L630. https://doi.org/10.1152/ajplung.2000.279.4.L623

Boulay, A.-C., Gilbert, A., Oliveira Moreira, V., Blugeon, C., Perrin, S., Pouch, J., Le Crom, S., Ducos, B., Cohen-Salmon, M., 2018. Connexin 43 Controls the Astrocyte Immunoregulatory Phenotype. Brain Sci. 8, 50. https://doi.org/10.3390/brainsci8040050

Braak, H., Tredici, K.D., Rüb, U., de Vos, R.A.I., Jansen Steur, E.N.H., Braak, E., 2003. Staging of brain pathology related to sporadic Parkinson's disease. Neurobiol. Aging 24, 197–211. https://doi.org/10.1016/S0197-4580(02)00065-9

Brizzee, K.R., Kaack, B., Klara, P., 1975. Lipofuscin: Intra- and Extraneuronal Accumulation and Regional Distribution, in: Ordy, J.M., Brizzee, K.R. (Eds.), Neurobiology of Aging: An Interdisciplinary Life-Span Approach, Advances in Behavioral Biology. Springer US, Boston, MA, pp. 463–484. https://doi.org/10.1007/978-1-4684-0925-3_20

Brown, P., Oliviero, A., Mazzone, P., Insola, A., Tonali, P., Lazzaro, V.D., 2001. Dopamine Dependency of Oscillations between Subthalamic Nucleus and Pallidum in Parkinson's Disease. J. Neurosci. 21, 1033–1038. https://doi.org/10.1523/JNEUROSCI.21-03-01033.2001

Burns, R.S., Markey, S.P., Phillips, J.M., Chiueh, C.C., 1984. The neurotoxicity of 1-methyl-4-phenyl-1,2,3,6-tetrahydropyridine in the monkey and man. Can. J. Neurol. Sci. J. Can. Sci. Neurol. 11, 166–168. https://doi.org/10.1017/s0317167100046345

Bushong, E.A., Martone, M.E., Jones, Y.Z., Ellisman, M.H., 2002. Protoplasmic Astrocytes in CA1 Stratum Radiatum Occupy Separate Anatomical Domains. J. Neurosci. 22, 183–192. https://doi.org/10.1523/JNEUROSCI.22-01-00183.2002

Caiola, M., Pittard, D., Wichmann, T., Galvan, A., 2019. Quantification of movement in normal and parkinsonian macaques using video analysis. J. Neurosci. Methods 322, 96–102. https://doi.org/10.1016/j.jneumeth.2019.05.001

Cajal, S., 1913. Un nuevo proceder para la impregnación de la neuroglía. Bol. Soc. Esp. Bio. 104–108.

Chai, H., Diaz-Castro, B., Shigetomi, E., Monte, E., Octeau, J.C., Yu, X., Cohn, W., Rajendran, P.S., Vondriska, T.M., Whitelegge, J.P., Coppola, G., Khakh, B.S., 2017. Neural Circuit-Specialized Astrocytes: Transcriptomic, Proteomic, Morphological, and Functional Evidence. Neuron 95, 531-549.e9. https://doi.org/10.1016/j.neuron.2017.06.029

Charron, G., Doudnikoff, E., Canron, M.-H., Li, Q., Véga, C., Marais, S., Baufreton, J., Vital, A., Oliet, S.H.R., Bezard, E., 2014. Astrocytosis in parkinsonism: considering tripartite striatal synapses in physiopathology? Front. Aging Neurosci. 6. https://doi.org/10.3389/fnagi.2014.00258

Chazalon, M., Paredes-Rodriguez, E., Morin, S., Martinez, A., Cristóvão-Ferreira, S., Vaz, S., Sebastiao, A., Panatier, A., Boué-Grabot, E., Miguelez, C., Baufreton, J., 2018. GAT-3 Dysfunction Generates Tonic Inhibition in External Globus Pallidus Neurons in Parkinsonian Rodents. Cell Rep. 23, 1678–1690. https://doi.org/10.1016/j.celrep.2018.04.014

Cheung, G., Bataveljic, D., Visser, J., Kumar, N., Moulard, J., Dallérac, G., Mozheiko, D., Rollenhagen, A., Ezan, P., Mongin, C., Chever, O., Bemelmans, A.-P., Lübke, J., Leray, I., Rouach, N., 2022. Physiological synaptic activity and recognition memory require astroglial glutamine. Nat. Commun. 13, 753. https://doi.org/10.1038/s41467-022-28331-7

Chever, O., Dossi, E., Pannasch, U., Derangeon, M., Rouach, N., 2016. Astroglial networks promote neuronal coordination. Sci. Signal. 9, ra6–ra6. https://doi.org/10.1126/scisignal.aad3066

Chever, O., Lee, C.-Y., Rouach, N., 2014. Astroglial connexin43 hemichannels tune basal excitatory synaptic transmission. J. Neurosci. Off. J. Soc. Neurosci. 34, 11228–11232. https://doi.org/10.1523/JNEUROSCI.0015-14.2014

Chou, T.-W., Chang, N.P., Krishnagiri, M., Patel, A.P., Lindman, M., Angel, J.P., Kung, P.-L., Atkins, C., Daniels, B.P., 2021. Fibrillar α-synuclein induces neurotoxic astrocyte activation via RIP kinase signaling and NF-κB. Cell Death Dis. 12, 756. https://doi.org/10.1038/s41419-021-04049-0

Cibelli, A., Stout, R., Timmermann, A., de Menezes, L., Guo, P., Maass, K., Seifert, G., Steinhäuser, C., Spray, D.C., Scemes, E., 2021. Cx43 carboxyl terminal domain determines AQP4 and Cx30 endfoot organization and blood brain barrier permeability. Sci. Rep. 11, 24334. https://doi.org/10.1038/s41598-021-03694-x

Colombo, J.A., Yáñez, A., Puissant, V., Lipina, S., 1995. Long, interlaminar astroglial cell processes in the cortex of adult monkeys. J. Neurosci. Res. 40, 551–556. https://doi.org/10.1002/jnr.490400414

Crompe, B. de la, Aristieta, A., Leblois, A., Elsherbiny, S., Boraud, T., Mallet, N.P., 2020. The globus pallidus orchestrates abnormal network dynamics in a model of Parkinsonism. Nat. Commun. 11, 1570. https://doi.org/10.1038/s41467-020-15352-3

Cui, Q., Du, X., Chang, I.Y.M., Pamukcu, A., Lilascharoen, V., Berceau, B.L., García, D., Hong, D., Chon, U., Narayanan, A., Kim, Y., Lim, B.K., Chan, C.S., 2021. Striatal Direct Pathway Targets Npas1+ Pallidal Neurons. J. Neurosci. Off. J. Soc. Neurosci. 41, 3966–3987. https://doi.org/10.1523/JNEUROSCI.2306-20.2021

Cui, Q., Pitt, J.E., Pamukcu, A., Poulin, J.-F., Mabrouk, O.S., Fiske, M.P., Fan, I.B., Augustine, E.C., Young, K.A., Kennedy, R.T., Awatramani, R., Chan, C.S., 2016. Blunted mGluR Activation Disinhibits Striatopallidal Transmission in Parkinsonian Mice. Cell Rep. 17, 2431–2444. https://doi.org/10.1016/j.celrep.2016.10.087

Decrock, E., De Vuyst, E., Vinken, M., Van Moorhem, M., Vranckx, K., Wang, N., Van Laeken, L., De Bock, M., D'Herde, K., Lai, C.P., Rogiers, V., Evans, W.H., Naus, C.C., Leybaert, L., 2009. Connexin 43 hemichannels contribute to the propagation of apoptotic cell death in a rat C6 glioma cell model. Cell Death Differ. 16, 151–163. https://doi.org/10.1038/cdd.2008.138

DeFelipe, J., Alonso-Nanclares, L., Arellano, J.I., 2002. Microstructure of the neocortex: Comparative aspects. J. Neurocytol. 31, 299–316.

DeLong, M.R., 1973. Putamen: activity of single units during slow and rapid arm movements. Science 179, 1240–1242. https://doi.org/10.1126/science.179.4079.1240

DeLong, M.R., 1971. Activity of pallidal neurons during movement. J. Neurophysiol. 34, 414–427. https://doi.org/10.1152/jn.1971.34.3.414

Devergnas, A., Pittard, D., Bliwise, D., Wichmann, T., 2014a. Relationship between oscillatory activity in the cortico-basal ganglia network and parkinsonism in MPTP-treated monkeys. Neurobiol. Dis. 68, 156–166. https://doi.org/10.1016/j.nbd.2014.04.004

Devergnas, A., Pittard, D., Bliwise, D., Wichmann, T., 2014b. Relationship between oscillatory activity in the cortico-basal ganglia network and parkinsonism in MPTP-treated monkeys. Neurobiol. Dis. 68, 156–166. https://doi.org/10.1016/j.nbd.2014.04.004

Donoghue, T., Haller, M., Peterson, E.J., Varma, P., Sebastian, P., Gao, R., Noto, T., Lara, A.H., Wallis, J.D., Knight, R.T., Shestyuk, A., Voytek, B., 2020. Parameterizing neural power spectra into periodic and aperiodic components. Nat. Neurosci. 23, 1655–1665. https://doi.org/10.1038/s41593-020-00744-x

Du, J., Yi, M., Zhou, F., He, W., Yang, A., Qiu, M., Huang, H., 2021. S100B is selectively expressed by gray matter protoplasmic astrocytes and myelinating oligodendrocytes in the developing CNS. Mol. Brain 14, 154. https://doi.org/10.1186/s13041-021-00865-9

Durkee, C.A., Covelo, A., Lines, J., Kofuji, P., Aguilar, J., Araque, A., 2019. Gi/o PROTEIN-COUPLED RECEPTORS INHIBIT NEURONS BUT ACTIVATE ASTROCYTES AND STIMULATE GLIOTRANSMISSION. Glia 67, 1076–1093. https://doi.org/10.1002/glia.23589

EbrahimAmini, A., Bazzigaluppi, P., Aquilino, M.S., Stefanovic, B., Carlen, P.L., 2021. Neocortical in vivo focal and spreading potassium responses and the influence of astrocytic gap junctional coupling. Neurobiol. Dis. 147, 105160. https://doi.org/10.1016/j.nbd.2020.105160

Ede, F. van, Quinn, A.J., Woolrich, M.W., Nobre, A.C., 2018. Neural Oscillations: Sustained Rhythms or Transient Burst-Events? Trends Neurosci. 41, 415–417. https://doi.org/10.1016/j.tins.2018.04.004

Elias, S., Ritov, Y., Bergman, H., 2008. Balance of Increases and Decreases in Firing Rate of the Spontaneous Activity of Basal Ganglia High-Frequency Discharge Neurons. J. Neurophysiol. 100, 3086–3104. https://doi.org/10.1152/jn.90714.2008

Emborg, M.E., 2007. Nonhuman Primate Models of Parkinson's Disease. ILAR J. 48, 339–355. https://doi.org/10.1093/ilar.48.4.339

Endo, F., Kasai, A., Soto, J.S., Yu, X., Qu, Z., Hashimoto, H., Gradinaru, V., Kawaguchi, R., Khakh, B.S., 2022. Molecular basis of astrocyte diversity and morphology across the CNS in health and disease. Science 378, eadc9020. https://doi.org/10.1126/science.adc9020

Eng, L.F., Vanderhaeghen, J.J., Bignami, A., Gerstl, B., 1971. An acidic protein isolated from fibrous astrocytes. Brain Res. 28, 351–354. https://doi.org/10.1016/0006-8993(71)90668-8

Engel, A.K., Fries, P., 2010. Beta-band oscillations—signalling the status quo? Curr. Opin. Neurobiol., Cognitive neuroscience 20, 156–165. https://doi.org/10.1016/j.conb.2010.02.015

Escartin, C., Galea, E., Lakatos, A., O'Callaghan, J.P., Petzold, G.C., Serrano-Pozo, A., Steinhäuser, C., Volterra, A., Carmignoto, G., Agarwal, A., Allen, N.J., Araque, A., Barbeito, L., Barzilai, A., Bergles, D.E., Bonvento, G., Butt, A.M., Chen, W.-T., Cohen-Salmon, M., Cunningham, C., Deneen, B., De Strooper, B., Díaz-Castro, B., Farina, C., Freeman, M., Gallo, V., Goldman, J.E., Goldman, S.A., Götz, M., Gutiérrez, A., Haydon,

P.G., Heiland, D.H., Hol, E.M., Holt, M.G., Iino, M., Kastanenka, K.V., Kettenmann, H., Khakh, B.S., Koizumi, S., Lee, C.J., Liddelow, S.A., MacVicar, B.A., Magistretti, P., Messing, A., Mishra, A., Molofsky, A.V., Murai, K.K., Norris, C.M., Okada, S., Oliet, S.H.R., Oliveira, J.F., Panatier, A., Parpura, V., Pekna, M., Pekny, M., Pellerin, L., Perea, G., Pérez-Nievas, B.G., Pfrieger, F.W., Poskanzer, K.E., Quintana, F.J., Ransohoff, R.M., Riquelme-Perez, M., Robel, S., Rose, C.R., Rothstein, J.D., Rouach, N., Rowitch, D.H., Semyanov, A., Sirko, S., Sontheimer, H., Swanson, R.A., Vitorica, J., Wanner, I.-B., Wood, L.B., Wu, J., Zheng, B., Zimmer, E.R., Zorec, R., Sofroniew, M.V., Verkhratsky, A., 2021. Reactive astrocyte nomenclature, definitions, and future directions. Nat. Neurosci. 24, 312–325. https://doi.org/10.1038/s41593-020-00783-4

Ezan, P., André, P., Cisternino, S., Saubaméa, B., Boulay, A.-C., Doutremer, S., Thomas, M.-A., Quenech'du, N., Giaume, C., Cohen-Salmon, M., 2012. Deletion of Astroglial Connexins Weakens the Blood–Brain Barrier. J. Cereb. Blood Flow Metab. 32, 1457–1467. https://doi.org/10.1038/jcbfm.2012.45

Falcone, C., McBride, E.L., Hopkins, W.D., Hof, P.R., Manger, P.R., Sherwood, C.C., Noctor, S.C., Martinez-Cerdeno, V., 2021a. Redefining varicose projection astrocytes in primates. Glia 70, 145–154. https://doi.org/10.1002/glia.24093

Falcone, C., Penna, E., Hong, T., Tarantal, A.F., Hof, P.R., Hopkins, W.D., Sherwood, C.C., Noctor, S.C., Martínez-Cerdeño, V., 2021b. Cortical Interlaminar Astrocytes Are Generated Prenatally, Mature Postnatally, and Express Unique Markers in Human and Nonhuman Primates. Cereb. Cortex 31, 379–395. https://doi.org/10.1093/cercor/bhaa231

Falcone, C., Wolf-Ochoa, M., Amina, S., Hong, T., Vakilzadeh, G., Hopkins, W.D., Hof, P.R., Sherwood, C.C., Manger, P.R., Noctor, S.C., Martínez-Cerdeño, V., 2019. Cortical

interlaminar astrocytes across the therian mammal radiation. J. Comp. Neurol. 527, 1654–1674. https://doi.org/10.1002/cne.24605

Fan, K.Y., Baufreton, J., Surmeier, D.J., Chan, C.S., Bevan, M.D., 2012. Proliferation of external globus pallidus-subthalamic nucleus synapses following degeneration of midbrain dopamine neurons. J. Neurosci. Off. J. Soc. Neurosci. 32, 13718–13728. https://doi.org/10.1523/JNEUROSCI.5750-11.2012

Fellin, T., Pascual, O., Gobbo, S., Pozzan, T., Haydon, P.G., Carmignoto, G., 2004. Neuronal Synchrony Mediated by Astrocytic Glutamate through Activation of Extrasynaptic NMDA Receptors. Neuron 43, 729–743. https://doi.org/10.1016/j.neuron.2004.08.011

Galvan, A., Devergnas, A., Wichmann, T., 2015a. Alterations in neuronal activity in basal ganglia-thalamocortical circuits in the parkinsonian state. Front. Neuroanat. 9. https://doi.org/10.3389/fnana.2015.00005

Galvan, A., Devergnas, A., Wichmann, T., 2015b. Alterations in neuronal activity in basal ganglia-thalamocortical circuits in the parkinsonian state. Front. Neuroanat. 9, 5. https://doi.org/10.3389/fnana.2015.00005

Galvan, A., Hu, X., Rommelfanger, K.S., Pare, J.-F., Khan, Z.U., Smith, Y., Wichmann, T., 2014. Localization and function of dopamine receptors in the subthalamic nucleus of normal and parkinsonian monkeys. J. Neurophysiol. 112, 467–479. https://doi.org/10.1152/jn.00849.2013

Galvan, A., Hu, X., Smith, Y., Wichmann, T., 2011. Localization and pharmacological modulation of GABA-B receptors in the globus pallidus of parkinsonian monkeys. Exp. Neurol. 229, 429–439. https://doi.org/10.1016/j.expneurol.2011.03.010

Galvan, A., Hu, X., Smith, Y., Wichmann, T., 2010. Localization and function of GABA transporters in the globus pallidus of parkinsonian monkeys. Exp. Neurol. 223, 505–515. https://doi.org/10.1016/j.expneurol.2010.01.018

Galvan, A., Kuwajima, M., Smith, Y., 2006. Glutamate and GABA receptors and transporters in the basal ganglia: What does their subsynaptic localization reveal about their function? Neuroscience 143, 351–375. https://doi.org/10.1016/j.neuroscience.2006.09.019

Galvan, A., Stauffer, W.R., Acker, L., El-Shamayleh, Y., Inoue, K., Ohayon, S., Schmid, M.C., 2017. Nonhuman Primate Optogenetics: Recent Advances and Future Directions. J. Neurosci. 37, 10894–10903. https://doi.org/10.1523/JNEUROSCI.1839-17.2017

Galvan, A., Villalba, R.M., West, S.M., Maidment, N.T., Ackerson, L.C., Smith, Y., Wichmann, T., 2005. GABAergic modulation of the activity of globus pallidus neurons in primates: in vivo analysis of the functions of GABA receptors and GABA transporters. J. Neurophysiol. 94, 990–1000. https://doi.org/10.1152/jn.00068.2005

Gan, W.-B., Grutzendler, J., Wong, W.T., Wong, R.O.L., Lichtman, J.W., 2000. Multicolor "DiOlistic" Labeling of the Nervous System Using Lipophilic Dye Combinations. Neuron 27, 219–225. https://doi.org/10.1016/S0896-6273(00)00031-3

Gao, R., Peterson, E.J., Voytek, B., 2017. Inferring synaptic excitation/inhibition balance from field potentials. NeuroImage 158, 70–78. https://doi.org/10.1016/j.neuroimage.2017.06.078

Gatev, P., Wichmann, T., 2009. Interactions between cortical rhythms and spiking activity of single basal ganglia neurons in the normal and parkinsonian state. Cereb. Cortex N. Y. N 1991 19, 1330–1344. https://doi.org/10.1093/cercor/bhn171

Golgi, C., 1873. Sulla struttura della sostanza grigia della cervello. Gazz Med Ital Lomb. 6, 244–246.

Gull, S., Ingrisch, I., Tausch, S., Witte, O.W., Schmidt, S., 2015. Consistent and reproducible staining of glia by a modified Golgi–Cox method. J. Neurosci. Methods 256, 141–150. https://doi.org/10.1016/j.jneumeth.2015.08.029

Haber, M., Zhou, L., Murai, K.K., 2006. Cooperative Astrocyte and Dendritic Spine Dynamics at Hippocampal Excitatory Synapses. J. Neurosci. 26, 8881–8891. https://doi.org/10.1523/JNEUROSCI.1302-06.2006

Hammond, C., Bergman, H., Brown, P., 2007. Pathological synchronization in Parkinson's disease: networks, models and treatments. Trends Neurosci. 30, 357–364. https://doi.org/10.1016/j.tins.2007.05.004

Han, X., Chen, M., Wang, F., Windrem, M., Wang, S., Shanz, S., Xu, Q., Oberheim, N.A., Bekar, L., Betstadt, S., Silva, A.J., Takano, T., Goldman, S.A., Nedergaard, M., 2013. Forebrain engraftment by human glial progenitor cells enhances synaptic plasticity and learning in adult mice. Cell Stem Cell 12, 342–353. https://doi.org/10.1016/j.stem.2012.12.015

Harris, A.L., 2007. Connexin Channel Permeability to Cytoplasmic Molecules. Prog. Biophys. Mol. Biol. 94, 120–143. https://doi.org/10.1016/j.pbiomolbio.2007.03.011

He, J., Kleyman, M., Chen, J., Alikaya, A., Rothenhoefer, K.M., Ozturk, B.E., Wirthlin, M., Bostan, A.C., Fish, K., Byrne, L.C., Pfenning, A.R., Stauffer, W.R., 2021. Transcriptional and Anatomical Diversity of Medium Spiny Neurons in the Primate Striatum. Curr. Biol. CB 31, 5473-5486.e6. https://doi.org/10.1016/j.cub.2021.10.015

Heffernan, K.S., Galvan, A., 2023. Building and Characterization of an Affordable diOlistic Device for Single-Cell Labeling in Rodent and Non-Human Primate Brain Slices. Curr. Protoc. 3, e760. https://doi.org/10.1002/cpz1.760

Heffernan, K.S., Rahman, K., Smith, Y., Galvan, A., 2022. Characterization of the GfaABC1D promoter to selectively target astrocytes in the rhesus macaque brain. J. Neurosci. Methods 372, 109530. https://doi.org/10.1016/j.jneumeth.2022.109530

Heffernan, K.S., Smith, Y., Galvan, A., 2023. Reporter Selection and Postmortem Methods to Verify Transgene Expression, in: Eldridge, M.A.G., Galvan, A. (Eds.), Vectorology for Optogenetics and Chemogenetics, Neuromethods. Springer US, New York, NY, pp. 275–292. https://doi.org/10.1007/978-1-0716-2918-5_15

Hegeman, D.J., Hong, E.S., Hernández, V.M., Chan, C.S., 2016. The External Globus Pallidus: Progress and Perspectives. Eur. J. Neurosci. 43, 1239–1265. https://doi.org/10.1111/ejn.13196

Heikkila, R.E., Manzino, L., Cabbat, F.S., Duvoisin, R.C., 1984. Protection against the dopaminergic neurotoxicity of 1-methyl-4-phenyl-1,2,5,6-tetrahydropyridine by monoamine oxidase inhibitors. Nature 311, 467–469. https://doi.org/10.1038/311467a0

Henning, J., Strauss, U., Wree, A., Gimsa, J., Rolfs, A., Benecke, R., Gimsa, U., 2008. Differential astroglial activation in 6-hydroxydopamine models of Parkinson's disease. Neurosci. Res. 62, 246–253. https://doi.org/10.1016/j.neures.2008.09.001

Hösli, L., Binini, N., Ferrari, K.D., Thieren, L., Looser, Z.J., Zuend, M., Zanker, H.S., Berry, S., Holub, M., Möbius, W., Ruhwedel, T., Nave, K.-A., Giaume, C., Weber, B., Saab, A.S., 2022a. Decoupling astrocytes in adult mice impairs synaptic plasticity and spatial learning. Cell Rep. 38, 110484. https://doi.org/10.1016/j.celrep.2022.110484

Hösli, L., Zuend, M., Bredell, G., Zanker, H.S., Porto De Oliveira, C.E., Saab, A.S., Weber, B., 2022b. Direct vascular contact is a hallmark of cerebral astrocytes. Cell Rep. 39, 110599. https://doi.org/10.1016/j.celrep.2022.110599

Hutchison, W.D., Lozano, A.M., Davis, K.D., Saint-Cyr, J.A., Lang, A.E., Dostrovsky, J.O., 1994. Differential neuronal activity in segments of globus pallidus in Parkinson's disease patients. Neuroreport 5, 1533–1537.

Ingham, C.A., Hood, S.H., Arbuthnott, G.W., 1989. Spine density on neostriatal neurones changes with 6-hydroxydopamine lesions and with age. Brain Res. 503, 334–338. https://doi.org/10.1016/0006-8993(89)91686-7

Itoh, Y., Voskuhl, R., 2017. Cell specificity dictates similarities in gene expression in multiple sclerosis, Parkinson's disease, and Alzheimer's disease. PloS One 12. https://doi.org/doi:10.1371/journal.pone.0181349

Izpisua Belmonte, J.C., Callaway, E.M., Caddick, S.J., Churchland, P., Feng, G., Homanics, G.E., Lee, K.-F., Leopold, D.A., Miller, C.T., Mitchell, J.F., Mitalipov, S., Moutri, A.R., Movshon, J.A., Okano, H., Reynolds, J.H., Ringach, D., Sejnowski, T.J., Silva, A.C., Strick, P.L., Wu, J., Zhang, F., 2015. Brains, genes, and primates. Neuron 86, 617–631. https://doi.org/10.1016/j.neuron.2015.03.021

Jenkinson, N., Brown, P., 2011. New insights into the relationship between dopamine, beta oscillations and motor function. Trends Neurosci. 34, 611–618. https://doi.org/10.1016/j.tins.2011.09.003

Joshua, M., Elias, S., Levine, O., Bergman, H., 2007. Quantifying the isolation quality of extracellularly recorded action potentials. J. Neurosci. Methods 163, 267–282. https://doi.org/10.1016/j.jneumeth.2007.03.012

Jurga, A.M., Paleczna, M., Kadluczka, J., Kuter, K.Z., 2021. Beyond the GFAP-Astrocyte Protein Markers in the Brain. Biomolecules 11, 1361. https://doi.org/10.3390/biom11091361

Katabi, S., Adler, A., Deffains, M., Bergman, H., 2023. Dichotomous activity and function of neurons with low- and high-frequency discharge in the external globus pallidus of non-human primates. Cell Rep. 42, 111898. https://doi.org/10.1016/j.celrep.2022.111898

Kater, M.S.J., Badia-Soteras, A., van Weering, J.R.T., Smit, A.B., Verheijen, M.H.G., 2023. Electron microscopy analysis of astrocyte-synapse interactions shows altered dynamics in an Alzheimer's disease mouse model. Front. Cell. Neurosci. 17, 1085690. https://doi.org/10.3389/fncel.2023.1085690

Kawasaki, A., Hayashi, T., Nakachi, K., Trosko, J.E., Sugihara, K., Kotake, Y., Ohta, S., 2009. Modulation of connexin 43 in rotenone-induced model of Parkinson's disease. Neuroscience 160, 61–68. https://doi.org/10.1016/j.neuroscience.2009.01.080

Ketzef, M., Silberberg, G., 2021. Differential Synaptic Input to External Globus Pallidus Neuronal Subpopulations In Vivo. Neuron 109, 516-529.e4. https://doi.org/10.1016/j.neuron.2020.11.006

Kim, J., Lee, J., Kim, E., Choi, J.H., Rah, J.-C., Choi, J.-W., 2022. Dopamine depletion can be predicted by the aperiodic component of subthalamic local field potentials. Neurobiol. Dis. 168, 105692. https://doi.org/10.1016/j.nbd.2022.105692

Kliem, M.A., Wichmann, T., 2004. A method to record changes in local neuronal discharge in response to infusion of small drug quantities in awake monkeys. J. Neurosci. Methods 138, 45–49. https://doi.org/10.1016/j.jneumeth.2004.03.015

Knox, E.G., Aburto, M.R., Clarke, G., Cryan, J.F., O'Driscoll, C.M., 2022. The blood-brain barrier in aging and neurodegeneration. Mol. Psychiatry 27, 2659–2673. https://doi.org/10.1038/s41380-022-01511-z

Korogod, N., Petersen, C.C., Knott, G.W., 2015. Ultrastructural analysis of adult mouse neocortex comparing aldehyde perfusion with cryo fixation. eLife 4, e05793. https://doi.org/10.7554/eLife.05793

Kovaleski, R.F., Callahan, J.W., Chazalon, M., Wokosin, D.L., Baufreton, J., Bevan, M.D., 2020. Dysregulation of external globus pallidus-subthalamic nucleus network dynamics in parkinsonian mice during cortical slow-wave activity and activation. J. Physiol. 598, 1897–1927. https://doi.org/10.1113/JP279232

Krienen, F.M., Goldman, M., Zhang, Q., del Rosario, R.C.H., Florio, M., Machold, R., Saunders, A., Levandowski, K., Zaniewski, H., Schuman, B., Wu, C., Lutservitz, A., Mullally, C.D., Reed, N., Bien, E., Bortolin, L., Fernandez-Otero, M., Lin, J.D., Wysoker, A., Nemesh, J., Kulp, D., Burns, M., Tkachev, V., Smith, R., Walsh, C.A., Dimidschstein, J., Rudy, B., Kean, L.S., Berretta, S., Fishell, G., Feng, G., McCarroll, S.A., 2020. Innovations present in the primate interneuron repertoire. Nature 586, 262–269. https://doi.org/10.1038/s41586-020-2781-z

Lagos-Cabré, R., Alvarez, A., Kong, M., Burgos-Bravo, F., Cárdenas, A., Rojas-Mancilla, E., Pérez-Nuñez, R., Herrera-Molina, R., Rojas, F., Schneider, P., Herrera-Marschitz, M., Quest, A.F.G., van Zundert, B., Leyton, L., 2017. αVβ3 Integrin regulates astrocyte reactivity. J. Neuroinflammation 14, 194. https://doi.org/10.1186/s12974-017-0968-5

Langston, J.W., 2017. The MPTP Story. J. Park. Dis. 7, S11–S19. https://doi.org/10.3233/JPD-179006

Langston, J.W., Irwin, I., Langston, E.B., Forno, L.S., 1984a. 1-Methyl-4-phenylpyridinium ion (MPP+): identification of a metabolite of MPTP, a toxin selective to the substantia nigra. Neurosci. Lett. 48, 87–92. https://doi.org/10.1016/0304-3940(84)90293-3

Langston, J.W., Langston, E.B., Irwin, I., 1984b. MPTP-induced parkinsonism in human and non-human primates--clinical and experimental aspects. Acta Neurol. Scand. Suppl. 100, 49–54.

LEE, J., ZIERING, A., HEINEMAN, S.D., BERGER, L., 1947. PIPERIDINE DERIVATIVES. PART II. 2-PHENYL- AND 2-PHENYLALKYL-PIPERIDINES1. J. Org. Chem. 12, 885–893. https://doi.org/10.1021/jo01170a021

Lee, Y., Messing, A., Su, M., Brenner, M., 2008. GFAP promoter elements required for region-specific and astrocyte-specific expression. Glia 56, 481–493. https://doi.org/10.1002/glia.20622

Legéndy, C.R., Salcman, M., 1985. Bursts and recurrences of bursts in the spike trains of spontaneously active striate cortex neurons. J. Neurophysiol. 53, 926–939. https://doi.org/10.1152/jn.1985.53.4.926

Leybaert, L., Lampe, P.D., Dhein, S., Kwak, B.R., Ferdinandy, P., Beyer, E.C., Laird, D.W., Naus, C.C., Green, C.R., Schulz, R., 2017. Connexins in Cardiovascular and Neurovascular Health and Disease: Pharmacological Implications. Pharmacol. Rev. 69, 396–478. https://doi.org/10.1124/pr.115.012062

Li, J., Pan, L., Pembroke, W.G., Rexach, J.E., Godoy, M.I., Condro, M.C., Alvarado, A.G., Harteni, M., Chen, Y.-W., Stiles, L., Chen, A.Y., Wanner, I.B., Yang, X., Goldman, S.A., Geschwind, D.H., Kornblum, H.I., Zhang, Y., 2021. Conservation and divergence of

vulnerability and responses to stressors between human and mouse astrocytes. Nat. Commun. 12, 3958. https://doi.org/10.1038/s41467-021-24232-3

Lushnikova, I., Skibo, G., Muller, D., Nikonenko, I., 2009. Synaptic potentiation induces increased glial coverage of excitatory synapses in CA1 hippocampus. Hippocampus 19, 753–762. https://doi.org/10.1002/hipo.20551

Magill, P.J., Bolam, J.P., Bevan, M.D., 2000. Relationship of Activity in the Subthalamic Nucleus–Globus Pallidus Network to Cortical Electroencephalogram. J. Neurosci. 20, 820–833. https://doi.org/10.1523/JNEUROSCI.20-02-00820.2000

Mallet, N., Micklem, B.R., Henny, P., Brown, M.T., Williams, C., Bolam, J.P., Nakamura, K.C., Magill, P.J., 2012. Dichotomous Organization of the External Globus Pallidus. Neuron 74, 1075–1086. https://doi.org/10.1016/j.neuron.2012.04.027

Manjarrez-Marmolejo, J., Franco-Pérez, J., 2016. Gap Junction Blockers: An Overview of their Effects on Induced Seizures in Animal Models. Curr. Neuropharmacol. 14, 759–771. https://doi.org/10.2174/1570159X14666160603115942

Masilamoni, G.J., Smith, Y., 2018. Chronic MPTP administration regimen in monkeys: a model of dopaminergic and non-dopaminergic cell loss in Parkinson's disease. J. Neural Transm. Vienna Austria 1996 125, 337–363. https://doi.org/10.1007/s00702-017-1774-z

Mastro, K.J., Bouchard, R.S., Holt, H.A.K., Gittis, A.H., 2014. Transgenic Mouse Lines Subdivide External Segment of the Globus Pallidus (GPe) Neurons and Reveal Distinct GPe Output Pathways. J. Neurosci. 34, 2087–2099. https://doi.org/10.1523/JNEUROSCI.4646-13.2014

Mastro, K.J., Zitelli, K.T., Willard, A.M., Leblanc, K.H., Kravitz, A.V., Gittis, A.H., 2017. Cell-specific pallidal intervention induces long-lasting motor recovery in dopamine-depleted mice. Nat. Neurosci. 20, 815–823. https://doi.org/10.1038/nn.4559

Mathiisen, T.M., Lehre, K.P., Danbolt, N.C., Ottersen, O.P., 2010. The perivascular astroglial sheath provides a complete covering of the brain microvessels: an electron microscopic 3D reconstruction. Glia 58, 1094–1103. https://doi.org/10.1002/glia.20990

Mazaud, D., Capano, A., Rouach, N., 2021. The many ways astroglial connexins regulate neurotransmission and behavior. Glia 69, 2527–2545. https://doi.org/10.1002/glia.24040

McCarthy, M.M., Moore-Kochlacs, C., Gu, X., Boyden, E.S., Han, X., Kopell, N., 2011. Striatal origin of the pathologic beta oscillations in Parkinson's disease. Proc. Natl. Acad. Sci. U. S. A. 108, 11620–11625. https://doi.org/10.1073/pnas.1107748108

Mederos, S., Hernández-Vivanco, A., Ramírez-Franco, J., Martín-Fernández, M., Navarrete, M., Yang, A., Boyden, E.S., Perea, G., 2019. Melanopsin for precise optogenetic activation of astrocyte-neuron networks. Glia 67, 915–934. https://doi.org/10.1002/glia.23580

Meissner, W., Leblois, A., Hansel, D., Bioulac, B., Gross, C.E., Benazzouz, A., Boraud, T., 2005. Subthalamic high frequency stimulation resets subthalamic firing and reduces abnormal oscillations. Brain 128, 2372–2382. https://doi.org/10.1093/brain/awh616

Middleton, F.A., Strick, P.L., 2000. Basal ganglia and cerebellar loops: motor and cognitive circuits. Brain Res. Rev. 31, 236–250. https://doi.org/10.1016/S0165-0173(99)00040-5

Miller, W.C., DeLong, M.R., 1987. Altered Tonic Activity of Neurons in the Globus Pallidus and Subthalamic Nucleus in the Primate MPTP Model of Parkinsonism, in: Carpenter, M.B., Jayaraman, A. (Eds.), The Basal Ganglia II, Advances in Behavioral Biology. Springer US, Boston, MA, pp. 415–427. https://doi.org/10.1007/978-1-4684-5347-8_29

Mills, W.A., Woo, A.M., Jiang, S., Martin, J., Surendran, D., Bergstresser, M., Kimbrough, I.F., Eyo, U.B., Sofroniew, M.V., Sontheimer, H., 2022. Astrocyte plasticity in mice ensures continued endfoot coverage of cerebral blood vessels following injury and declines with age. Nat. Commun. 13, 1794. https://doi.org/10.1038/s41467-022-29475-2

Miocinovic, S., Somayajula, S., Chitnis, S., Vitek, J.L., 2013. History, Applications, and Mechanisms of Deep Brain Stimulation. JAMA Neurol. 70, 163. https://doi.org/10.1001/2013.jamaneurol.45

Montagne, A., Barnes, S.R., Sweeney, M.D., Halliday, M.R., Sagare, A.P., Zhao, Z., Toga, A.W., Jacobs, R.E., Liu, C.Y., Amezcua, L., Harrington, M.G., Chui, H.C., Law, M., Zlokovic, B.V., 2015. Blood-brain barrier breakdown in the aging human hippocampus. Neuron 85, 296–302. https://doi.org/10.1016/j.neuron.2014.12.032

Moye, S.L., Diaz-Castro, B., Gangwani, M.R., Khakh, B.S., 2019. Visualizing Astrocyte Morphology Using Lucifer Yellow Iontophoresis. JoVE J. Vis. Exp. e60225. https://doi.org/10.3791/60225

Mudannayake, J.M., Mouravlev, A., Fong, D.M., Young, D., 2016. Transcriptional activity of novel ALDH1L1 promoters in the rat brain following AAV vector-mediated gene transfer. Mol. Ther. Methods Clin. Dev. 3, 16075. https://doi.org/10.1038/mtm.2016.75

Murphy-Royal, C., Dupuis, J., Groc, L., Oliet, S.H.R., 2017. Astroglial glutamate transporters in the brain: Regulating neurotransmitter homeostasis and synaptic transmission. J. Neurosci. Res. 95, 2140–2151. https://doi.org/10.1002/jnr.24029

Nagai, J., Rajbhandari, A.K., Gangwani, M.R., Hachisuka, A., Coppola, G., Masmanidis, S.C., Fanselow, M.S., Khakh, B.S., 2019. Hyperactivity with Disrupted Attention by

Activation of an Astrocyte Synaptogenic Cue. Cell 177, 1280-1292.e20. https://doi.org/10.1016/j.cell.2019.03.019

Nagy, J.I., Patel, D., Ochalski, P.A., Stelmack, G.L., 1999. Connexin30 in rodent, cat and human brain: selective expression in gray matter astrocytes, co-localization with connexin43 at gap junctions and late developmental appearance. Neuroscience 88, 447–468. https://doi.org/10.1016/s0306-4522(98)00191-2

Nevado-Holgado, A.J., Mallet, N., Magill, P.J., Bogacz, R., 2014. Effective connectivity of the subthalamic nucleus-globus pallidus network during Parkinsonian oscillations. J. Physiol. 592, 1429–1455. https://doi.org/10.1113/jphysiol.2013.259721

Nicchia, G.P., Srinivas, M., Li, W., Brosnan, C.F., Frigeri, A., Spray, D.C., 2005. New possible roles for aquaporin-4 in astrocytes: cell cytoskeleton and functional relationship with connexin43. FASEB J. Off. Publ. Fed. Am. Soc. Exp. Biol. 19, 1674–1676. https://doi.org/10.1096/fj.04-3281fje

Nini, A., Feingold, A., Slovin, H., Bergman, H., 1995. Neurons in the globus pallidus do not show correlated activity in the normal monkey, but phase-locked oscillations appear in the MPTP model of parkinsonism. J. Neurophysiol. 74, 1800–1805. https://doi.org/10.1152/jn.1995.74.4.1800

Niu, J., Tsai, H.-H., Hoi, K.K., Huang, N., Yu, G., Kim, K., Baranzini, S.E., Xiao, L., Chan, J.R., Fancy, S.P.J., 2019. Aberrant oligodendroglial-vascular interactions disrupt the blood-brain barrier, triggering CNS inflammation. Nat. Neurosci. 22, 709–718. https://doi.org/10.1038/s41593-019-0369-4

Oberheim, N.A., Takano, T., Han, X., He, W., Lin, J.H., Wang, F., Xu, Q., Wyatt, J.D., Pilcher, W., Ojemann, J.G., Ransom, B.R., Goldman, S.A., Nedergaard, M., 2009. Uniquely

hominid features of adult human astrocytes. J. Neurosci. Off. J. Soc. Neurosci. 29, 3276. https://doi.org/10.1523/JNEUROSCI.4707-08.2009

Oberheim, N.A., Wang, X., Goldman, S., Nedergaard, M., 2006. Astrocytic complexity distinguishes the human brain. Trends Neurosci. 29, 547–553. https://doi.org/10.1016/j.tins.2006.08.004

O'Neill, K.M., Saracino, E., Barile, B., Mennona, N.J., Mola, M.G., Pathak, S., Posati, T., Zamboni, R., Nicchia, G.P., Benfenati, V., Losert, W., 2023. Decoding Natural Astrocyte Rhythms: Dynamic Actin Waves Result from Environmental Sensing by Primary Rodent Astrocytes. Adv. Biol. 7, 2200269. https://doi.org/10.1002/adbi.202200269

Pamukcu, A., Cui, Q., Augustine, E.C., Fan, I.B., Berceau, B.L., Xenias, H.S., Lerner, T.N., Chan, C.S., 2019. Pallidal PV+ neurons and Npas1+ neurons have distinct input and function.

Pannasch, U., Vargová, L., Reingruber, J., Ezan, P., Holcman, D., Giaume, C., Syková, E., Rouach, N., 2011. Astroglial networks scale synaptic activity and plasticity. Proc. Natl. Acad. Sci. U. S. A. 108, 8467–8472. https://doi.org/10.1073/pnas.1016650108

Parent, A., 1986. Comparative Neurobiology of the Basal Ganglia, Wiley Series in Neurobiology. Wiley.

Paxinos, G., Franklin, K.B.J., 2019. Paxinos and Franklin's the Mouse Brain in Stereotaxic Coordinates. Academic Press.

Paxinos, G., Huang, X.-F., Toga, A., 2000. The Rhesus Monkey Brain in Stereotaxic Coordinates. Acad. Press.

Peters, A., Palay, S.L., Webster, H., 1991. Astrocytes, in: The Fine Structure of the Nervous System: Neurons and Their Supporting Cells. pp. 276–294.

Phookan, S., Sutton, A.C., Walling, I., Smith, A., O'Connor, K.A., Campbell, J.C., Calos, M., Yu, W., Pilitsis, J.G., Brotchie, J.M., Shin, D.S., 2015. Gap junction blockers attenuate beta oscillations and improve forelimb function in hemiparkinsonian rats. Exp. Neurol. 265, 160–170. https://doi.org/10.1016/j.expneurol.2015.01.004

R. Virchow, 1846. Über das granulierte Ansehen der Wandungen der Gerhirnventrikel. Allg Z Psychiatr 3, 242.

Ramos-Gonzalez, P., Mato, S., Chara, J.C., Verkhratsky, A., Matute, C., Cavaliere, F., 2021. Astrocytic atrophy as a pathological feature of Parkinson's disease with LRRK2 mutation. Npj Park. Dis. 7, 1–11. https://doi.org/10.1038/s41531-021-00175-w

Ramsay, R.R., Salach, J.I., Singer, T.P., 1986. Uptake of the neurotoxin 1-methyl-4-phenylpyridine (MPP+) by mitochondria and its relation to the inhibition of the mitochondrial oxidation of NAD+-linked substrates by MPP+. Biochem. Biophys. Res. Commun. 134, 743–748. https://doi.org/10.1016/s0006-291x(86)80483-1

Ransom, B.R., Kunis, D.M., Irwin, I., Langston, J.W., 1987. Astrocytes convert the parkinsonism inducing neurotoxin, MPTP, to its active metabolite, MPP+. Neurosci. Lett. 75, 323–328. https://doi.org/10.1016/0304-3940(87)90543-x

Riachi, N.J., Harik, S.I., Kalaria, R.N., Sayre, L.M., 1988. On the mechanisms underlying 1-methyl-4-phenyl-1,2,3,6-tetrahydropyridine neurotoxicity. II. Susceptibility among mammalian species correlates with the toxin's metabolic patterns in brain microvessels and liver. J. Pharmacol. Exp. Ther. 244, 443–448.

Rouach, N., Koulakoff, A., Abudara, V., Willecke, K., Giaume, C., 2008. Astroglial Metabolic Networks Sustain Hippocampal Synaptic Transmission. Science 322, 1551–1555. https://doi.org/10.1126/science.1164022

Rouach, N., Segal, M., Koulakoff, A., Giaume, C., Avignone, E., 2003. Carbenoxolone blockade of neuronal network activity in culture is not mediated by an action on gap junctions. J. Physiol. 553, 729–745. https://doi.org/10.1113/jphysiol.2003.053439

Rufer, M., Wirth, S. b., Hofer, A., Dermietzel, R., Pastor, A., Kettenmann, H., Unsicker, K., 1996. Regulation of connexin-43, GFAP, and FGF-2 is not accompanied by changes in astroglial coupling in MPTP-lesioned, FGF-2-treated Parkisonian mice. J. Neurosci. Res. 46, 606–617. https://doi.org/10.1002/(SICI)1097-4547(19961201)46:5<606::AID-JNR9>3.0.CO;2-N

Salmon, C.K., Syed, T.A., Kacerovsky, J.B., Alivodej, N., Schober, A.L., Sloan, T.F.W., Pratte, M.T., Rosen, M.P., Green, M., Chirgwin-Dasgupta, A., Mehta, S., Jilani, A., Wang, Y., Vali, H., Mandato, C.A., Siddiqi, K., Murai, K.K., 2023. Organizing principles of astrocytic nanoarchitecture in the mouse cerebral cortex. Curr. Biol. CB 33, 957-972.e5. https://doi.org/10.1016/j.cub.2023.01.043

Salvesen, L., Ullerup, B.H., Sunay, F.B., Brudek, T., Løkkegaard, A., Agander, T.K., Winge, K., Pakkenberg, B., 2015. Changes in total cell numbers of the basal ganglia in patients with multiple system atrophy — A stereological study. Neurobiol. Dis. 74, 104–113. https://doi.org/10.1016/j.nbd.2014.11.008

Sanders, T.H., Clements, M.A., Wichmann, T., 2013. Parkinsonism-related features of neuronal discharge in primates. J. Neurophysiol. 110, 720–731. https://doi.org/10.1152/jn.00672.2012

Santiago Ramon y Cajal, 1911. Histologie du systeme nerveux de l'homme et des vertebres. A. Maloine, Paris.

Saper, C.B., 2005. An open letter to our readers on the use of antibodies. J. Comp. Neurol. 493, 477–478. https://doi.org/10.1002/cne.20839

Saper, C.B., Sawchenko, P.E., 2003. Magic peptides, magic antibodies: guidelines for appropriate controls for immunohistochemistry. J. Comp. Neurol. 465, 161–163. https://doi.org/10.1002/cne.10858

Schapira, A.H., Cooper, J.M., Dexter, D., Clark, J.B., Jenner, P., Marsden, C.D., 1990. Mitochondrial complex I deficiency in Parkinson's disease. J. Neurochem. 54, 823–827. https://doi.org/10.1111/j.1471-4159.1990.tb02325.x

Schildknecht, S., Di Monte, D.A., Pape, R., Tieu, K., Leist, M., 2017. Tipping Points and Endogenous Determinants of Nigrostriatal Degeneration by MPTP. Trends Pharmacol. Sci. 38, 541–555. https://doi.org/10.1016/j.tips.2017.03.010

Schildknecht, S., Pape, R., Meiser, J., Karreman, C., Strittmatter, T., Odermatt, M., Cirri, E., Friemel, A., Ringwald, M., Pasquarelli, N., Ferger, B., Brunner, T., Marx, A., Möller, H.M., Hiller, K., Leist, M., 2015. Preferential Extracellular Generation of the Active Parkinsonian Toxin MPP+ by Transporter-Independent Export of the Intermediate MPDP+. Antioxid. Redox Signal. 23, 1001–1016. https://doi.org/10.1089/ars.2015.6297

Schindelin, J., Arganda-Carreras, I., Frise, E., Kaynig, V., Longair, M., Pietzsch, T., Preibisch, S., Rueden, C., Saalfeld, S., Schmid, B., Tinevez, J.-Y., White, D.J., Hartenstein, V., Eliceiri, K., Tomancak, P., Cardona, A., 2012. Fiji: an open-source platform for biological-image analysis. Nat. Methods 9, 676–682. https://doi.org/10.1038/nmeth.2019

Schwab, B.C., Wezel, R.J.A. van, Gils, S.A. van, 2017. Sparse pallidal connections shape synchrony in a network model of the basal ganglia. Eur. J. Neurosci. 45, 1000–1012. https://doi.org/10.1111/ejn.13324

Seabold, G.K., Daunais, J.B., Rau, A., Grant, K.A., Alvarez, V.A., 2010. DiOLISTIC Labeling of Neurons from Rodent and Non-human Primate Brain Slices. JoVE J. Vis. Exp. https://dx.doi.org/10.3791/2081-v

Shen, R.S., Abell, C.W., Gessner, W., Brossi, A., 1985. Serotonergic conversion of MPTP and dopaminergic accumulation of MPP+. FEBS Lett. 189, 225–230. https://doi.org/10.1016/0014-5793(85)81028-0

Shigetomi, E., Bushong, E.A., Haustein, M.D., Tong, X., Jackson-Weaver, O., Kracun, S., Xu, J., Sofroniew, M.V., Ellisman, M.H., Khakh, B.S., 2013. Imaging calcium microdomains within entire astrocyte territories and endfeet with GCaMPs expressed using adeno-associated viruses. J. Gen. Physiol. 141, 633–647. https://doi.org/10.1085/jgp.201210949

Sholl, D.A., 1953. Dendritic organization in the neurons of the visual and motor cortices of the cat. J. Anat. 87, 387-406.1.

Soares, J., Kliem, M.A., Betarbet, R., Greenamyre, J.T., Yamamoto, B., Wichmann, T., 2004. Role of external pallidal segment in primate parkinsonism: comparison of the effects of 1-methyl-4-phenyl-1,2,3,6-tetrahydropyridine-induced parkinsonism and lesions of the external pallidal segment. J. Neurosci. Off. J. Soc. Neurosci. 24, 6417–6426. https://doi.org/10.1523/JNEUROSCI.0836-04.2004

Sokoloff, L., 1977. Relation between physiological function and energy metabolism in the central nervous system. J. Neurochem. 29, 13–26. https://doi.org/10.1111/j.1471-4159.1977.tb03919.x

Song, Y.J.C., Halliday, G.M., Holton, J.L., Lashley, T., O'Sullivan, S.S., McCann, H., Lees, A.J., Ozawa, T., Williams, D.R., Lockhart, P.J., Revesz, T.R., 2009. Degeneration in Different Parkinsonian Syndromes Relates to Astrocyte Type and Astrocyte Protein

Expression. J. Neuropathol. Exp. Neurol. 68, 1073–1083. https://doi.org/10.1097/NEN.0b013e3181b66f1b

Spix, T.A., Nanivadekar, S., Toong, N., Kaplow, I.M., Isett, B.R., Goksen, Y., Pfenning, A.R., Gittis, A.H., 2021. Population-specific neuromodulation prolongs therapeutic benefits of deep brain stimulation. Science 374, 201–206. https://doi.org/10.1126/science.abi7852

Stefanis, L., 2012. α-Synuclein in Parkinson's Disease. Cold Spring Harb. Perspect. Med. 2, a009399. https://doi.org/10.1101/cshperspect.a009399

Stehberg, J., Moraga-Amaro, R., Salazar, C., Becerra, A., Echeverría, C., Orellana, J.A., Bultynck, G., Ponsaerts, R., Leybaert, L., Simon, F., Sáez, J.C., Retamal, M.A., 2012. Release of gliotransmitters through astroglial connexin 43 hemichannels is necessary for fear memory consolidation in the basolateral amygdala. FASEB J. 26, 3649–3657. https://doi.org/10.1096/fj.11-198416

Steigerwald, F., Pötter, M., Herzog, J., Pinsker, M., Kopper, F., Mehdorn, H., Deuschl, G., Volkmann, J., 2008. Neuronal activity of the human subthalamic nucleus in the parkinsonian and nonparkinsonian state. J. Neurophysiol. 100, 2515–2524. https://doi.org/10.1152/jn.90574.2008

Stogsdill, J.A., Ramirez, J., Liu, D., Kim, Y.-H., Baldwin, K.T., Enustun, E., Ejikeme, T., Ji, R.-R., Eroglu, C., 2017. Astrocytic Neuroligins Control Astrocyte Morphogenesis and Synaptogenesis. Nature 551, 192–197. https://doi.org/10.1038/nature24638

Sun, W., Cornwell, A., Li, J., Peng, S., Osorio, M.J., Aalling, N., Wang, S., Benraiss, A., Lou, N., Goldman, S.A., Nedergaard, M., 2017. SOX9 Is an Astrocyte-Specific Nuclear Marker in the Adult Brain Outside the Neurogenic Regions. J. Neurosci. 37, 4493–4507. https://doi.org/10.1523/JNEUROSCI.3199-16.2017

Sun, W., McConnell, E., Pare, J.-F., Xu, Q., Chen, M., Peng, W., Lovatt, D., Han, X., Smith, Y., Nedergaard, M., 2013. Glutamate-Dependent Neuroglial Calcium Signaling Differs Between Young and Adult Brain. Science 339, 197–200. https://doi.org/10.1126/science.1226740

Szabó, Z., Héja, L., Szalay, G., Kékesi, O., Füredi, A., Szebényi, K., Dobolyi, Á., Orbán, T.I., Kolacsek, O., Tompa, T., Miskolczy, Z., Biczók, L., Rózsa, B., Sarkadi, B., Kardos, J., 2017. Extensive astrocyte synchronization advances neuronal coupling in slow wave activity in vivo. Sci. Rep. 7, 1–18. https://doi.org/10.1038/s41598-017-06073-7

Tachibana, Y., Iwamuro, H., Kita, H., Takada, M., Nambu, A., 2011. Subthalamo-pallidal interactions underlying parkinsonian neuronal oscillations in the primate basal ganglia. Eur. J. Neurosci. 34, 1470–1484. https://doi.org/10.1111/j.1460-9568.2011.07865.x

Takano, T., Tian, G.-F., Peng, W., Lou, N., Libionka, W., Han, X., Nedergaard, M., 2006. Astrocyte-mediated control of cerebral blood flow. Nat. Neurosci. 9, 260–267. https://doi.org/10.1038/nn1623

Tatsumi, K., Okuda, H., Morita-Takemura, S., Tanaka, T., Isonishi, A., Shinjo, T., Terada, Y., Wanaka, A., 2016. Voluntary Exercise Induces Astrocytic Structural Plasticity in the Globus Pallidus. Front. Cell. Neurosci. 10. https://doi.org/10.3389/fncel.2016.00165

Tepper, J.M., Bolam, J.P., 2004. Functional diversity and specificity of neostriatal interneurons. Curr. Opin. Neurobiol. 14, 685–692. https://doi.org/10.1016/j.conb.2004.10.003

Theodosis, D.T., Poulain, D.A., Oliet, S.H.R., 2008. Activity-dependent structural and functional plasticity of astrocyte-neuron interactions. Physiol. Rev. 88, 983–1008. https://doi.org/10.1152/physrev.00036.2007

Tong, J., Ang, L.-C., Williams, B., Furukawa, Y., Fitzmaurice, P., Guttman, M., Boileau, I., Hornykiewicz, O., Kish, S.J., 2015. Low levels of astroglial markers in Parkinson's disease: relationship to α-synuclein accumulation. Neurobiol. Dis. 82, 243–253. https://doi.org/10.1016/j.nbd.2015.06.010

Torres, A., Wang, F., Xu, Q., Fujita, T., Dobrowolski, R., Willecke, K., Takano, T., Nedergaard, M., 2012. Extracellular Ca2+ Acts as a Mediator of Communication from Neurons to Glia. Sci. Signal. 5, ra8–ra8. https://doi.org/10.1126/scisignal.2002160

Valsky, D., Heiman Grosberg, S., Israel, Z., Boraud, T., Bergman, H., Deffains, M., 2020. What is the true discharge rate and pattern of the striatal projection neurons in Parkinson's disease and Dystonia? eLife 9, e57445. https://doi.org/10.7554/eLife.57445

Vasile, F., Dossi, E., Rouach, N., 2017. Human astrocytes: structure and functions in the healthy brain. Brain Struct. Funct. 222, 2017–2029. https://doi.org/10.1007/s00429-017-1383-5

Ventura, R., Harris, K.M., 1999. Three-Dimensional Relationships between Hippocampal Synapses and Astrocytes. J. Neurosci. 19, 6897–6906. https://doi.org/10.1523/JNEUROSCI.19-16-06897.1999

Verkhratsky, A., Bush, N.A.O., Nedergaard, M., Butt, A., 2018. The Special Case of Human Astrocytes. Neuroglia 1, 21–29. https://doi.org/10.3390/neuroglia1010004

Villalba, R.M., Smith, Y., 2011. Neuroglial Plasticity at Striatal Glutamatergic Synapses in Parkinson's Disease. Front. Syst. Neurosci. 5, 68. https://doi.org/10.3389/fnsys.2011.00068

Vints, K., Vandael, D., Baatsen, P., Pavie, B., Vernaillen, F., Corthout, N., Rybakin, V., Munck, S., Gounko, N.V., 2019. Modernization of Golgi staining techniques for high-resolution,

3-dimensional imaging of individual neurons. Sci. Rep. 9, 130. https://doi.org/10.1038/s41598-018-37377-x

Virchow, R., 1856. Gesammelte Abhandlungen zur wissenschaftlichen Medizin. Verlag von Meidinger Sohn & Comp, Frankfurt.

Wang, N., De Bock, M., Antoons, G., Gadicherla, A.K., Bol, M., Decrock, E., Evans, W.H., Sipido, K.R., Bukauskas, F.F., Leybaert, L., 2012. Connexin mimetic peptides inhibit Cx43 hemichannel opening triggered by voltage and intracellular Ca2+ elevation. Basic Res. Cardiol. 107, 304. https://doi.org/10.1007/s00395-012-0304-2

Wang, Y., Wu, Z., Liu, X., Fu, Q., 2013. Gastrodin ameliorates Parkinson's disease by downregulating connexin 43. Mol. Med. Rep. 8, 585–590. https://doi.org/10.3892/mmr.2013.1535

Wang, Y.-F., Parpura, V., 2016. Central Role of Maladapted Astrocytic Plasticity in Ischemic Brain Edema Formation. Front. Cell. Neurosci. 10, 129. https://doi.org/10.3389/fncel.2016.00129

Weigert, C., 1895. Beiträge zur Kenntnis der Normalen Menschlichen Neuroglia. Ärztlicher Verein, Frankfurt, Germany.

Wichmann, T., DeLong, M.R., 2003. Pathophysiology of Parkinson's disease: the MPTP primate model of the human disorder. Ann. N. Y. Acad. Sci. 991, 199–213. https://doi.org/10.1111/j.1749-6632.2003.tb07477.x

Wichmann, T., Kliem, M.A., DeLong, M.R., 2001. Antiparkinsonian and Behavioral Effects of Inactivation of the Substantia Nigra Pars Reticulata in Hemiparkinsonian Primates. Exp. Neurol. 167, 410–424. https://doi.org/10.1006/exnr.2000.7572

Wichmann, T., Soares, J., 2006. Neuronal firing before and after burst discharges in the monkey basal ganglia is predictably patterned in the normal state and altered in parkinsonism. J. Neurophysiol. 95, 2120–2133. https://doi.org/10.1152/jn.01013.2005

Wiest, C., Torrecillos, F., Pogosyan, A., Bange, M., Muthuraman, M., Groppa, S., Hulse, N., Hasegawa, H., Ashkan, K., Baig, F., Morgante, F., Pereira, E.A., Mallet, N., Magill, P.J., Brown, P., Sharott, A., Tan, H., 2023. The aperiodic exponent of subthalamic field potentials reflects excitation/inhibition balance in Parkinsonism. eLife 12, e82467. https://doi.org/10.7554/eLife.82467

Wildenberg, G.A., Rosen, M.R., Lundell, J., Paukner, D., Freedman, D.J., Kasthuri, N., 2021. Primate neuronal connections are sparse in cortex as compared to mouse. Cell Rep. 36, 109709. https://doi.org/10.1016/j.celrep.2021.109709

Winawer, J., Kay, K.N., Foster, B.L., Rauschecker, A.M., Parvizi, J., Wandell, B.A., 2013. Asynchronous broadband signals are the principal source of the BOLD response in human visual cortex. Curr. Biol. CB 23, 1145–1153. https://doi.org/10.1016/j.cub.2013.05.001

Witcher, M.R., Kirov, S.A., Harris, K.M., 2007. Plasticity of perisynaptic astroglia during synaptogenesis in the mature rat hippocampus. Glia 55, 13–23. https://doi.org/10.1002/glia.20415

Wright, C.S., Steensel, M.A.M.V., Hodgins, M.B., Martin, P.E.M., 2009. Connexin mimetic peptides improve cell migration rates of human epidermal keratinocytes and dermal fibroblasts in vitro. Wound Repair Regen. 17, 240–249. https://doi.org/10.1111/j.1524-475X.2009.00471.x

Yu, X., Nagai, J., Khakh, B.S., 2020. Improved tools to study astrocytes. Nat. Rev. Neurosci. 21, 121–138. https://doi.org/10.1038/s41583-020-0264-8

Zaja-Milatovic, S., Milatovic, D., Schantz, A.M., Zhang, J., Montine, K.S., Samii, A., Deutch, A.Y., Montine, T.J., 2005. Dendritic degeneration in neostriatal medium spiny neurons in Parkinson disease. Neurology 64, 545–547. https://doi.org/10.1212/01.WNL.0000150591.33787.A4

Zhang, Y., Sloan, S.A., Clarke, L.E., Caneda, C., Plaza, C.A., Blumenthal, P.D., Vogel, H., Steinberg, G.K., Edwards, M.S.B., Li, G., Duncan, J.A., Cheshier, S.H., Shuer, L.M., Chang, E.F., Grant, G.A., Hayden Gephart, M.G., Barres, B.A., 2016. Purification and characterization of progenitor and mature human astrocytes reveals transcriptional and functional differences with mouse. Neuron 89, 37–53. https://doi.org/10.1016/j.neuron.2015.11.013